CRUSTAL STRESS ORIENTATION PROFILE TO A DEPTH OF 3.5KM NEAR THE SAN ANDREAS FAULT AT CAJON PASS, CALIFORNIA

A DISSERTATION
SUBMITTED TO THE DEPARTMENT OF
APPLIED EARTH SCIENCES
AND THE COMMITTEE ON GRADUATE STUDIES
OF STANFORD UNIVERSITY
IN PARTIAL FULFILLMENT OF THE REQUIREMENTS
FOR THE DEGREE OF
DOCTOR OF PHILOSOPHY

BY
GADI SHAMIR
NOVEMBER 1990

Abstract

Located 4.2km from the San Andreas Fault, the Cajon Pass research drillhole was designed primarily to study the heat flow and in situ stress associated with the fault. A detailed profile of the orientation of borehole breakouts as a function of depth was constructed by analyzing data obtained by borehole televiewers. Forming at the locus of the maximum compressive tangential stress concentration at the borehole wall, breakout azimuth is determined by the orientation of the principal stresses applied to the borehole. Significant variations in breakout azimuth as a function of depth occur over borehole-parallel length scales from a few centimeters to hundreds of meters. They reflect fluctuations in the stress field sampled by the borehole and are predominantly associated with fractures penetrated during drilling. The latter are therefore active faults which slipped recently in geological history, resulting in stress fluctuations which are then sampled by the borehole. In order to model this process, the maximum tangential stress resulting from the superposition of the fault-induced and the ambient stresses is calculated at points on the borehole wall for variable seismic moments and stress drops. For the geometry of faulting considered, it is found that if fault stress drops are limited by the available ambient shear stress and seismic observations, the drop in tangential stress near a slipping fault can result in intermittent breakout occurrence, discontinuous orientation changes and gradual changes of up to several tens of degrees. The specific geometry depends on local rock strength. The borehole-parallel length scale of breakout azimuth perturbations generally underestimates the actual extent of the stress drop zone. If extreme stress drops occur locally, so that the fault-induced tangential stresses exceed the ambient field, then stress increases, rather than decreases, near the fault and

continuous breakout azimuth changes may reach full 180° rotations over borehole length 2-3 times the fault half-length. Such locally amplified stress drops, undetected in the far-field, may result from fault heterogeneities, fault ends, etc..

The spectra of the borehole-parallel extent of stress fluctuations in selected intervals, up to 120m long, show fractal-like behavior over broad spatial bandwidths. This apparently suggest that a spatially self-similar distribution of seismic stress drops has been directly sampled by the Cajon Pass drillhole.

The overall mean breakout orientation in the Cajon Pass drillhole (azimuth 147°-327°) has a fairly small standard deviation of 19°; if it reflects the average orientation of the principal horizontal stresses near the San Andreas Fault at Cajon Pass, then the horizontal maximum compressive stress is oriented 057°, resulting in left-lateral shear stress resolved on planes parallel to the fault. Dislocation modelling of the current earthquake cycle along the Cajon Pass segment of the San Andreas Fault suggests that the state of stress near the Cajon Pass site is very close to that immediately prior to the 1812 earthquake, the last large seismic event to occur in this area. It is difficult to reconcile the measured stress magnitudes with the calculated shear stress budget through any plausible physical mechanism, even if a slip overshoot in 1812 is hypothesized. While it is unclear whether the depth of the borehole exceeded the maximum extent of local, fault-induced stress fluctuations, the Cajon Pass stress orientation results seem to rule out the existence of significant right-lateral shear stress parallel to the San Andreas Fault in the Cajon Pass area.

Contents

1. Background and motivation

1.1 Introduction....1

1.2 Stress-induced wellbore breakouts....7

2. Data acquisition and analysis....13

3. Stress orientation results....20

4. Crustal stress heterogeneity at Cajon Pass

4.1 Mechanics of fault-induced borehole breakouts....34

4.2 The wavelength spectra of borehole stress fluctuations 50

4.3 Discussion....56

5. The San Andreas seismic cycle near Cajon Pass

5.1 Introduction....61

5.2 Shear stress accumulation since 1812....69

5.3 Effects of aseismic slip near Cajon Pass....77

5.4 Discussion....84

6. Appendices

A.1 Polyaxial stress state near boreholes....89

A.2 Borehole Televiewer calibration....90

A.3 Effects of lithological and drilling parameters on borehole breakouts at Cajon Pass....94

7. References....99

List of Tables

Table 1: Orientations of the maximum horizontal compressive stress in the Mojave Desert.....5

Table 2: Fractal dimensions from spectral analysis of breakout orientation variations in the Cajon Pass wellbore.....56

Table 3: Displacements and displacement rates along the San Andreas and San Jacinto Faults in the Cajon Pass area.....66-67

List of Figures

Figure 1.1: Generalized fault map of the western Mojave Desert..... 2

Figure 1.2: Borehole breakouts in cylindrical and cross sectional views.....8

Figure 1.3: Polyaxial state of stress at the borehole wall..... 11

Figure 2.1: BHTV logs and hydraulic fracturing tests in the Cajon Pass drillhole..... 14

Figure 2.2: NNE-oriented borehole breakouts in unwrapped, cylindrical and cross sectional views from a depth of 2844m in the Cajon Pass drillhole 15

Figure 2.3: Orientation of the apparent maximum horizontal compressive stress as a function of depth - comparison between the BHTV and the four-arm caliper output..... 17

Figure 2.4: Determination of the orientation of the apparent maximum horizontal compressive stress based on borehole breakouts..... 19

Figure 3.1: Profile of the orientation of the apparent maximum horizontal stress as a function of depth in the interval 1750-3460m in the Cajon Pass borehole 21

Figure 3.2: E-W oriented borehole breakouts in unwrapped and cross sectional views from a depth of 2933m in the Cajon Pass drillhole 22

Figure 3.3: Zonation in the orientation profile of the apparent maximum horizontal compressive stress 24

Figure 3.4: Examples of gradual and discontinuous changes in breakout orientation in the shallow crust at Cajon Pass.....25-28

Figure 3.5: Comparison of the fracture frequency and the orientation of the apparent maximum horizontal

compressive stress in the lower 400m of the Cajon Pass drillhole 30

Figure 3.6: Gradual and discontinuous variations in the orientation of the apparent maximum horizontal compressive stress and geometry of the associated fractures 31

Figure 3.7: Overall orientation distribution of wellbore breakouts in the interval 1750-3460m in the Cajon Pass drillhole..... 33

Figure 4.1: Model for the mechanics of fault-induced borehole stress perturbations 37

Figure 4.2: Seismic moments vs. source radius from Mommoth Lake and San Jacinto Fault earthquakes 40

Figure 4.3: Calculated magnitude and orientation of the maximum tangential stress at the borehole wall for seismic moments lower than $10^{20.5}$ dyne-cm 43

Figure 4.4: Same as Fig. 4.3, for seismic moments higher than $10^{20.5}$ dyne-cm 44

Figure 4.5: Calculated circumferential variations in borehole ambient, fault-induced and total tangential stresses..... 45

Figure 4.6: Effect of rock strength on the extent of breakout occurrence near a fault of $M_0=10^{20}$ dyne-cm..... 47

Figure 4.7: Same as Fig. 4.6 for a fault of $M_0=10^{21}$ dyne-cm..... 49

Figure 4.8: Power spectral density of breakout orientation variations in the Cajon pass drillhole..... 53-54

Figure 5.1: Major strike changes along the trace of the San Andreas Fault near Cajon Pass 63

Figure 5.2: Dislocation model of the San Andreas and San Jacinto faults near Cajon Pass..... 64

Figure 5.3: The change in shear stress parallel to the San Andreas Fault near Cajon Pass due to the 1812 earthquake.....70

Figure 5.4: The change in shear stress parallel to the San Andreas Fault near Cajon Pass due to the 1857 earthquake.....72-73

Figure 5.5: The change in shear stress parallel to the San Andreas Fault near Cajon Pass since immediately prior to the 1812 earthquake.....76

Figure 5.6: Tse et al.'s (1985) model of the San Andreas Fault as a double edge-crack in elastic plate.....78

Figure 5.7: The modified orientation of the horizontal principal compressive stress for different remotely applied stress fields.....81

Figure 5.8: Effects of the shallow creeping zone and the deep aseismic slip zone on the change in stress orientation near the San Andreas Fault.....83

Figure 5.9: The change in earthquake-related stress terms as a function of displacement in a one-dimensional earthquake model.....86

Figure A.2.1: Calibration container for borehole televiewers.....91

Figure A.2.2: Graphic output from a BHTV calibration run.....92

Figure A.3.1 Comparison between the orientation of the apparent maximum horizontal compressive stress, biotite content in the drilled rocks, and some drilling parameters in the Cajon Pass drillhole.....95-98

1. BACKGROUND AND MOTIVATION

1.1 Introduction

The southern San Andreas Fault (SAF; Fig. 1.1) has been the locus of many large earthquakes in historic and pre-historic times (Lawson et al., 1908; Agnew and Sieh, 1978; Sieh et al., 1989). The last one occurred in 1857 (M_S~8.2; Sieh, 1978), rupturing more than 350 km, from Cholame (near Parkfield) in Central California to the vicinity of Cajon Pass in the south. The southern termination of the 1857 surface rupture was probably about 20km northwest of Cajon Pass (Weldon and Sieh, 1985). The previous large earthquake in this region, that of December 1812, probably ruptured about 170km of the SAF with a southern termination several tens of km southeast of Cajon Pass (Jacoby et al., 1988; Sieh et al., 1989).

Evidence for the sense and magnitude of the long term slip along the San Andreas fault near Cajon Pass comes from various independent sources. Overall, about 300km of right-lateral displacement across the SAF has occurred since the middle Miocene (Hill and Diblee, 1953; Crowell, 1962). Late Holocene right-lateral surface slip, at a rate of 24.5±3.5 mm/yr, was determined by Weldon and Sieh (1985) based on offset Quarternary deposits. Crustal strain accumulation in this region, based on repeated trilateration surveys (Savage et al., 1986) has a maximum horizontal shortening azimuth of 344°±2° for the period 1973-1984, consistent with deep right-lateral slip along the SAF.

The level of shear stress resisting faulting along the San Andreas Fault has been a subject of considerable debate since early measurements of heat flow (Henyey, 1968; Henyey and Wasserburg,1971) showed that no positive heat anomaly is localized over the fault. Such anomalous heat level would have

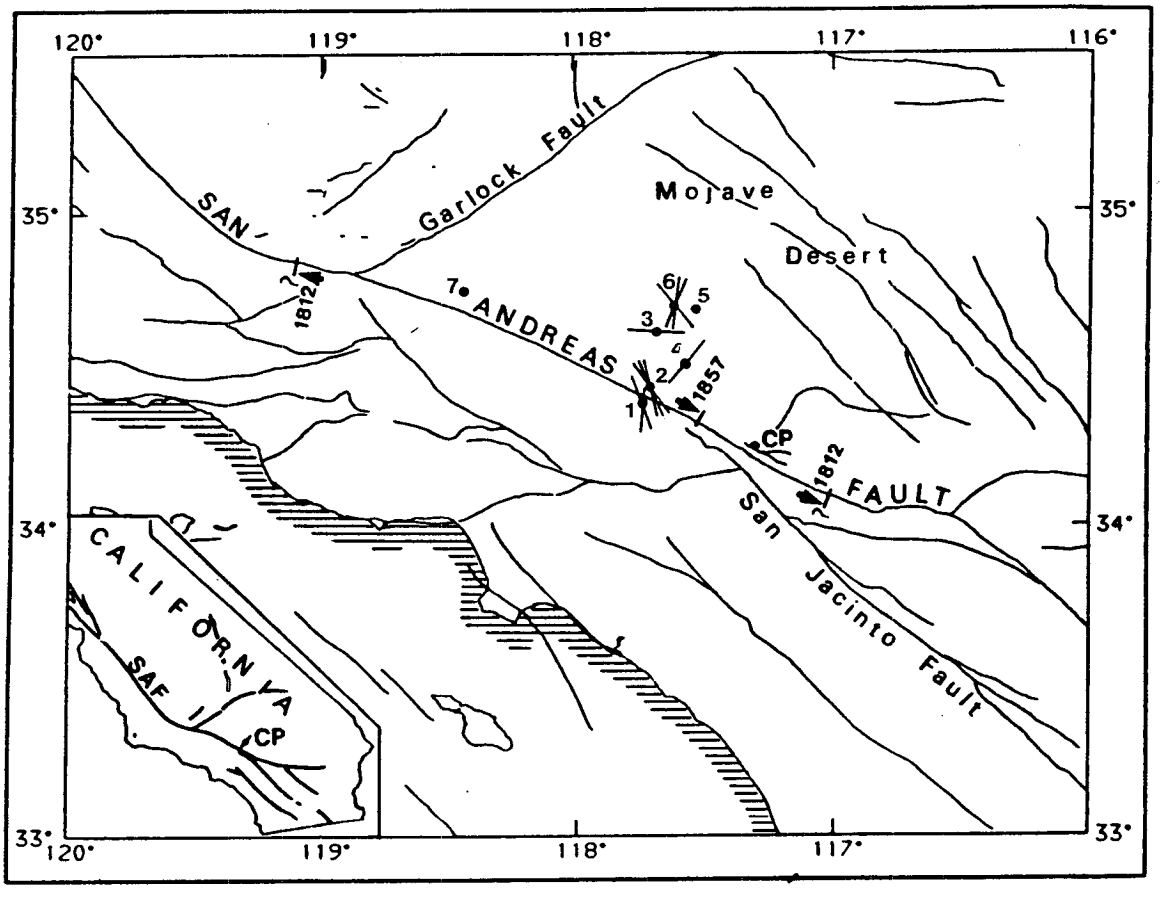

Figure 1.1 Generalized fault map of the westerm Mojave Desert and the Transverse Ranges in southern California, showing the location of the Cajon Pass drillhole (CP) and sites of previous in situ stress tests in this region (1=Moj1; 2=XTLR; 3=Black Bute; 4=Moj4; 5=Moj5; 6=Hi Vista; 7=Lake Hughes). Also shown are the presumed rupture terminations of the 1812 (Jacoby et al., 1989) and 1857 (Weldon and Sieh, 1985) earthquakes along the San Andreas Fault.

been generated by the (seismically undetectable) frictional stress resisting fault motion in large earthquakes. Brune et al. (1969) pointed out that this finding puts an upper limit of about 10MPa on the dynamic frictional stress (assuming a mean slip rate of 5 cm/yr) and of about 20MPa on the long term average static strength, i.e. the possibly "undetected" frictional heat. Brune et al. (1969) also hypothesized that the strength of the fault may be anomalously low compared to the rupture strengths determined in lab experiments. These results have been later supported by many additional heat flow measurements, by theoretical analysis (Lachenbruch and Sass, 1973, 1980) and, in central California's locked section of the SAF, by in situ stress orientations, which have been interpreted to indicate that the direction of the maximum horizontal compressive stress is nearly perpendicular to the trace of the San Andreas (Zoback et al., 1987; Mount and Suppe, 1987). Lachenbruch (1980) hypothesized that the "weakness" of the SAF may be either permanent or come about only during large earthquakes due to transient mechanisms which reduce or eliminate the coseismic frictional resistance (Lachenbruch, 1980; Melosh, 1979; McKenzie and Brune, 1972). In the first case one would expect that the SAF is nearly parallel to a principal stress plane over time scales much larger than the seismic cycle. In the second case the SAF is expected to lie in more or less optimal orientation with respect to the principal driving stresses, with an extremely large drop in resistance only during the coseismic slip. A very low shear stress resolved on the fault during the interseismic period, as the in situ stress orientation data of Central California may suggest, as well as low stress drops (1-100MPa), both imply permanent weakness of the fault.

The hypothesis that the San Andreas Fault is inherently "weak" is inconsistent with numerous laboratory friction experiments (e.g. Stesky and Brace, 1973; Byerlee, 1978), and in situ stress measurements (McGarr and Gay, 1978; Brace

and Kohlstedt, 1980; McGarr, 1980; Zoback and Healy, 1984). These studies concluded that crustal faults support fairly high average frictional stresses and that the average fault strength is comparable to that of the surrounding rocks. In her study of earthquake focal mechanisms of events occurring along the southern San Andreas Fault between 1978 and 1985, Jones (1988) suggested that along most of that part of the fault the angle between the orientation of the maximum horizontal compressive stress and the fault is about 65°, except for the area just south of Cajon Pass. Overall, then, no clear prediction of the expected mean orientation of the principal stresses can be made for the Cajon Pass area and the western Mojave Desert.

Past in situ stress measurements (primarily hydraulic fracturing tests up to 0.9 km deep) in the western Mojave Desert have shown highly variable stress magnitudes and orientations. These measurements were aimed at determining the state of stress on the SAF based on a model of Lachenbruch and Sass (1973), who related (through equilibrium considerations) the vertical shear stress gradient on the fault with the horizontal gradient away from it. The azimuths of the horizontal maximum compressive stress determined in six wells roughly making a profile perpendicular to the trace of the SAF (Zoback and Roller, 1979; McGarr, 1980; Zoback et al., 1980; Hickman et al., 1988; Stock and Healy, 1988) are shown in Fig. 1.1 and summarized in Table 1. They show variations that span 66° between wells and that a significant local variation (63°) was observed in the Hi Vista well (Hickman et al., 1988). Furthermore, horizontal gradients of all stress components as a function of distance from the SAF seemed to reverse their trends between the shallow (<230m) and the deeper levels.

Table 1

Depth (m)	Moj.1[1]	XTLR[1]	Black Butte[2]	Moj.4[1]	HiVista[3]	Lake Hughes[4]
73				104±10°(P)		
80	340±10°(F)					
104				093±10°(P)		
149		093±10°(P)				
167		083±10°(P)				
178					007±15°(G)	
185	337±10°(P)					
218	004±10°(F)					
230		346±10°(E)				
271					321±15°(G)	
309			041±10°			
323					320±20°(P)	
338		317±10°(F)				
491					023±20°(F)	
561		340±10°(P)				
787		336±10°(E)				
		341±10°(G)				
984						040°

(1) Zoback et al., 1980

(2) High quality impression, but lacking independent confirmation; Stock and Healy, 1988

(3) Hickman et al., 1988

(4) Based on borehole breakouts, Castillo, unpublished work.

E=Excellent; G=Good; F=Fair; P=Poor.

McGarr et al. (1982), Hickman et al. (1988) and Stock and Healy (1988) all pointed out that the available shallow in situ stress data in the western Mojave Desert, and specifically along the San Andreas profile, show exceptional variability. Hickman et al. (1988) concluded that "inversion of the stress measurements ... for the magnitude of shear stress at depth on the San Andreas Fault is not feasible until the origin of the observed variations are understood". These results are in contrast to the situation in many regions in the U.S. and world-wide (Zoback and Zoback, 1989; Zoback et al., 1989), where fairly uniform stress orientation patterns have been deduced by using the same techniques as in the Mojave Desert experiments.

The Cajon Pass scientific drilling project (Zoback et al., 1988), located about 4km northeast of the active trace of the SAF, was designed primarily to address the stress/heat flow contradiction of the San Andreas Fault through deep measurements, as close as possible to the fault zone itself. It was originally planned to reach a depth of 5km, that is, to the top of the seismogenic zone. To date the borehole has reached a depth of 3.5km. Key experiments were heat flow and production and in-situ stress measurements, at depths considerably greater than those penetrated before near the SAF. These experiments were designed to show whether conductive heat flow increases at the depth where hypothetical effects of water circulation (O'Neil and Hanks, 1980) diminish, and to determine the actual state of stress at nearly seismogenic depths near the SAF.

Twenty three determinations of the horizontal minimum principal stress were obtained in the Cajon Pass drillhole through hydraulic fracturing experiments (Healy and Zoback, 1988; Zoback and Healy, 1991). The study described in this

thesis is concerned with the profile of the orientation of stresses as a function of depth, determined through analysis of stress-induced borehole breakouts.

1.2 Stress-induced wellbore breakouts

Wellbore breakouts (Fig. 1.2) are azimuthally-restricted zones of spalling at borehole walls, spanning a few tens of degrees of circumference. Such borehole failure largely occurs spontaneously following drilling and can be distinguished, using the imaging technique described below, from spalling associated with the intersection of fractures, mechanical erosion of the hole due to pipe rubbing, or washouts at fault zones.

Observations in the field and in laboratory experiments (e.g. Leeman, 1964; Cox, 1970; Bell and Gough, 1979; Gough and Bell, 1982; Hickman et al., 1985; Zoback et al., 1985; Haimson and Herrick, 1985; Mastin, 1984; Ewy and Cook, 1989; Maloney and Kaiser, 1989) are generally consistent with Gough and Bell's (1979) original suggestion that breakouts occur at the two, diametrically-opposed points of maximum circumferential compressive stress at the wall of boreholes. If the compressive strength of the rock is exceeded at these points, failure will initiate and the two broken-out zones would be co-linear and aligned with the azimuth of the remote least compressive stress orthogonal to the borehole. This hypothesis is based on the classic two-dimensional (plane strain) solution for a circular hole in an isotropic elastic plate under differential in-plane remote compressive stress (Kirsch, 1898; Jaeger and Cook, 1976, p. 249). It is applicable to boreholes which are parallel to one principal stress, commonly the vertical, and was extended by Zoback et al. (1985) to predict the

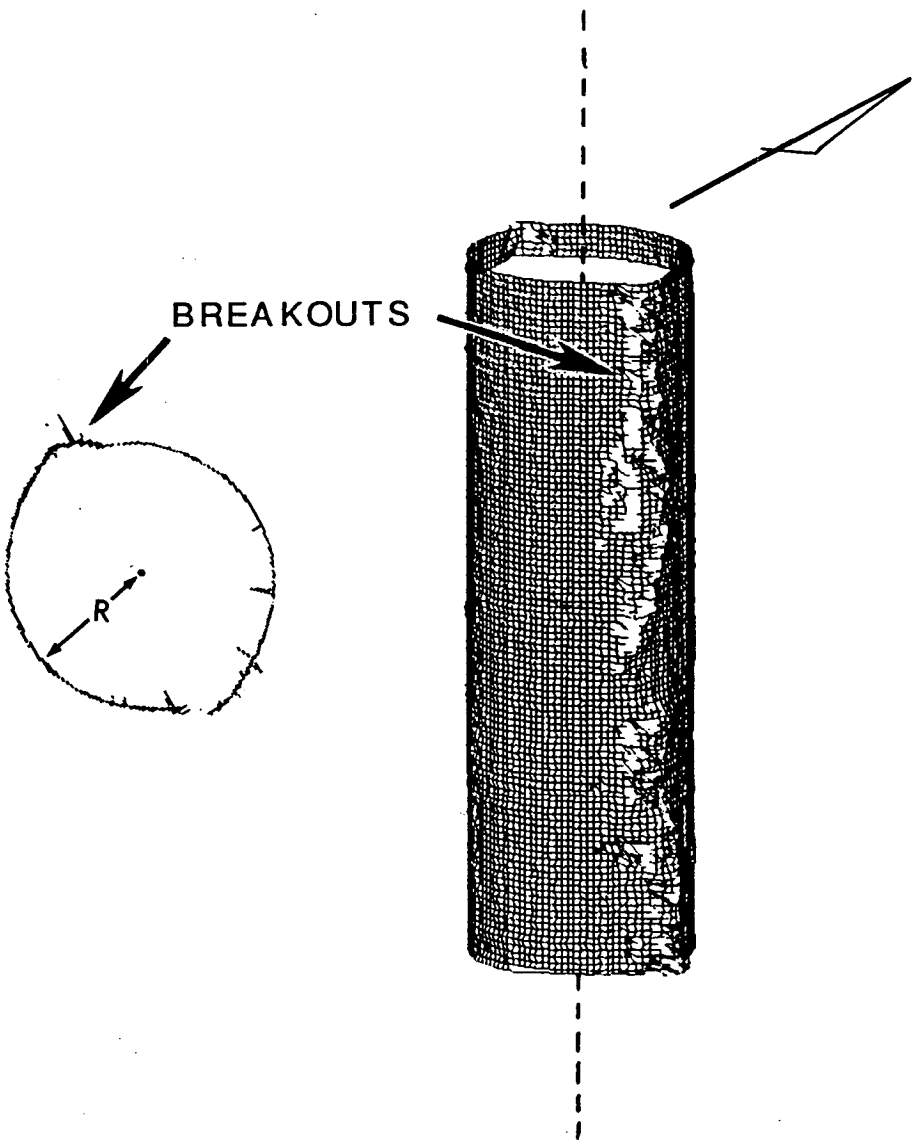

Figure 1.2 Wellbore breakouts in a cylindrical borehole relief view and in polar cross section (data from depth of 3km in the Cajon Pass drillhole; R=8.25cm).

expected breakout morphology given the remote stresses, the compressive strength of the rock and a Mohr-Coulomb failure criterion.

An alternative approach to borehole breakout development has been based on the observation (e.g. Leeman, 1960; Mastin, 1984; Zheng and Cook, 1985; Haimson and Herrick, 1985; Ewy et al., 1988) that they sometimes form by successive tensile splitting parallel to the borehole wall. However, as pointed out by Moos and Zoback (1990), this requires initial crack sliding and therefore stresses which are not substantially different from those required by compressive shear failure. A rigid-plastic, pressure-sensitive failure criterion for breakout development has been proposed by Vardoulakis et al. (1988).

The two-dimensional, elastic breakout hypothesis has been used in many studies (e.g. Gough and Bell, 1982; Hickman et al., 1985; Plumb and Cox, 1987; Barton et al., 1988; Zoback and Zoback, 1988; Zoback and Moos, 1989) which considered depth-averaged breakout orientations to estimate the orientation of the horizontal principal stresses. Average orientations of wellbore breakouts are, in many regions, generally consistent with horizontal stress orientations deduced from hydraulic fracturing, earthquake focal mechanisms and orientations of recently active faults. However, in order to study the stress field at the scale of the measurement, the general polyaxial state of stress around the borehole should be considered. In this way, a-priori assumptions concerning the orientation of the principal stresses applied to the well can be avoided.

Given a generally oriented, uniform remote stress field σ_{ij}^{∞} and borehole fluid column in equilibrium with the fluid pore pressure in the surrounding rock (i.e. vanishing radial principal stress at the wall), the only non-zero stress

components at the borehole wall are (Hiramatsu and Oka, 1962; Fig. 1.3), by setting r=R in Eqs. A1.1,

$$\sigma_{\theta\theta}^{eff} = \sigma_{11}^{\infty} + \sigma_{22}^{\infty} - 2\left(\sigma_{11}^{\infty} - \sigma_{22}^{\infty}\right)\cos 2\theta - 4\sigma_{12}^{\infty}\sin 2\theta - P_0 \qquad (1.1)$$

$$\sigma_{zz}^{eff} = \sigma_{33}^{\infty} - 0.5\left(\sigma_{11}^{\infty} - \sigma_{22}^{\infty}\right)\cos 2\theta - \sigma_{12}^{\infty}\sin 2\theta \qquad (1.2)$$

$$\sigma_{\theta z} = 2\left(\sigma_{23}^{\infty}\cos\theta - \sigma_{31}^{\infty}\sin\theta\right) \qquad (1.3)$$

where P_0 is the pore fluid pressure in the adjacent rock, θ is the circumferential angle. The borehole z axis is taken parallel to x_3 for simplicity. Then, the maximum compressive normal stress tangent to the borehole wall is given by

$$\sigma_t = \frac{\sigma_{\theta\theta} + \sigma_{zz}}{2} + \frac{1}{2}\sqrt{4\tau_{\theta z}^2 + (\sigma_{\theta\theta} - \sigma_{zz})^2} \qquad (1.4)$$

(where the superscript "eff" is dropped but effective stresses are implied) and the breakout initiation condition is

$$\sigma_t \geq C \,. \qquad (1.5)$$

In the two-dimensional case described above, $\sigma_t = \sigma_{\theta\theta}$ and one principal stress, as well as the breakouts, are parallel to the borehole axis, as in Fig. 1.2. In the general, 3-dimensional case, σ_t can be inclined at an angle ω to the borehole axis and varies, along any borehole circumference, between the values of σ_{zz} and $\sigma_{\theta\theta}$. As discussed by Moos and Zoback (1990), the state of stress at the borehole wall should be considered polyaxial for the purpose of considering the appropriate strength term C. Following Weibols and Cook (1968), they show that C lies in the range $C_0 \leq C \leq 1.36C_0$ (i.e. between 100 and 204 MPa for the different types of Cajon Pass rocks; L. Vernik, pers.

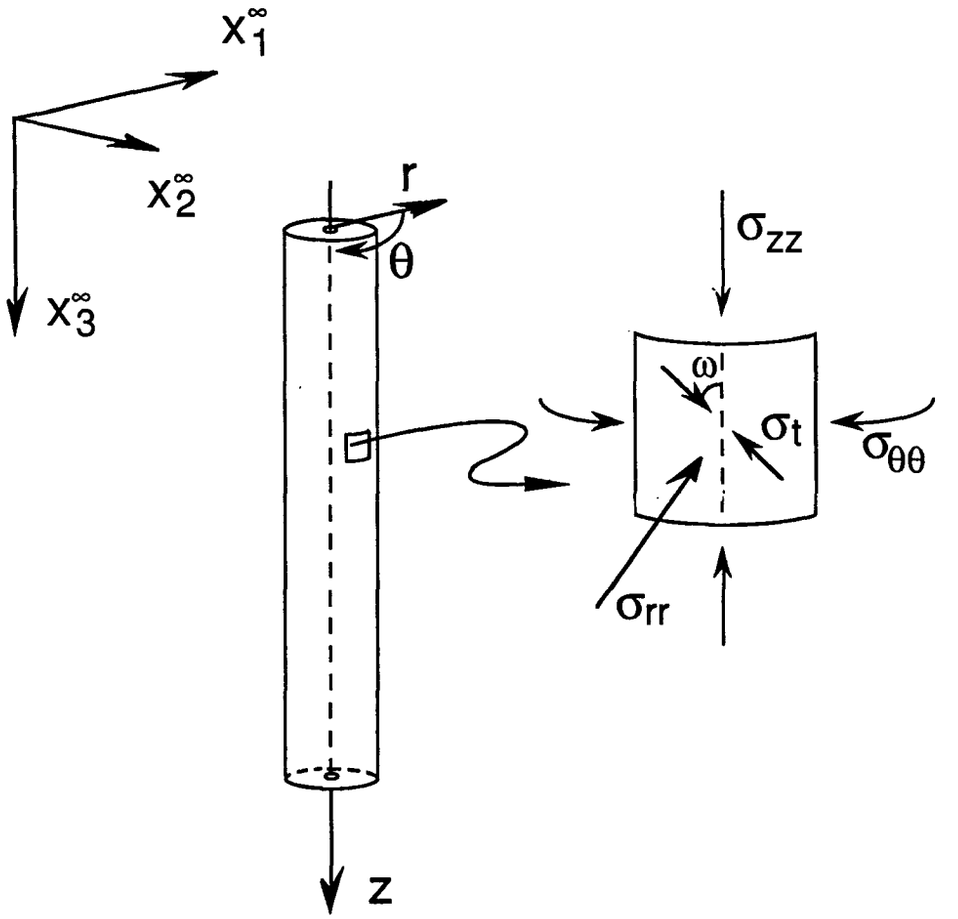

Figure 1.3 Polyaxial state of stress at the borehole wall. Stresses are shown with respect to the borehole cylindrical coordinate system. X_i^∞ - Coordinate system aligned with the remotely applied stress field; σ_{rr},$\sigma_{\theta\theta}$,σ_{zz} - Stress components at the borehole wall with respect to a cylindrical coordinate system r,θ,z, with the z axis parallel to the hole axis; σ_t - Maximum compressive normal stress tangent to the wellbore wall at any point (principal stress if σ_{rr}=0) and inclined by an angle ω to the borehole axis.

comm.), where C_0 is the unconfined compressive strength. If eq. 5 is satisfied, breakouts will form along a trace which is perpendicular to the maximum tangential stress in any borehole circumference. In the context of tensile failure, it has been shown (Daneshy, 1973; Hayashi et al., 1985; Kuriyagwa et al., 1989; Baumgartner et al., 1989) that the polyaxial stress state at the borehole wall results in hydraulic fractures which are discontinuous and inclined with respect to the borehole axis. For compressive borehole failure, Mastin (1988) analyzed the error involved in determination of S_H from wellbore breakouts when the borehole is inclined with respect to the principal stresses.

Regardless of the mechanical process responsible for breakout propagation, there is a general agreement that, when rock strength anisotropy is negligible, the locus of breakouts is determined by the elastic deformation of the rock and thus uniquely determines the location of stress concentration at the borehole wall. An important potential exception is the case when significant strength anisotropy, e.g. in the form of steeply dipping (≥40°) foliation planes, controls the locus and symmetry of failure at the borehole wall (Heinemann and Zoback, unpublished manuscript; Vernik and Zoback, 1990). In the case of Cajon Pass, only rarely are foliation planes steeper than about 40° and strength anisotropy has probably only a local and limited effect on breakout orientation (Vernik and Zoback, 1990).

2. DATA ACQUISITION

In order to study the stress-induced breakouts in the Cajon Pass wellbore, continuous acoustic images of the borehole were obtained through nineteen borehole televiewer (BHTV) logs. these were run through the entire Cajon Pass open hole by teams from Stanford University and the U.S. Geological Survey between February 1987 and April 1988 (Fig. 2.1). The BHTV is an ultrasonic, high resolution logging tool used originally to produce magneticaly-oriented reflectance images of borehole walls. As originally designed by Mobil Oil, Inc. (Zemanek et al., 1970), the BHTV contains a rotating acoustic transducer (1.4 Mhz) that emits a focused 3° beam pulse at a rate of 600 times per revolution, while the tool is pulled uphole at a rate of 2.5cm/s. The resulting vertical resolution is about 1cm. A fluxgate magnetometer within the tool triggers at each crossing of magnetic north. The raw BHTV output consists of the acoustic waveform (stored on video tapes) and reflectance images of the borehole wall obtained while logging. These enable real-time evaluation of the wellbore condition and selection of favorable intervals for hydraulic fracturing. In addition to detection of fractures and lithostratigraphic features, it was demonstrated that the televiewer is a powerful tool for imaging breakouts (e.g. Plumb and Hickman, 1985; Zoback et al., 1985; Hickman et al., 1985; Paillet and Kim, 1987; Barton 1988; Shamir et al., 1988).

The analysis of the Cajon Pass BHTV logs was based on high rate digitization (10^6 sec^{-1}) of the ultrasonic pulses reflected from the borehole wall, resulting in the dual measurement of the acoustic reflectivity and travel time (Barton, 1988). The basic graphic output consists of split 360° false-color images of the borehole radius (Fig. 2.2) and the reflectance amplitude, corrected for tool

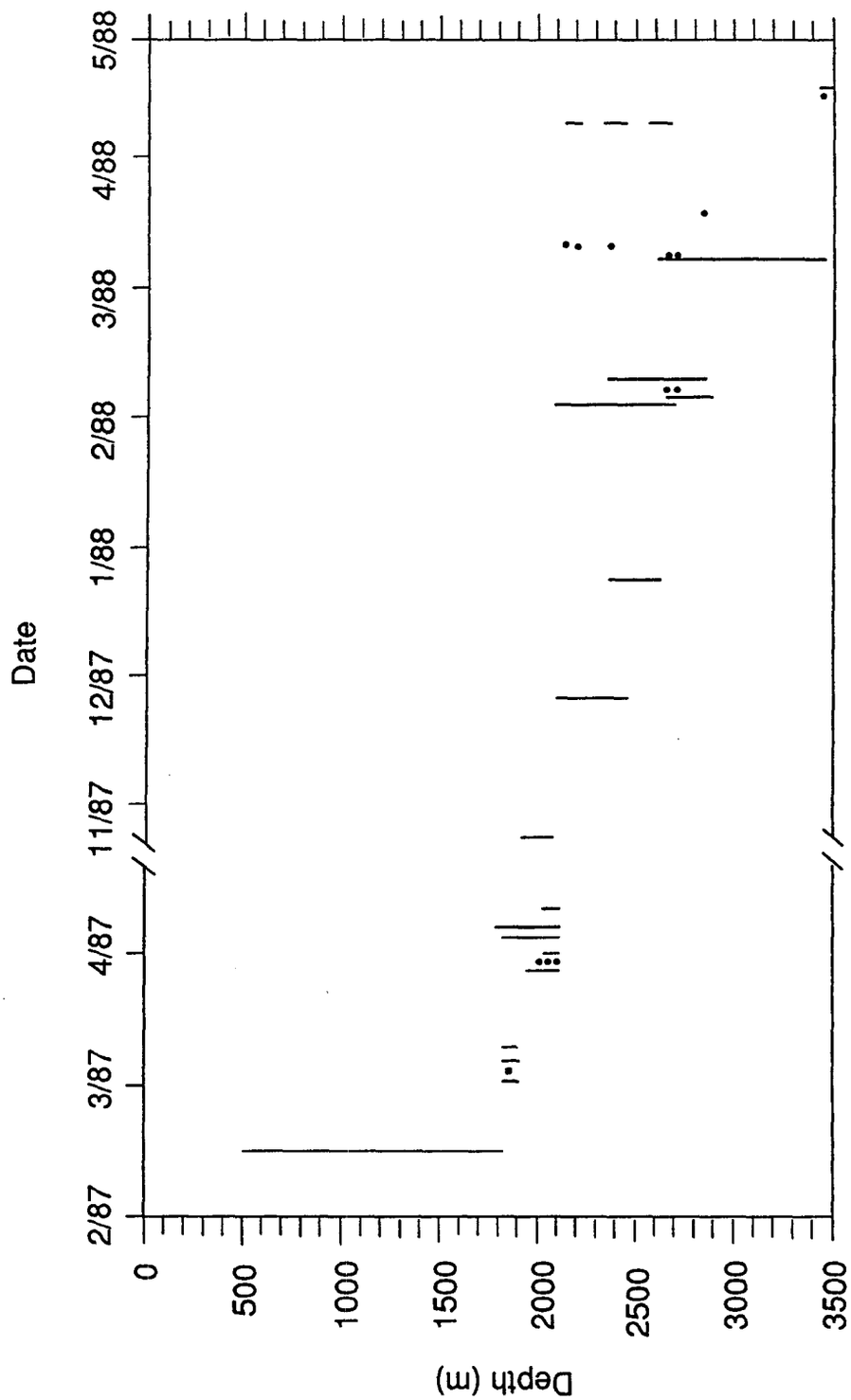

Figure 2.1 Borehole televiewer logs (lines) and hydraulic fracturing tests (dots) in the Cajon Pass drillhole.

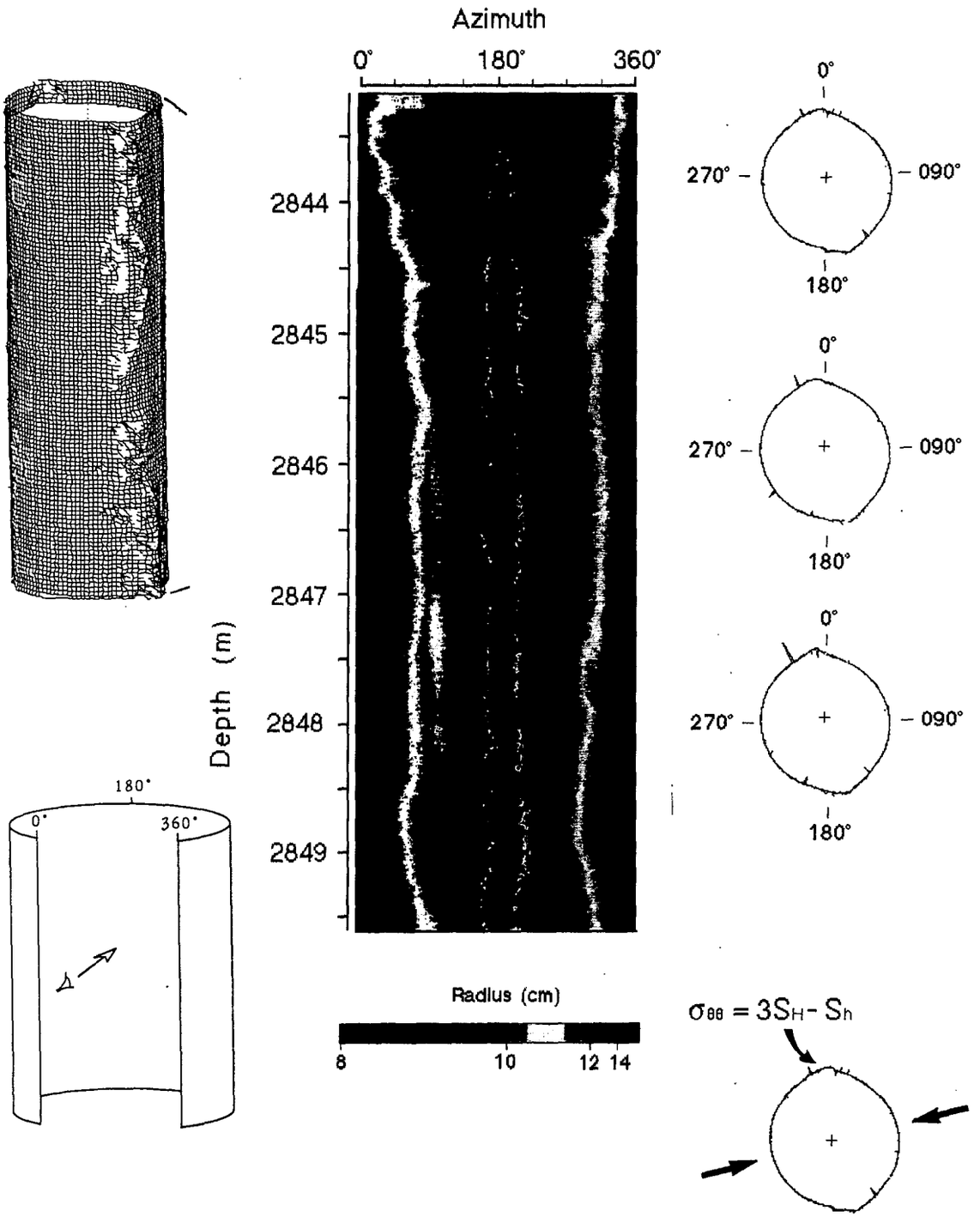

Figure 2.2 Unwrapped (lower left) borehole image (center), modulated by the borehole wall topography, of a section of the Cajon Pass drillhole. Breakouts (dark linear zones on the image) are parallel to the borehole axis (center) and oriented NNE-SSW (upper right). In this case, breakouts are at 90° the the orientation of the maximum horizontal compressive stress (lower right).

position in the hole and for magnetic declination. In the borehole shape analysis, polar cross sections of the hole are plotted, and breakout orientations are interactively measured (Fig. 2.2). For each of the Cajon Pass logs, the appropriate orientation and depth corrections were determined (see Appendix 2) and applied to the output data. Four different televiewers were run in the Cajon Pass borehole, all of which produced consistently oriented data. To further establish the reliability of the image orientations, breakout azimuths were compared to the caliper output of the magnetically oriented, four-arm formation microscanner (FMS). In the 4-arm caliper log (which has been the traditional tool for studying borehole elongations, prior to the introduction of the BHTV), breakouts are identified where the tool maintains a steady orientation (i.e. stops spiraling) along some depth interval, the two caliper readings differ significantly and the smaller reading is about equal to the drill bit size (Fordjor et al., 1983; Plumb and Hickman, 1985). Figure 2.3 shows a comparison of the output of the two tools for the depth interval 2980-3060m. Considering the different resolution of the two tools, the orientations are generally consistent, except where breakouts are either narrower than the FMS pads, or poorly developed and thus missed as the tool spirals up the hole. The caliper output may also show hole enlargements which are unrelated to borehole breakouts, e.g. due to mechanical erosion of the hole. The advantage of using the BHTV is therefore not only in recording more, and more accurate, breakout data, but also in the ability to distinguish between different types of borehole enlargements.

For the purpose of this analysis, five logs were used to construct a continuous acoustic image of the borehole between 503 and 3460 meters depth. The logs were chosen on the basis of the calibration accuracy, depth coverage, signal quality and proximity of logging to drilling. In the breakout analysis, polar cross

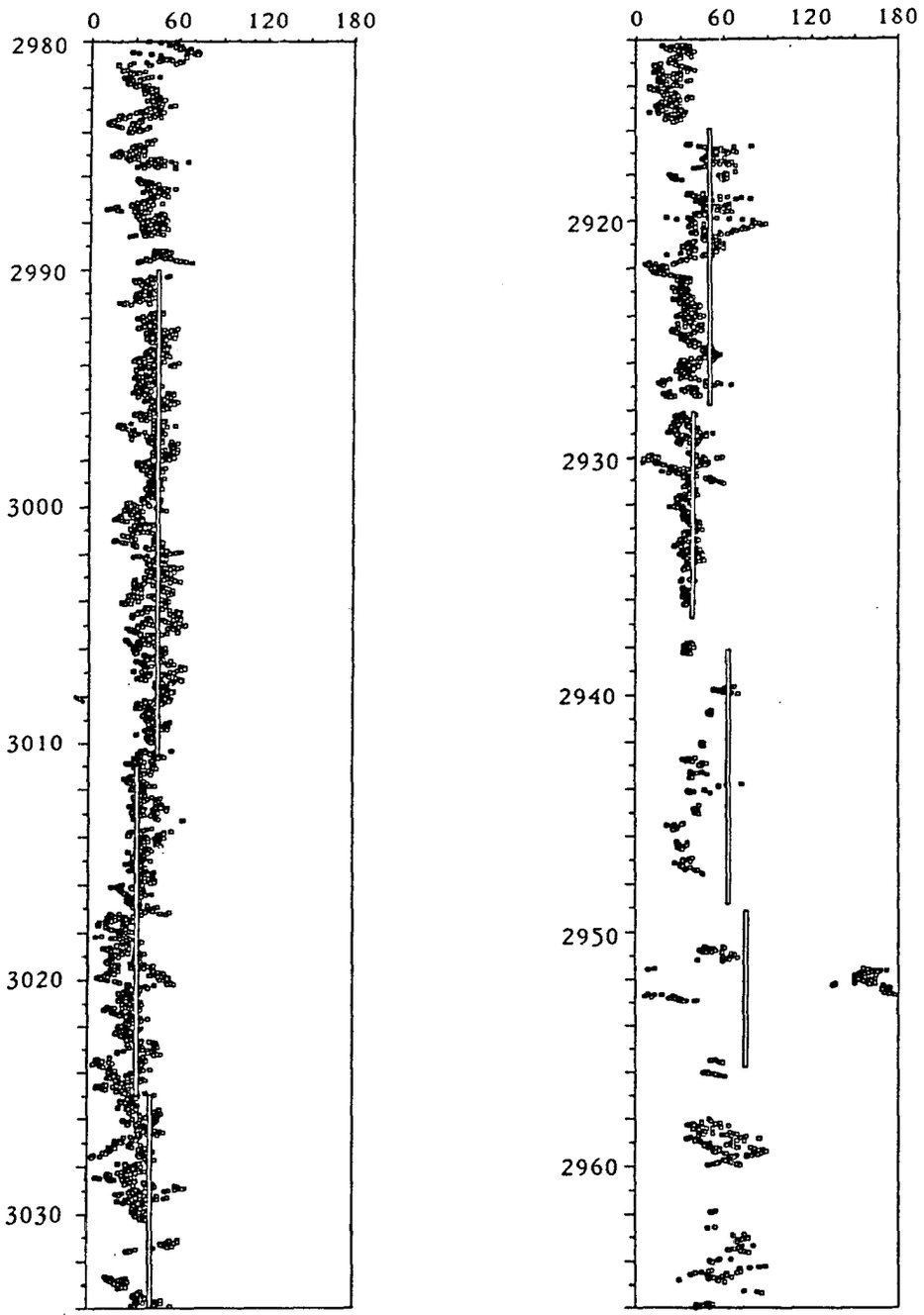

Figure 2.3. S_H^* orientation (90° from breakout azimuths) as a function of depth, as derived from the BHTV data (dots) and from the four-arm caliper data (lines).

sections were superimposed over 4cm intervals along the borehole, determining the basic spatial sampling interval. This choice provides high resolution, on the scale of the width of a single breakout or fracture, without interference of features on the grain scale. The midpoint of each breakout, on either side of the wellbore, was determined in each polar cross section (Fig. 2.4) and the azimuths Θ^*, at 90° to the breakouts, were recorded as function of depth throughout the breakout occurrence interval (1750-3460m). Θ^* is used as a general indicator of breakout orientation, regardless of the local stress field geometry. Only where breakout orientation is stable with depth, can it be assumed that one principal stress is sub-vertical (the borehole deviation was rarely more than 3°) and that Θ^* is the azimuth of the most compressive horizontal principal stress applied to the borehole. In general, however, changes of Θ^* strictly indicate the variability in the azimuth of the wellbore stress concentration as a function of depth. Overall, over 32,000 such data points were recorded in this interval in the Cajon Pass borehole, and were used to construct a detailed stress orientation profile.

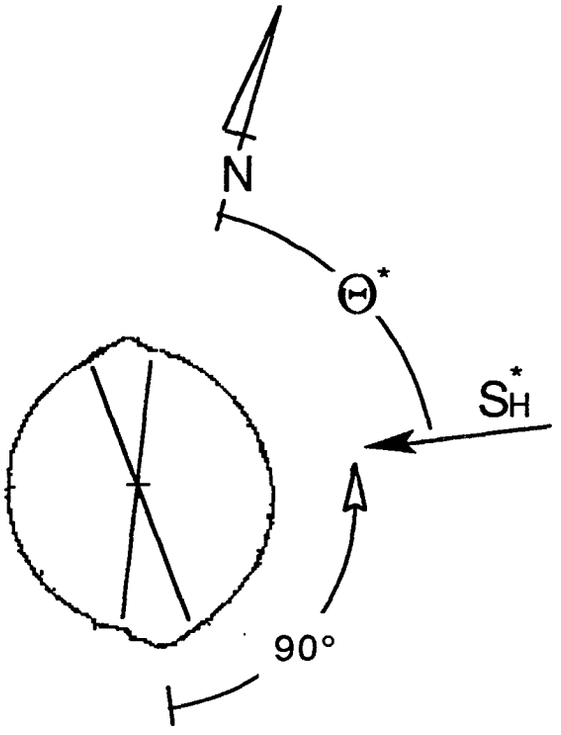

Figure 2.4 Breakout orientations represented by the azimuth Θ^* of the apparent maximum horizontal compressive stress S^*_H, at 90° to either breakout. In the particular case of one principal stress parallel to the borehole axis, Θ^* is independent of depth and S^*_H is assumed to represent the average maximum compressive stress orthogonal to the wellbore.

3. STRESS ORIENTATION RESULTS

Borehole breakouts first occur at a depth of 1.75km in the Cajon Pass drillhole. The complete profile of Θ^* as a function of depth, for the interval of breakout occurrence is shown in Figure 3.1, plotted in the azimuth range 0-180°. Each point represents one 4cm-averaged S_H^* orientation (apparent maximum horizontal compressive stress), measured as in Fig. 2.4. The azimuth of S_H^* is fairly stable along some depth intervals (e.g. 2770-2810m, 2980-3030m), but highly variable along others (e.g. 2840-2940m, 3260-3360m). Gaps in the profile represent sections of the borehole where no wall failure occurred (mostly in the interval 1750-2450m) or where the hole caved to an extent that little acoustic energy was reflected back from the wall. The latter resulted either from borehole caving at major fault zones (stippled intervals in Fig. 3.1) or, rarely, from mechanical erosion of the borehole.

In light of the result shown in Fig. 3.1, a special effort was made to verify that the changes in breakout azimuth indeed reflect variations in the state of stress with depth, by comparing the S_H^* profile with several lithological and drilling parameters (see Appendix A.3). It was found to be uncorrelated to lithological variations (Silver and James, 1988; L. Vernik, pers. com.), to borehole deviation or trend, to drill-bit penetration rate and to changes in biotite content in the penetrated rocks. The latter re-confirmed that strength (and elastic) anisotropy did not play an important role in determining the orientation and symmetry of breakouts, except perhaps sporadically. Figure 3.2 shows breakouts which are nearly orthogonal to those shown in Figure 2.2 and the cross-sectional morphology of breakouts can be seen to be independent of their orientation. Thus, mistaken identification of preferentially-oriented fractures as breakouts

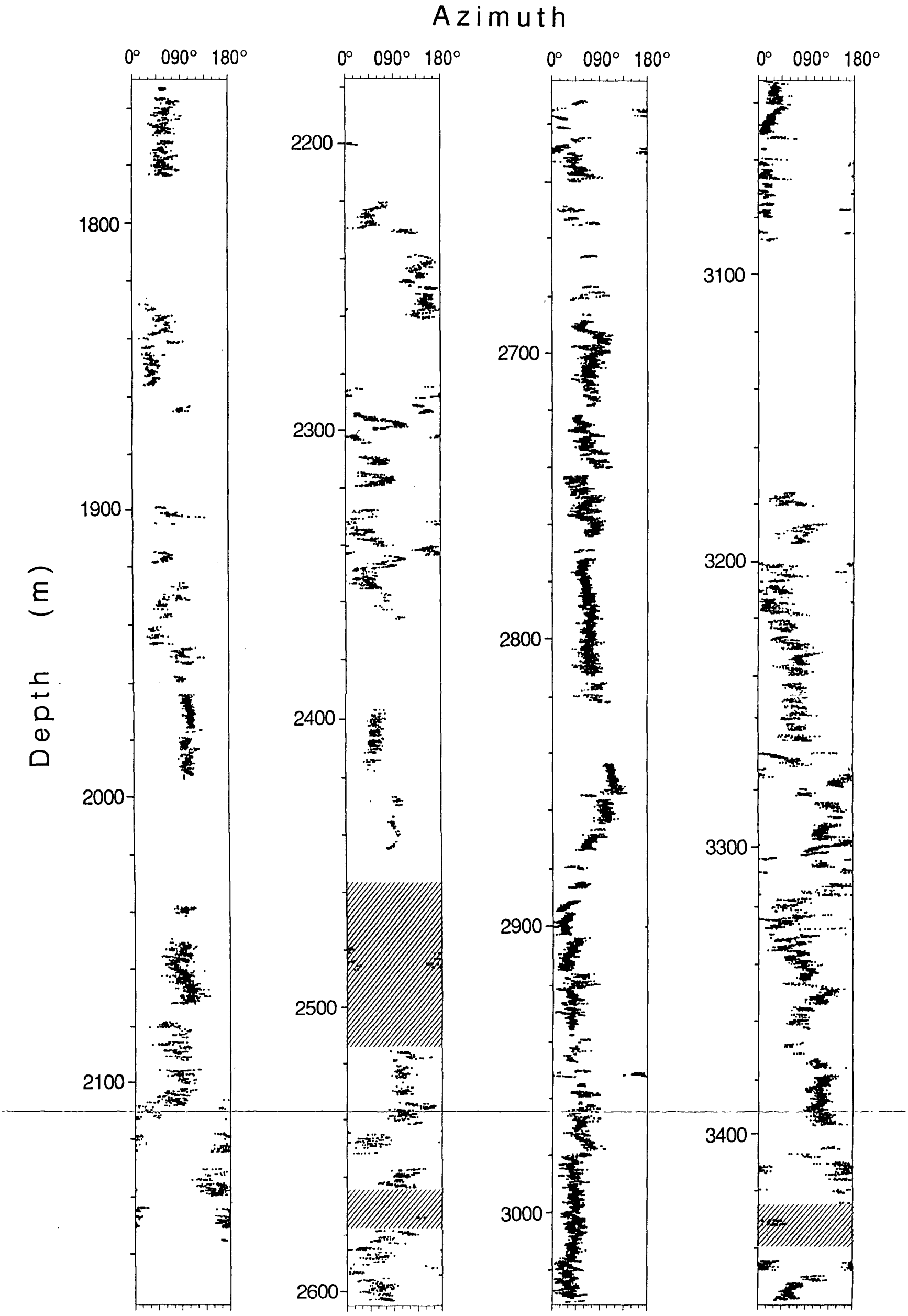

Figure 3.1 Profile of the orientation Θ^* of apparent maximum horizontal compressive stress S_H^*, as a function of depth, in the interval of breakout occurrence (1750-3460m). Each point represents a 4cm-averaged azimuth Θ^* based on one breakout, from either side of the borehole (determined as in Fig. 2.4). Intervals of poor data quality (stippled) due to extensive caving of the wellbore are typical of major fault zones. n=32616.

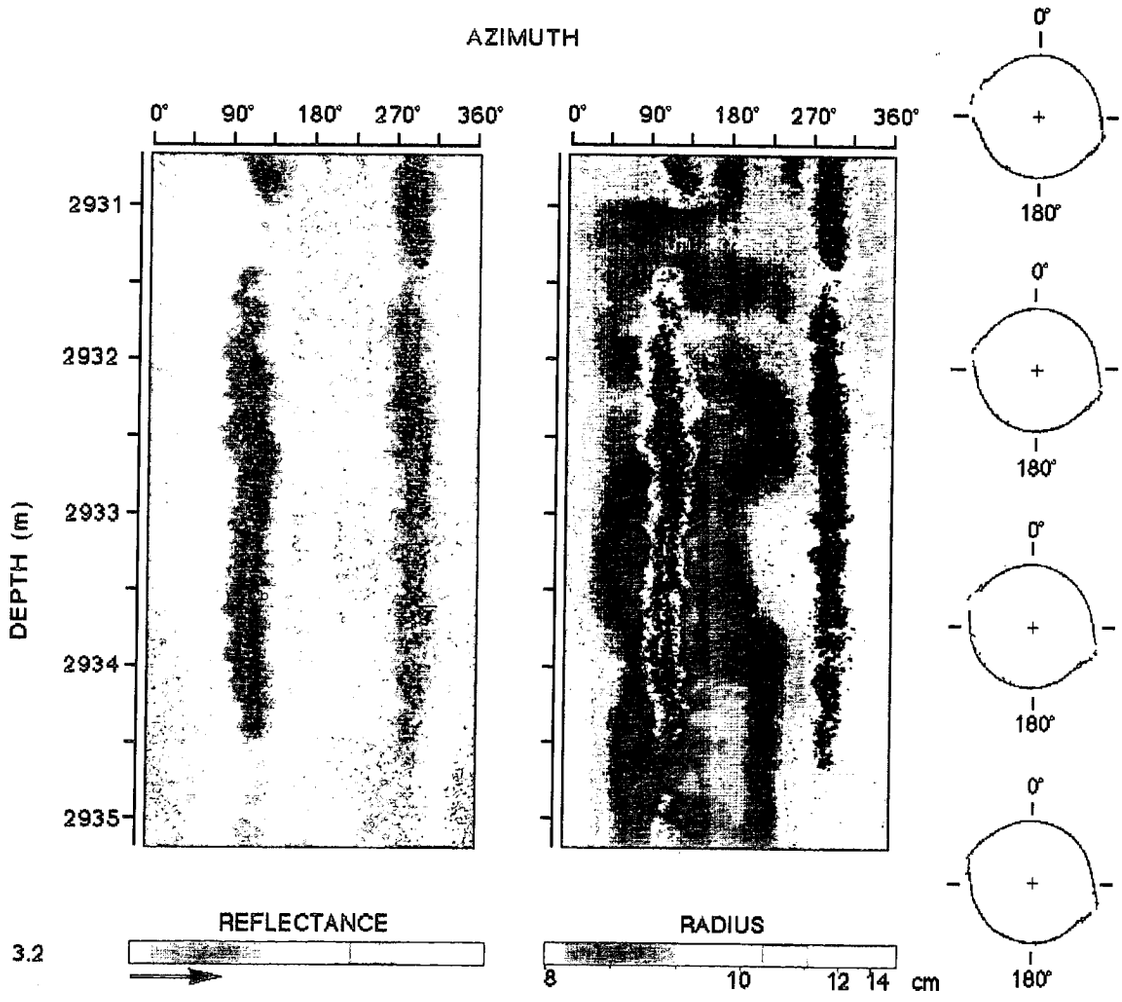

Figure 3.2 Reflectance and radius images and polar cross sections where borehole breakouts are oriented nearly orthogonal to those of Fig. 2.2.

(Byerlee and Lockner, 1988) can be ruled out. Based on these observations, it was concluded that by far the majority of borehole breakouts in the Cajon Pass wellbore are stress-induced, indicating the locus of the maximum compressive tangential stress at the borehole wall, and that their orientations are generally unaffected by rock type, strength anisotropy, instrumental malfunction or drilling operations. The primary source of breakout azimuth variations with depth should therefore be actual variations in the orientation of the principal stresses applied to the borehole.

As Fig. 3.1 clearly shows, variations in breakout azimuth occur on a wide range of wavelengths. Long wavelength azimuthal zonation is exhibited in several intervals, up to several hundreds of meters in length, in which breakout orientations are relatively stable, but distinctly different from each other (Fig. 3.3). Notably, each of these zones contributes a different component to the overall mean breakout azimuth.

A number of patterns of change in orientation and morphology of breakouts are observed at shorter wavelengths (Fig. 3.4): Gradual changes in azimuth with depth (in all images), discontinuous changes at fracture planes (b,c) or away from them (d, at 2895m), stoppage of borehole wall failure near fractures (b,d), local deviations from co-linearity of breakouts, abrupt or gradual changes in breakout azimuthal width and spiraling in opposite senses on either side of the wellbore (b). Note also the different length scales involved, from many tens of meters (Fig. 3.1), to several meters (Fig. 3.4a,d) to just a few centimeters (Fig. 3.4b,c). It is clear from Figures 3.1 through 3.4 that throughout the borehole there is a superposition of variations in breakout orientation at a wide variety of

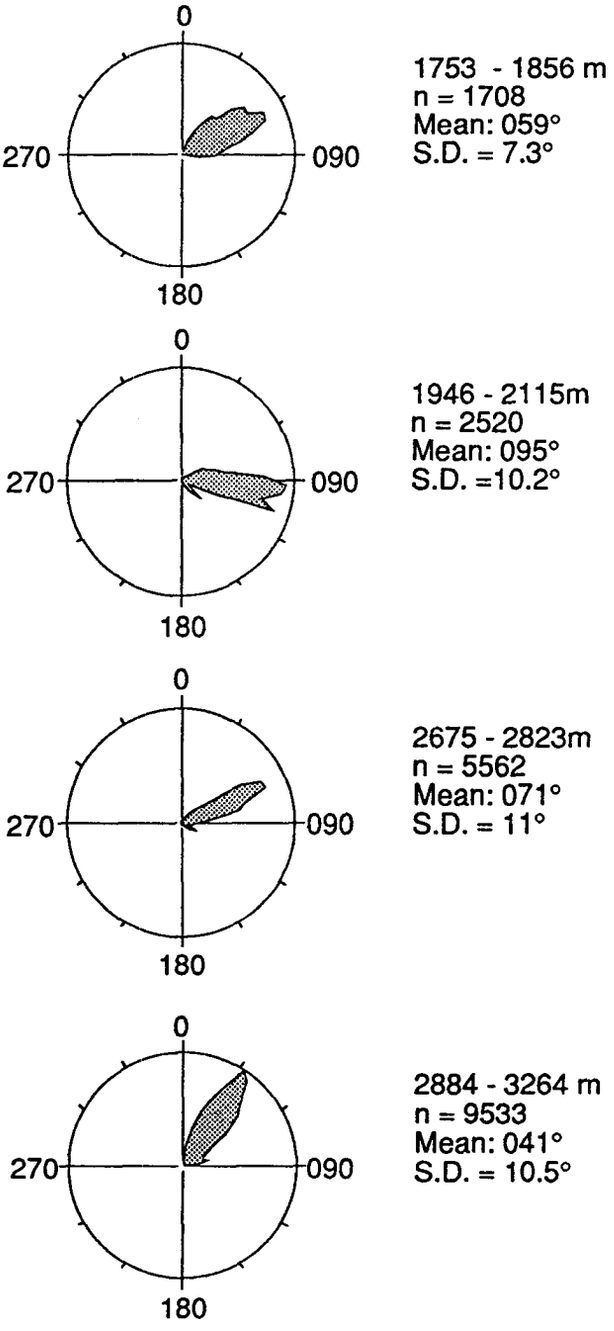

Figure 3.3 Orientation distribution of S_H in four intervals of the Cajon Pass borehole of relatively stable breakout orientations, indicating zonation at wavelengths of at least several hundred meters.

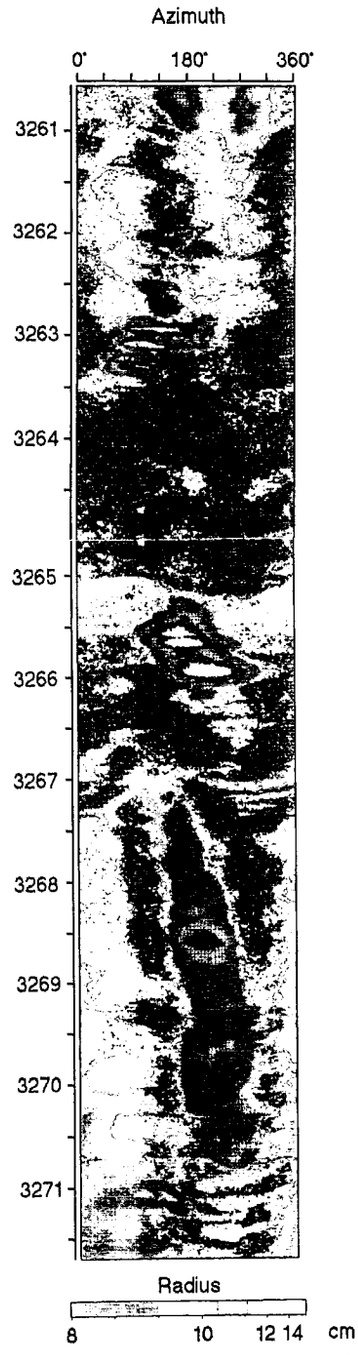

Figure 3.4a False color, split 360° image of the borehole wall relief. A major fault zone (which was also identified by alteration minerals retrieved from the wellbore) is penetrated from 3263m to 3267m, with the distinct fracture planes making sinusoidal traces on the split image. Several fractures at 3271m may be related to this fault zone as well. Borehole breakouts (represented by elongated dark zones) gradually change orientation over ~4m below the fault zone (3267-3271m) but retain a more or less steady orientation above it (above 3263m).

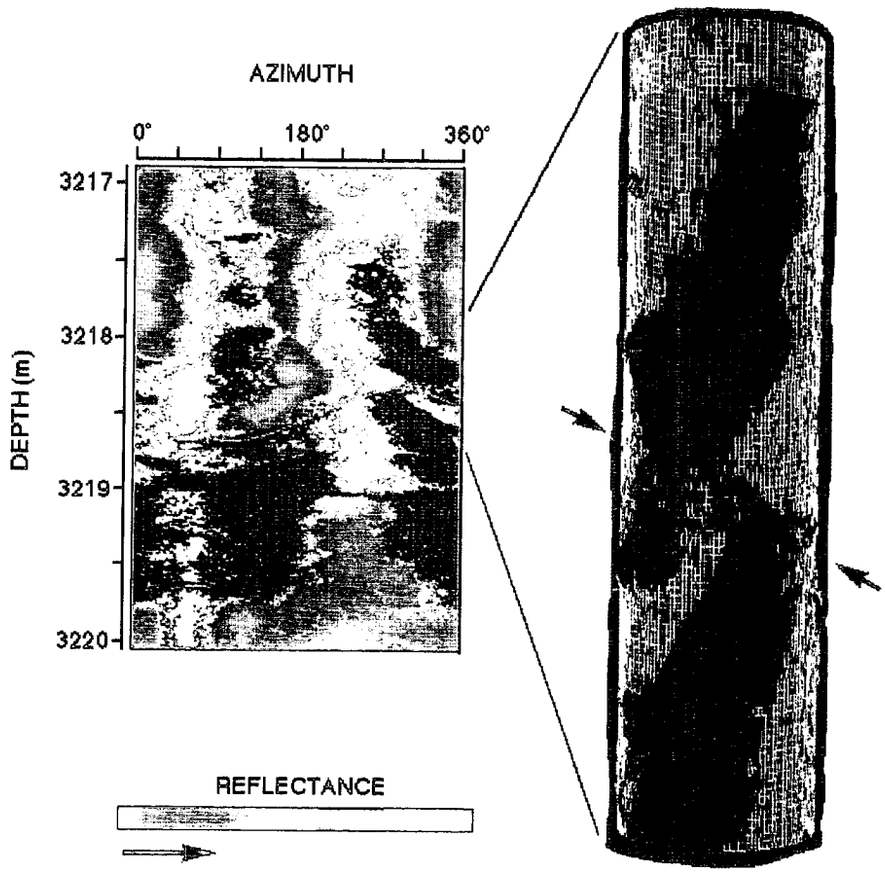

Figure 3.4b Split 360° image of the borehole wall relief from 3217-3220m. A distinct fracture plane is highlighted by a white sinusoid at about 3218.5m. The broken-out zone on the western side of the wellbore is changing azimuth gradually over a distance of about ±0.5m from the fracture. At the fracture plane itself, a discontinuous shift in breakout orientation occurs, in a sense opposite to that of the gradual rotation. These orientation changes are seen in a cylindrical view of the borehole relief (right, color-modulated by the reflectance amplitude).

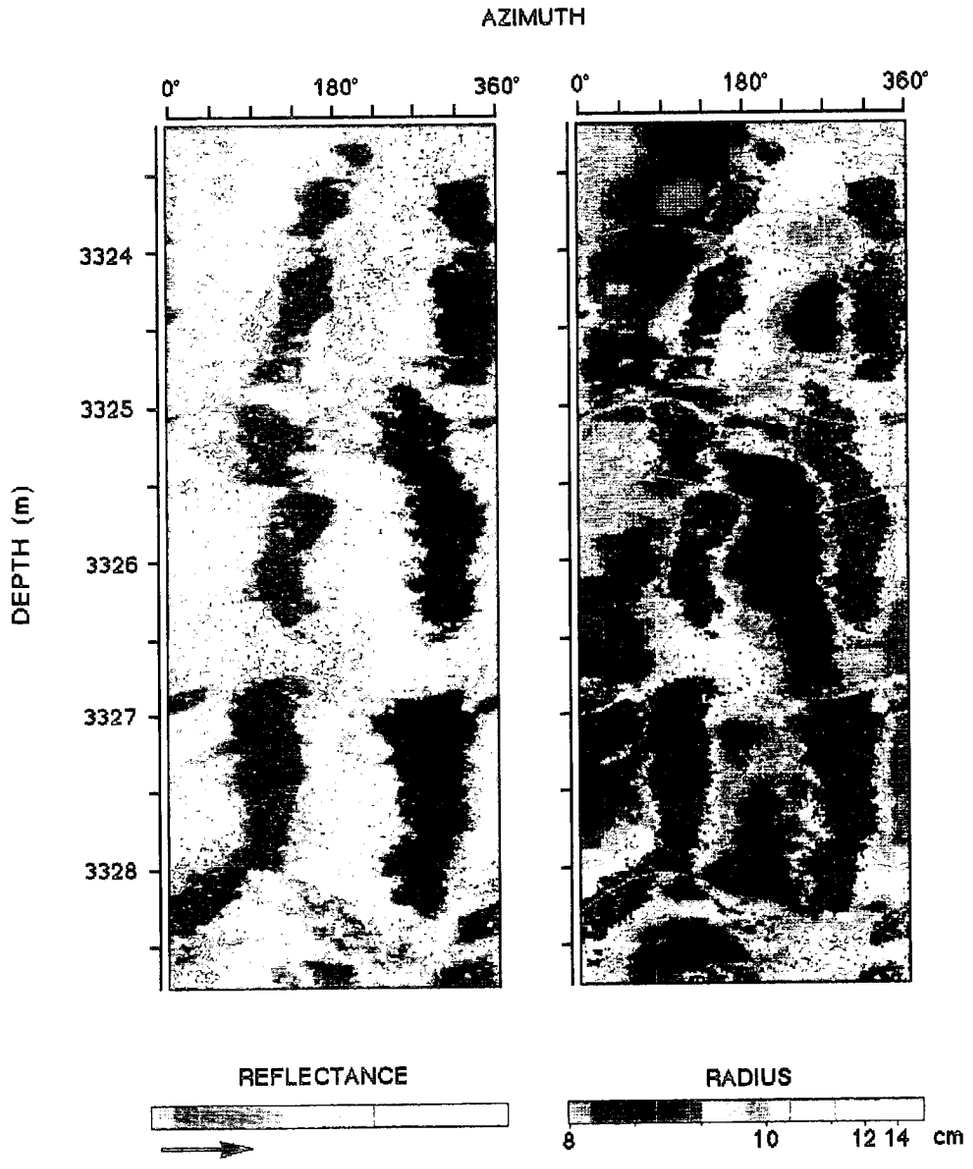

Figure 3.4c Split 360° images of the borehole wall reflectivity (left) and releif (right) from 3323.3-3328.7m in the Cajon Pass wellbore. Several distinct fracture planes (with sinusoidal appearance) are highlighted by white curves. Borehole breakouts are seen to change orientation gradually (e.g. around the fracture at 3325.5m) and discontinuously (the eastern breakout at the same fracture palne). They are supressed above hte fractures at 3325m and 3327m.

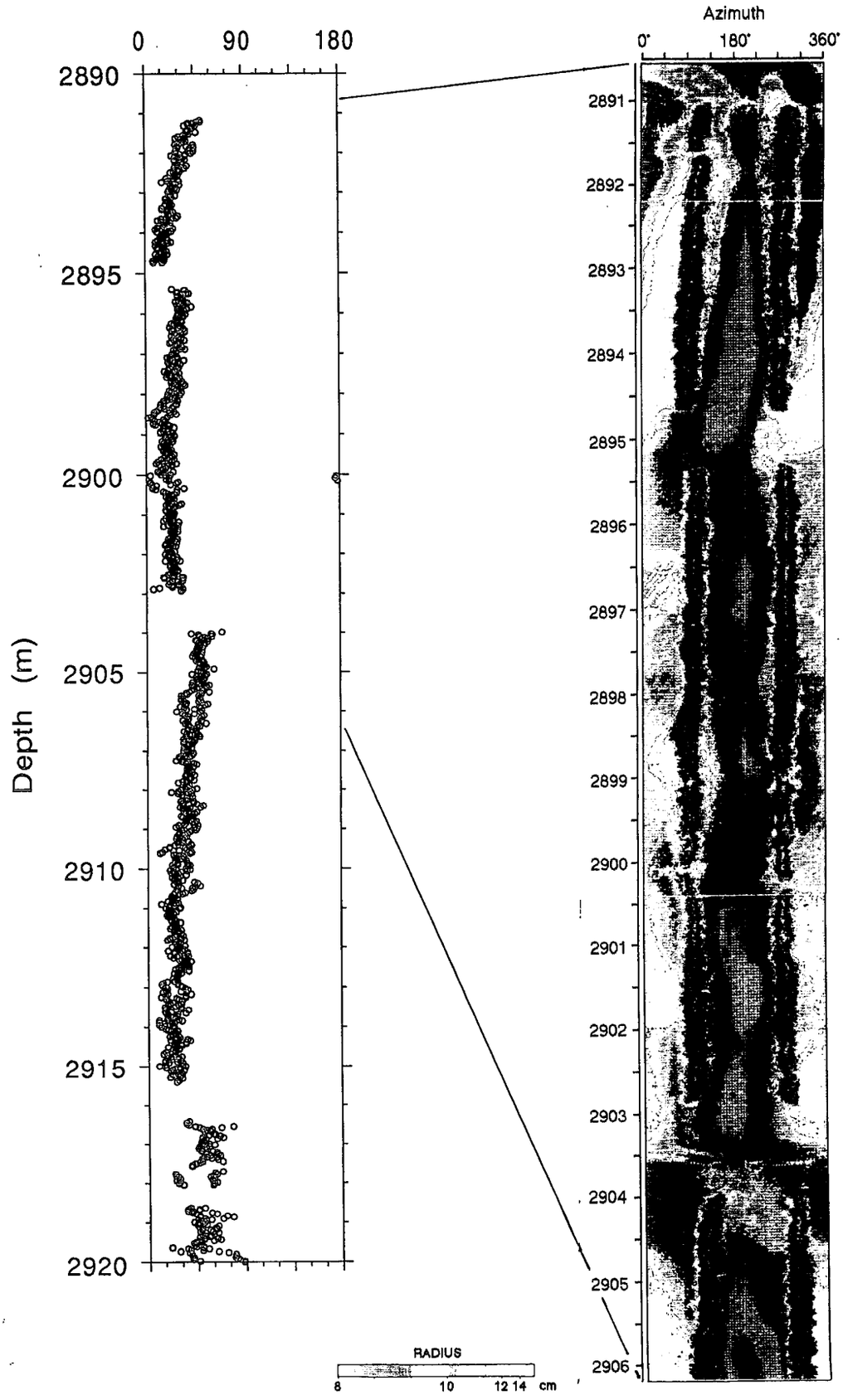
Azimuth
0°
180°
360°
0
90
180
Depth (m)
2890
2895
2900
2905
2910
2915
2920
2891
2892
2893
2894
2895
2896
2897
2898
2899
2900
2901
2902
2903
2904
2905
2906
RADIUS
8
10
12 14 cm

scales (e.g. Fig. 3.4d), at least up to wavelengths which make a substantial fraction of the total interval of breakout occurrence.

Another important observation is that in many places the features shown in Fig. 3.4 are associated with fracture planes which have been penetrated by the drillhole (inclined fractures form sinusoidal curves in split cylindrical views; see highlighted fractures in Fig. 3.4). Thus, breakout spiraling often initiates (or terminates) at fractures, and much (but not all) of the discontinuities occur at the fracture surfaces. Conversely, some gaps in continuously broken-out zones occur on either side of some pronounced fractures. The correlation between changes in Θ^* and fractures occurrence is also evident on a larger scale. Figure 3.5 shows the fracture frequency as a function of depth in the the lower part of the Cajon Pass well, as observed on the BHTV images (Barton and Zoback, 1990), compared with the section of the Θ^* orientation profile for the same depth interval. Clearly, the intervals of most dense fracturing in the lower 400m of the hole are associated with the most highly variable stress orientations.

Figure 3.6 shows four sections of the S_H^* profile, representing different length scales and exhibiting some of the most pronounced azimuth variations. The orientations of those fractures which are both reliably measured and clearly associated with S_H^* variations, are shown on lower hemisphere stereographic projections. Note the opposite senses of azimuth changes (Fig. 3.6b and d) and

Figure 3.4d Split 360° image of the borehole wall relief (right) and the resulting orientation profile of the apparent maximum horizontal compressive stress (left) in the depth interval 2891-2907m at Cajon Pass. A distinct fracture is seen at 2903m, surrounded by a zone of no borehole failure. An almost identical zone is seen at 2895m, but with observed fracture. In both cases the breakouts are shifted in orientation across the no-failure zone. A fracture at 2900m is associated with breakout orientation change and narrowing of breakouts, in particular on the eastern side of the wellbore.

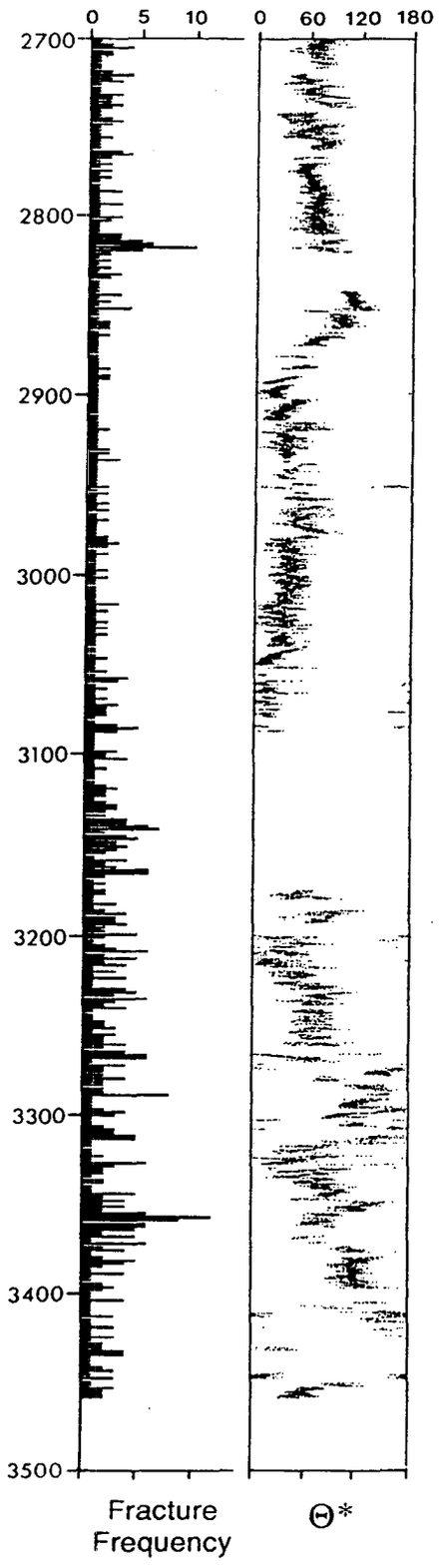

Figure 3.5 Fracture frequency per meter (left; Barton, personal communication; Barton and Zoback, 1990) compared to the orientation Θ^* of the apparent maximum horizontal compressive stress in the lower 400m of the Cajon Pass borehole.

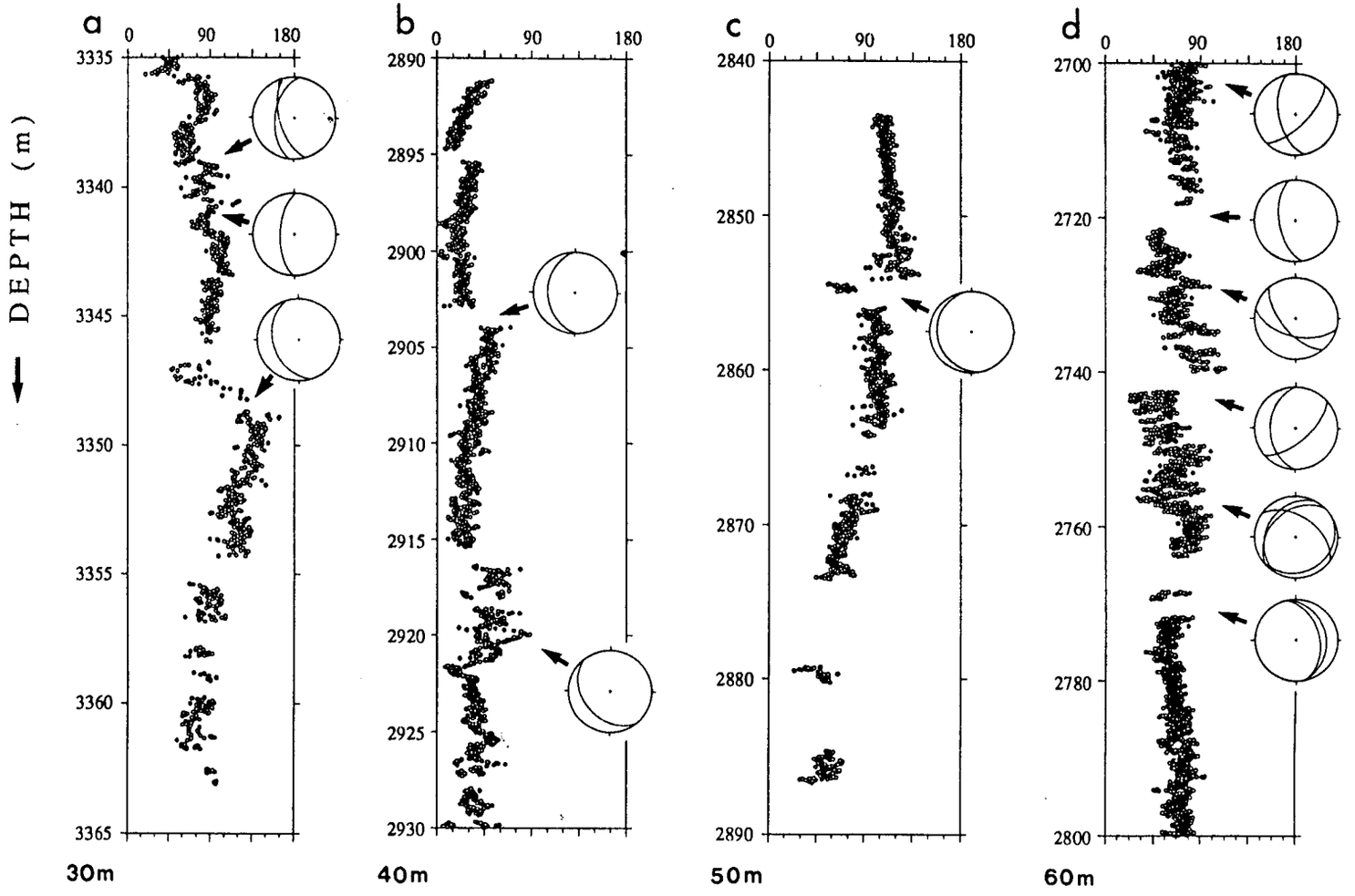

Figure 3.6 Sections of the Θ^* profile exhibiting the orientation variations described above. The geometry of fractures associated with changes in breakout orientation are shown in lower hemisphere stereographic projections. Note the different length scales indicated at the bottom of each panel.

the superposition of various wavelengths (3.6a and d). The measured fractures generally fall into two groups, one striking NNW (seen in all panels), the other about NE (3.6d).

In light of the wide fluctuations in breakout orientations described above, the overall orientation distribution of wellbore breakouts (i.e. for the entire data set of Fig. 3.1) is surprisingly confined (Fig. 3.7). The vectorial mean azimuth of S_H^* is 057°, with a standard deviation of 19°. The distributions on opposite sides of the borehole are generally co-linear, suggesting, again, that anisotropy does not have a significant effect on the mean breakout orientation.

In conclusion, based on the observations summarized above, the shallow crust at Cajon Pass is seen to contain a pervasive distribution of fracture-related stress perturbations, over a wide range of scales in amplitudes and wavelengths. These faults have therefore been active in recent geological times, leaving stress signatures which are superimposed on the average ambient stress field.

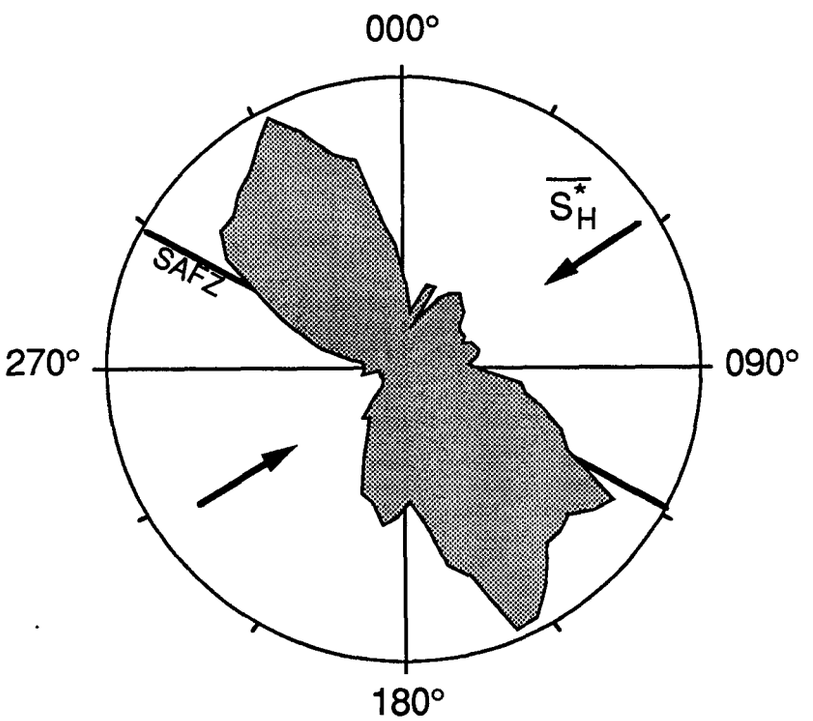

Figure 3.7 Overall orientation distribution of borehole breakouts between 1750 and 3460m in the Cajon Pass wellbore. The mean S_H^* azimuth is 057°, with circular standard deviation of 19° (n=32616).

4. CRUSTAL STRESS HETEROGENEITY AT CAJON PASS

4.1 Mechanics of fault-induced stress perturbations

The data presented above suggests that, at least on length scales shorter than that of the entire breakout occurrence interval (1710m), stress heterogeneity is a pervasive feature of the shallow crust near Cajon Pass. This observation is in general agreement with the variability of stress magnitudes and orientations documented in the western Mojave Desert, as described in Ch.1. It was also concluded above that breakouts in the Cajon Pass wellbore are distorted due to local stress fluctuations associated with active faults. Several differing mechanisms may then be suggested for generating the stress perturbations, depending on the temporal relations between fault slip and drilling (Shamir et al., 1990):

1. Fault displacements may be of tectonic origin, i.e. preexisting at the time of drilling. This is a static case, in which fault slip is temporally decoupled from the drilling process.

2. Slip across limited fracture areas occurs during drilling. This may be the case for faults which are near-failure prior to drilling and the slip distribution should be localized near the borehole. Such displacements may be induced either by the wellbore stress concentration (in which case slip occurs as the drillhole penetrates the fracture) or due to the bottom hole stress concentration (in which case slip occurs, prior to penetration, as the drill bit approaches the fault plane). An auxiliary factor in either case may be an increase in pore fluid pressure around the wellbore due to the high pumping pressure into the well during drilling. In the case of drilling-induced slip, a dynamic interaction takes place between the drilling process and fault rupture.

3. Discontinuity in some stress components may occur across material property boundaries (e.g. gouge-filled fractures, veins, migmatitic zones, etc.). As mentioned above, the major detectable lithological transitions did not have a measurable effect on breakout orientation but it is unknown whether this mechanism is locally significant.

The first case, that of preexisting tectonic displacements under a prescribed remote stress state, is analyzed below. A fault penetrated by the drillhole is considered, and the total stress applied to it is a superposition of the remote stress state and the local fault-induced stress. The change in the borehole state of stress, as a function of distance from the fault, is then computed. In the context of the theory of elasticity, it would intuitively be expected that wavelengths of stress perturbations in the hole should scale with the amount of slip and the slip patch area of the associated faults. In that case, the very short wavelength perturbations in Fig. 3.4. would indicate very small slip patches which are localized to the vicinity of the borehole, i.e. drilling-induced.

In the model, a planar square fault of dimension 2L is assumed to be buried in a semi-infinite, isotropic, linearly elastic medium which is otherwise continuous and mechanically homogeneous. For illustrative purposes, a fault is considered that strikes north-south and dips to the west, generally representing the stress-perturbing faults of Figure 3.6. The remote stress state σ_{ij}^{∞} is taken equal to that determined by hydraulic fracturing at a depth of 2.66km in Cajon Pass (Zoback and Healy, submitted manuscript, 1990). The measured horizontal least compressive stress is $S_h \approx 33$MPa and the calculated S_H is 70.2MPa (there, Table 1). The lithostatic vertical stress at that depth ($S_v \approx$ 72MPa , ρ=2700 kg/m^3) is assumed to be a principal stress. S_H is taken to be oriented 057°, as

the mean S_H^* in Cajon Pass, and stress components are then derived by simple Euler angle rotations (e.g. Jaeger and Cook, 1976, p. 49). Slip on the fault is assumed to occur parallel to the maximum resolved shear stress. Its rake is determined analytically (Bott, 1959) to be 13°, 19° and 25° in an oblique strike-slip/normal sense for fault dips of 30°, 45° and 60°, respectively and the prescribed remote stress field.

Once a slip vector orientation which is kinematically compatible with the ambient stress field has been determined, the solution for the 3-dimensional elastic fields produced by a buried screw dislocation (discussed further in ch.5) is utilized (DIS3D; Dunbar [1984] and Erickson [1986]), to obtain the local, fault-induced stress field σ_{ij}^f, whose magnitude and extent depend on the prescribed displacement and the fault size. Then, a vertical borehole of radius R<<L is introduced, piercing the fault plane far from its edges (Fig. 4.1). By superposition, the total stress applied to the borehole is

$$\sigma_{ij}^{tot} = \sigma_{ij}^f + \sigma_{ij}^{\infty} \tag{4.1}$$

The principal directions of σ_{ij}^{tot} are, in general, inclined with respect to both the remote principal stresses and the borehole axis. Eqs. 1.1-1.4 become

$$\sigma_{\theta\theta}^{tot} = \sigma_{11}^{tot} + \sigma_{22}^{tot} - 2\left(\sigma_{11}^{tot} - \sigma_{22}^{tot}\right)\cos 2\theta - 4\sigma_{12}^{tot}\sin 2\theta - P_0 \tag{4.2}$$

$$\sigma_{zz}^{tot} = \sigma_{33}^{tot} - 0{,}5\left(\sigma_{11}^{tot} - \sigma_{22}^{tot}\right)\cos 2\theta - \sigma_{12}^{tot}\sin 2\theta \tag{4.3}$$

$$\sigma_{\theta z}^{tot} = 2\left(\sigma_{23}^{tot}\cos\theta - \sigma_{31}^{tot}\sin\theta\right) \tag{4.4}$$

$$\sigma_t^{tot} = \frac{\sigma_{\theta\theta}^{tot} + \sigma_{zz}^{tot}}{2} + \frac{1}{2}\sqrt{4\tau_{\theta z}^2 + \left(\sigma_{\theta\theta}^{tot} - \sigma_{zz}^{tot}\right)^2} \tag{4.5}$$

and the inclination of σ_{tmax}^{tot} with respect to the borehole axis is given by

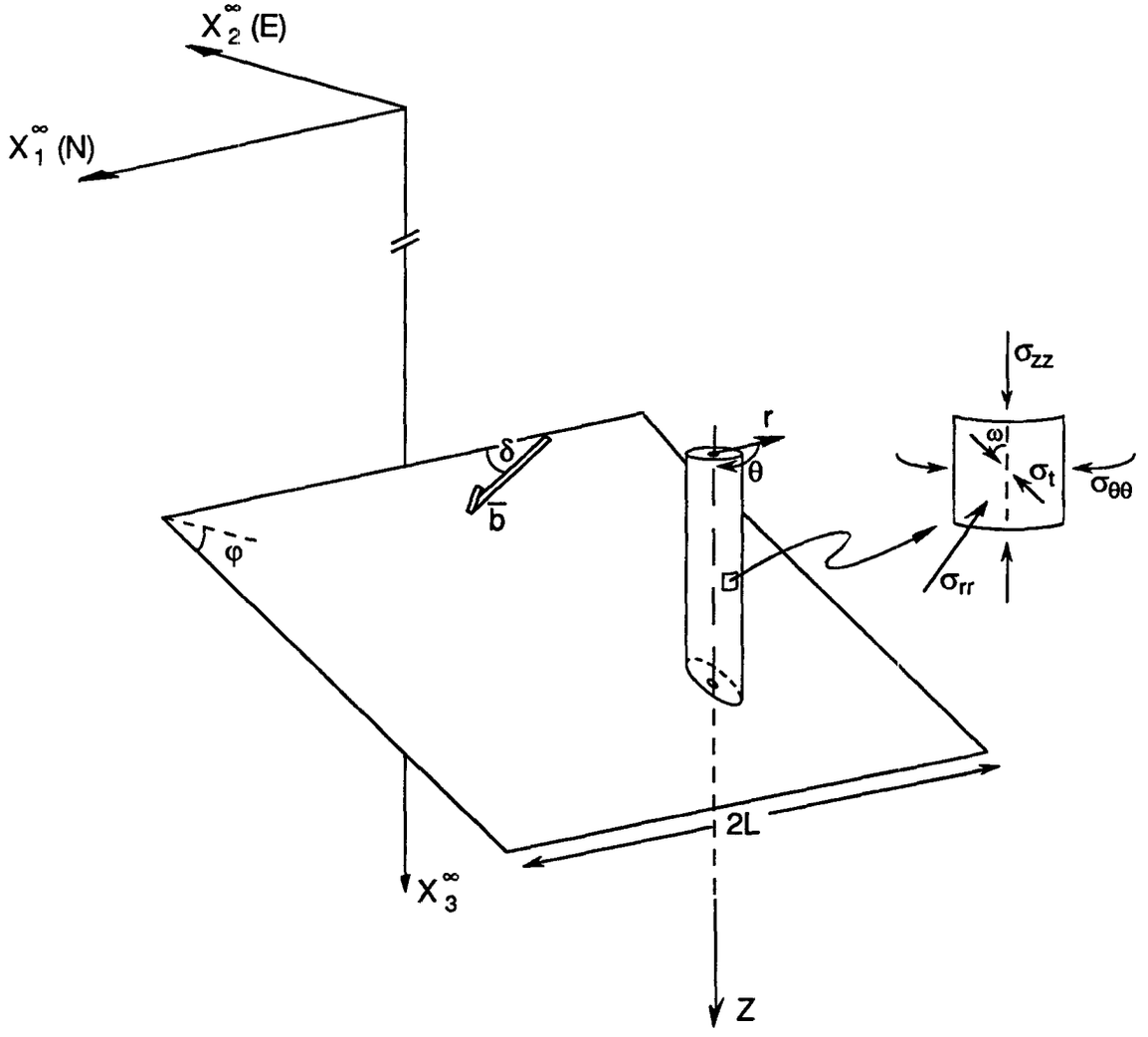

Figure 4.1 Model for the mechanics of fault-induced borehole stress perturbations (schematic, not to scale). The fault is buried at x_3 = 2.66 km and strikes 180°. Its mean slip vector b plunges at a rake δ, which depends on the ambient stress state and the fault dip ϕ.

$$\omega_t^{tot} = \frac{1}{2} \tan^{-1}\left(\frac{2\,\tau_{\theta z}^{tot}}{\sigma_{\theta\theta}^{tot} - \sigma_{zz}^{tot}}\right) \quad . \tag{4.6}$$

The relaxed analytical solution for the polyaxial state of stress around a borehole (App. 1; Hiramatsu and Oka, 1968) assumes that the stresses applied to the borehole are uniform. In the case analyzed here, the non-uniformity of the stress near the fault is actually the property we are trying to investigate. However, for L>>R, the change in any stress component along borehole distances of 5 to several tens of borehole radii (for the range of M_0 analyzed here, but excluding very steep faults), as well as across the borehole diameter does not exceed about 5%. Therefore, Eqs. 4.2-4.6 are used to give discrete averages of the state of stress along an ~8L long borehole segment centered on the fault. Then, the maximum tangential stress in each borehole circumference, σ_{tmax}^{tot} (Eq. 4.5), its inclination with respect to the borehole axis, ω_{tmax}^{tot} (Eq. 4.6), and the azimuth at which it occurs in the borehole, Θ_{tmax}^{tot}, are calculated along the analyzed borehole segment. In the examples below, σ_{tmax}^{tot} is normalized to σ_{tmax}^{∞}, the maximum tangential stress which would occur at the borehole wall in the absence of a fault. Fluid pore pressure near the borehole wall is assumed to be hydrostatic (In Cajon Pass it was found to be slightly super-hydrostatic; Coyle and Zoback, 1988).

The fault parameters are conveniently described by the average scalar seismic moment $M_0=\mu A\bar{b}$ (where μ=rigidity, A=fault area, $\bar{b}$=average slip vector), which is commonly determined from the amplitude of long-period surface waves. Using M_0 and the source radius r (as determined from seismic spectral parameters), the stress drop is commonly calculated as

$$\Delta\sigma = \frac{7\ M_0}{16\ r^3} \qquad (4.7)$$

from models of planar, uniform faults (Kanamori and Anderson, 1975). For events larger than about M_L=3, seismic moments generally scale with source radii, resulting in earthquake stress drops which are restricted to the range 1-200 bar, over 8±1 orders of magnitude of seismic moment (e.g. Hanks, 1977). There is, however, abundant evidence that this self-similarity does not persist for low moment events (e.g. Chouet et al., 1978; Rautian et al., 1978). Archuleta et al. (1982) showed that for earthquakes with seismic moments higher than about 10^{21} dyne-cm (M_L~ 3.2) from the Mammoth Lake sequence (1980), as well as a variety of other environments (Fig. 4.2a) have seismic moments which scale with the source radii (M_0 decreases by 3 orders of magnitude for 1 order of magnitude decrease in source dimension), and consequently nearly constant stress drops (10-100 bars). At lower moments, however, the source radii change very slowly with M_0 but the stress drop decreases (Fig. 4.2a). The data reaches seismic moments as low as 10^{18} dyne-cm and source dimension in the range 30-100m. This same pattern was observed for induced seismicity data from the Monticello reservoir, South Carolina (Fletcher, 1982), where small seismic events in the depth interval 0.5-1.4km, produced moments in the range 10^{17} to 5×10^{18} dyne-cm, associated with source diameters in the range 44-112m. Data measured in the Anza seismic array, along the San Jacinto fault (Fletcher et al., 1987), show source radii limited to the range 30-100m for events with M_0=10^{17} to 10^{20} dyne-cm. When data suspected of being attenuated were deleted from this set, the recalculated source radii are somewhat less constrained but still show a decrease in stress drop with decrease in seismic moment (Fig. 4.2b). Aki (1987) used seismograms obtained in a 1.7km deep

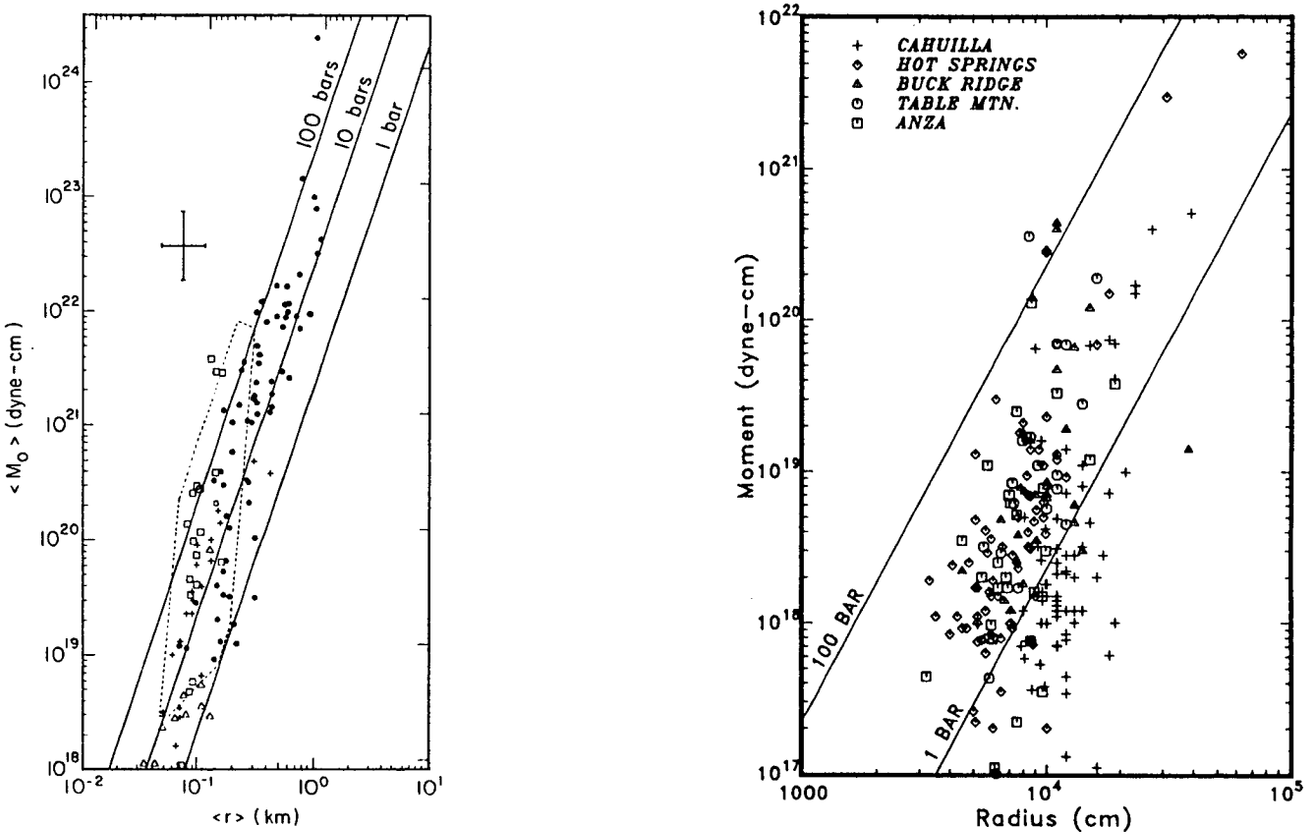

Figure 4.2 (a) Seismic moment vs. source radius for Mammoth Lake earthquakes (Archuleta et al., 1982; solid circles); Oroville, California, aftershocks (Fletcher, 1980; triangles); central California earthquakes (Bakun et al., 1976; squares); South African mine tremors (Spottiswoode and McGarr, 1975; pluses); San Fernando, California, aftershocks (Tucker and Brune, 1973; area in dashed line) (From Archuleta et al., 1982). (b) Seismic moment vs. source radius (excluding data suspected to be attenuated) for seismicity off the San Jacinto Fault near Anza, California, 1982-1984 (Fletcher et al., 1987).

borehole station in the Newport-Inglewood fault zone to check whether indeed the moment-radius scaling breaks down at the low M_0 range. He concluded that the observed frequency-magnitude relation departs from self-similarity for earthquakes with magnitude smaller than 3, coinciding with the above mentioned pattern of the moment-radius relation (i.e. earthquakes below magnitude 3 tend to have nearly constant source radii). The breakdown may mean a minimum source size with no minimum moment (Aki, 1984), that is, a diminishing slip vector magnitudes across finite size faults.

Following these observations, and without an understanding of the relation between the seismologically-determined source parameters and the actual near-field properties of the slipping fault, the model calculations are carried out for a constant fault dimension (L=53m) corresponding to a circular source radius of 60m and for seismic moments from 10^{17} to 10^{21} dyne-cm. As expected in the context of linear elasticity, the fault-induced stresses scale with fault size and slip. Notably, these seismic moments result in stress drops (calculated from Eq. 4.7) of 0.2-2000 bars (0.02-200 MPa), respectively. The higher values are inconsistent with the generally observed, seismologically-determined stress drops of up to about 20MPa (Fig. 4.2) and with the actual available shear stress at Cajon Pass based on the measured stress magnitudes (Zoback and Healy, 1991) and conventional frictional strength of rocks (Byerlee, 1978). This problem will be discussed below. Also, since most parameters for the actual stress fluctuations in the Cajon Pass well are unconstrained (e.g. fault sizes, seismic moments, stress drops), the results shown below are meant to demonstrate the range of possible patterns of breakout occurrence associated with active faults, but are not intended to model specific cases.

Figures 4.3a and 4.4a show the changes in normalized tangential stress at the borehole wall, as function of distance from the fault, for seismic moments above and below about 10^{20} dyne-cm, respectively. Figures 4.3b and 4.4b show the azimuths at which the maximum tangential stress will occur in the borehole, for the same ranges of M_0.

Scaling patterns. For the geometry of faulting considered, there is clear change in the scaling pattern of σ_{tmax}^{tot} at about $M_0=10^{20.5}$ dyne-cm. In the low-M_0 range (Fig. 4.3a), the total tangential stress near the fault *decreases* with increasing fault slip. This pattern is reversed in the high-M_0 range (Fig. 4.4a), where σ_{tmax}^{tot} *increases* with increasing slip. In the context of linear elasticity, however, fault-induced stresses scale with the amount of slip, so that, for example, the shear stress induced parallel to a screw dislocation lying in the x_1-x_3 plane is $\tau_{13}=(-\mu b/2\pi)\left\{x_2/(x_1^2+x_2^2)\right\}$, where b is its Burgers vector (Hirth and Lothe, 1982, p. 60).

To illustrate the source of this pattern, each of the tangential stress contributions (remote, σ_t^{∞}, fault-induced, σ_t^f, and total, σ_t^{tot}) is plotted (Fig. 4.5) along a borehole circumference for the low-M_0 (a) and high-M_0 (b) cases. As the fault slip was taken to be parallel to the maximum resolved shear stress (i.e. compatible with the ambient stress field), the σ_t^f maxima around the borehole are nearly orthogonal to those of σ_t^{∞}, i.e. σ_t^f is the tangential stress drop. As long as the maximum fault-induced tangential stress is lower than the remote (i.e. $\sigma_{tmax}^f < \sigma_{tmax}^{\infty}$; Fig. 4.5a), the total tangential stress is reduced relative to its ambient value (as in Fig. 4.3a), and its azimuth varies mildly about Θ_{tmax}^{∞}. In this case greater slip results in *lower* total tangential stress σ_t^{tot}. However, when

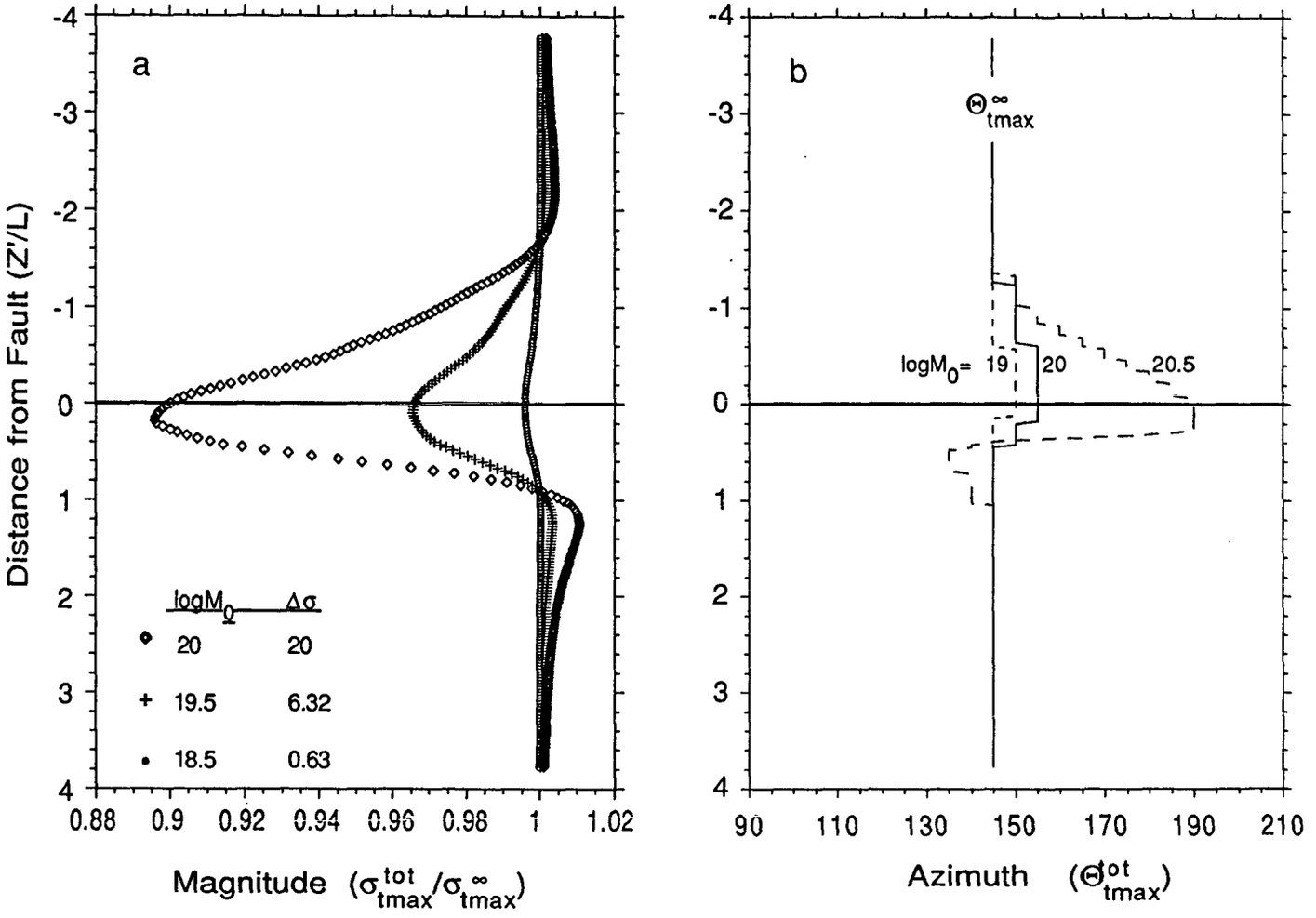

Figure 4.3 Normalized maximum tangential stress at the borehole wall (a) and its azimuth (b), as a function of normalized distance from a penetrated fault, for seismic moments of $10^{18.5}$-10^{20} dyne-cm and stress drops of 0.63-20MPa. Sharp steps in Θ^{tot}_{tmax} represent discontinuous orientation changes.

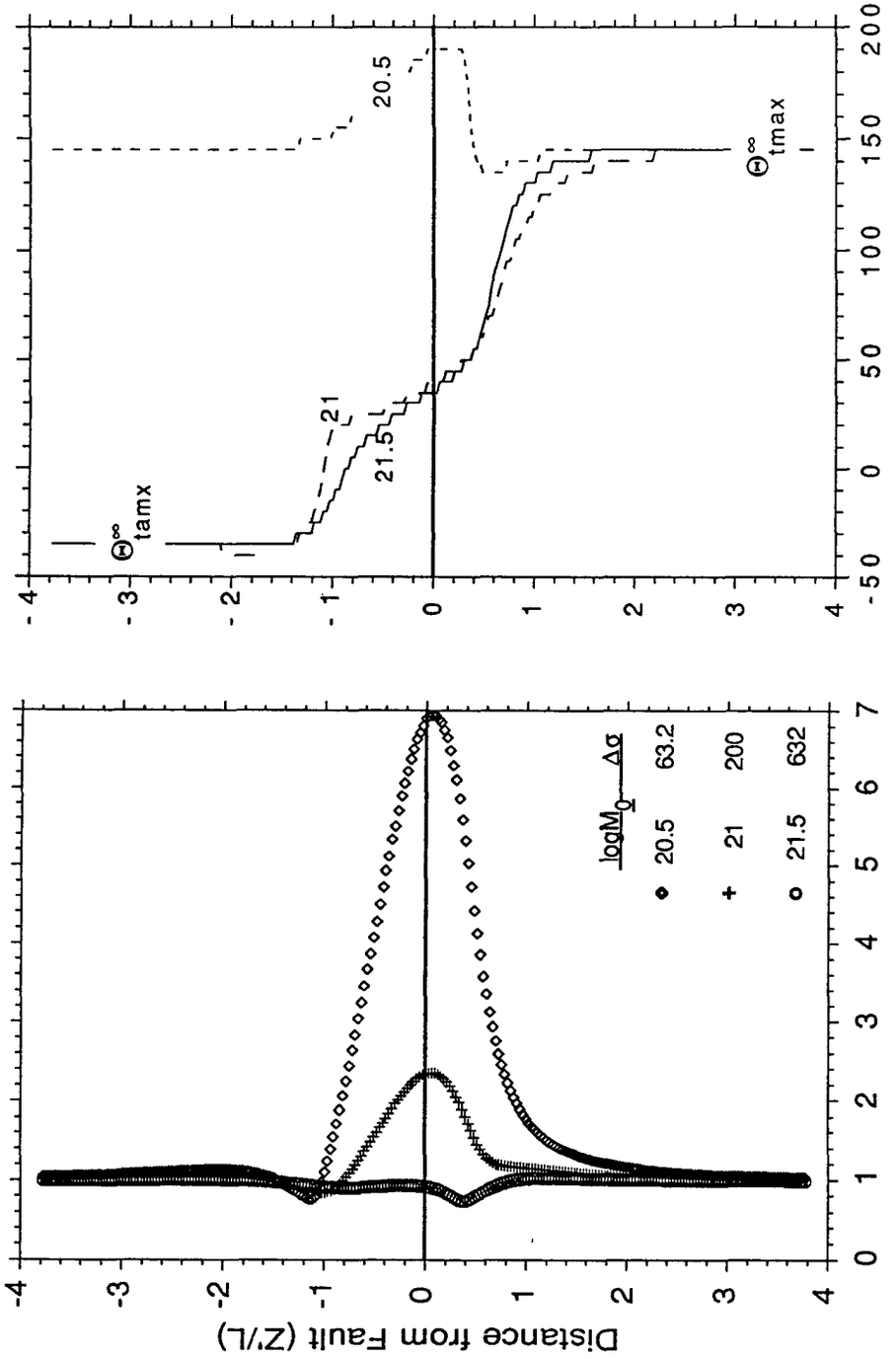

Figure 4.4 Same as Fig.4.3, for seismic moments above of $10^{20.5}$-$10^{21.5}$ dyne-cm and stress drops of 63.2-632 MPa. Note the full 180° rotation in the azimuth of the borehole stress concentration near faults of extremely high stress drop.

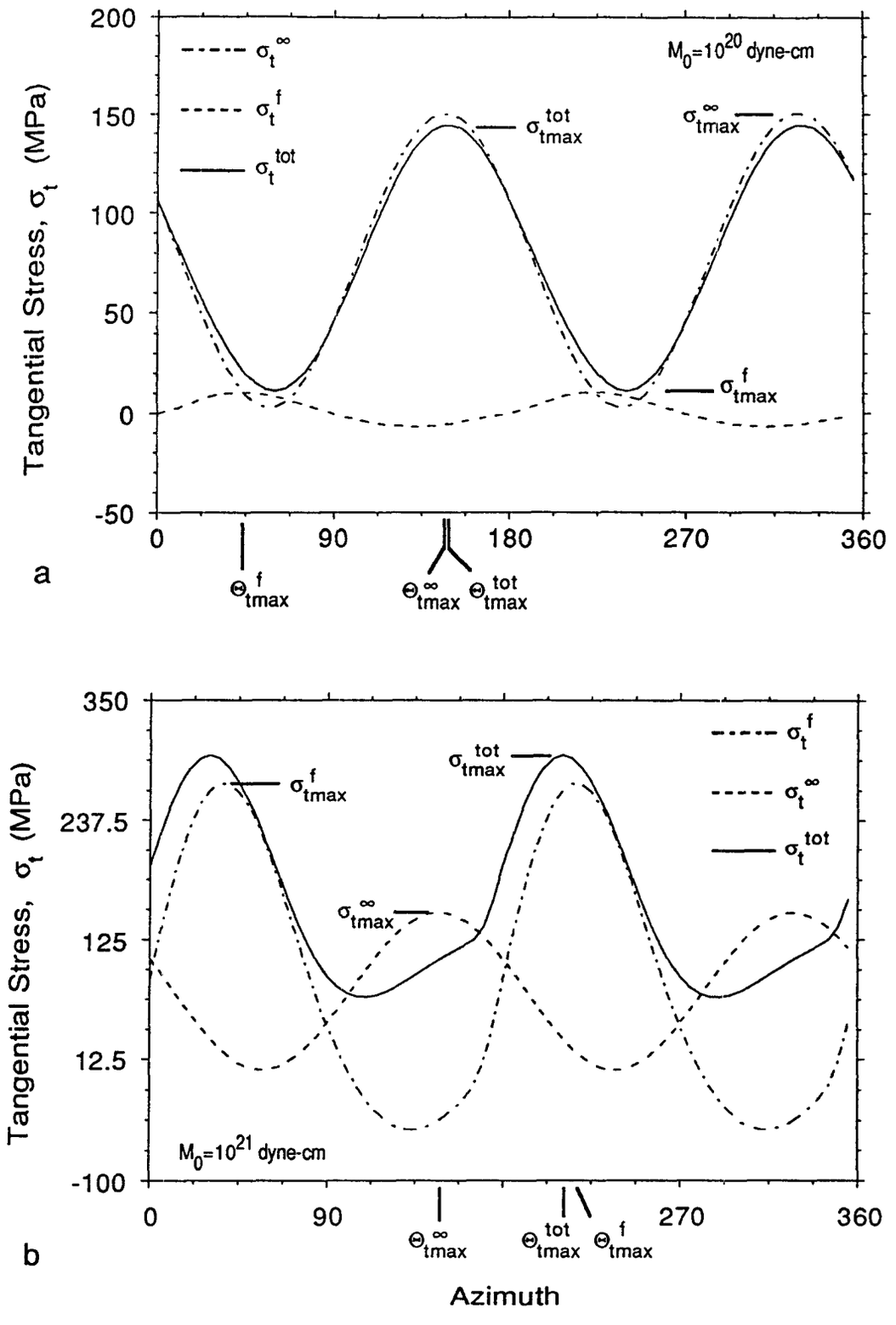

Figure 4.5 Variation of the ambient (σ_t^{∞}), fault-induced (σ_t^{f}) and total (σ_t^{tot}) tangential stress around a borehole circumference, for $M_0=10^{20}$ (a) and 10^{21} (b) dyne-cm.

$\sigma^{f}_{tmax} > \sigma^{\infty}_{tmax}$ (Fig.4.5b), the total tangential stress becomes dominated (in both magnitude and orientation) by the fault-induced stress, and greater slip results in *higher* total tangential stresses (As in Fig. 4.4a). Thus, the change in scaling of the re-distributed borehole stresses near active faults depends on the relative magnitudes of the stress drop and the ambient stresses.

Effect of rock strength. As mentioned in Ch. 1, the compressive strength of the dominant Cajon Pass rock type (gneissic-granidiorites) is in the range 100-204 MPa (Vernik and Zoback, 1990; Moos and Zoback, 1990). The ambient stress state used for the model calculations results in $\sigma^{\infty}_{tmax} \cong 150MPa$, and wherever C<150MPa breakouts are expected at an azimuth of Θ^{∞}_{tmax}=145°. If, for example, C=148.5MPa (=$0.99\sigma^{\infty}_{tmax}$; left side of Fig. 4.6) then breakouts near a fault of $M_{0=10}{}^{20}$ dyne-cm will step discontinuously and be suppressed near the fault plane (Fig. 4.6, right). If C=138MPa (=$0.92\sigma^{\infty}_{tmax}$), the breakouts follow the orientation of the ambient maximum tangential stress and are inhibited along a borehole section ~2L in length (Fig. 4.6, center) near the fault plane. Thus, a typical effect of low-M_0 faults, when $C < \sigma^{\infty}_{tmax}$, is stoppage of failure near the fault and possibly discontinuous azimuth changes. Overall, the azimuth changes associated with low-M_0 faults are up to several tens of degrees and very low moment slip patches (e.g. drilling-induced slip) are probably undetectable.

In Fig. 4.4, seismic moments of $10^{20.5}$, 10^{21} and $10^{21.5}$ dyne-cm were used to demonstrate the stress amplification near high-M_0 faults. By Eq. 4.7, these moments result in stress drops of 64, 200 and 640 MPa, respectively. If such

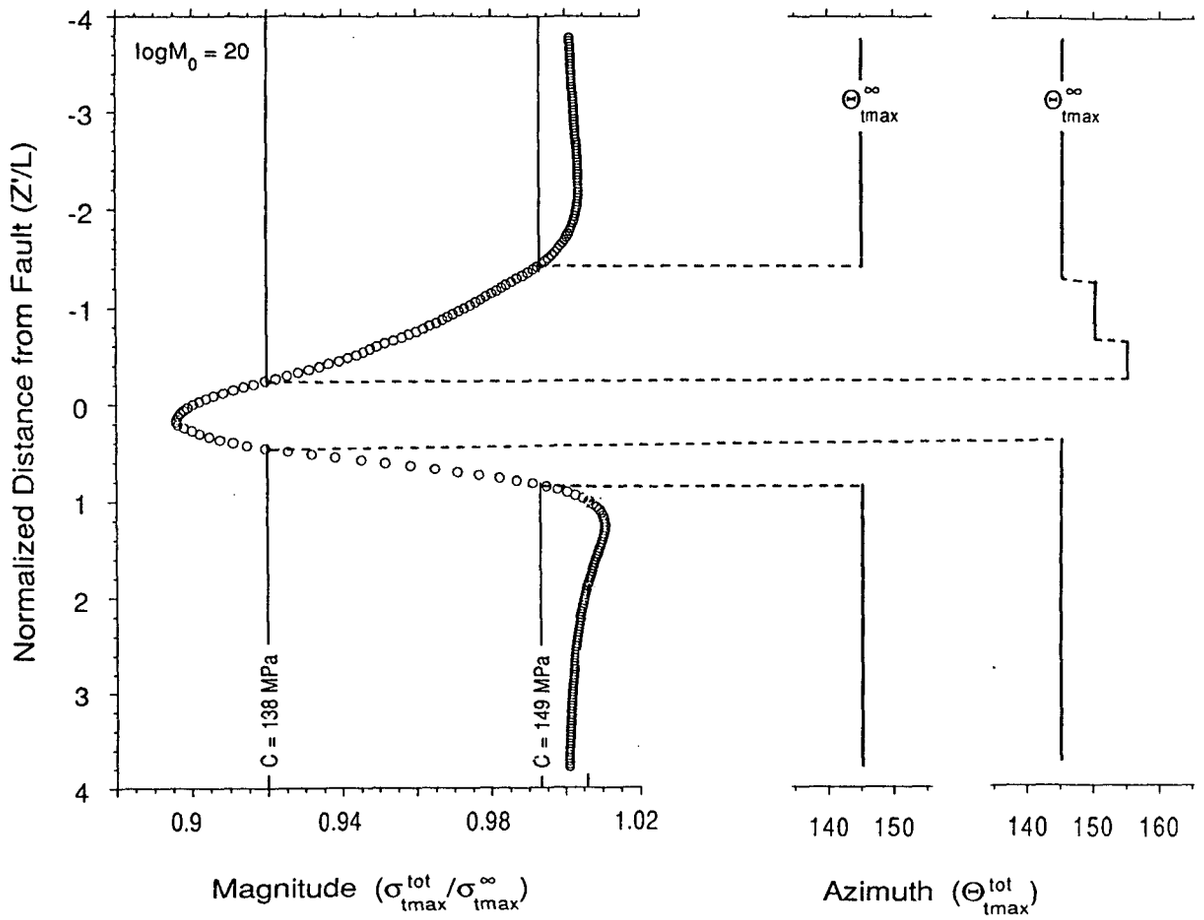

Figure 4.6 Effect of rock strength on the extent of breakout occurrence near a fault of $M_0=10^{20}$ dyne-cm (stress drop of 20 MPa). The breakout orientation expected soley due to the ambient stress field is $\Theta^{\infty}_{tmax}=145°$. For C=149MPa, the total maximum tangential stress drops below hte rock strength over a ~2L zone surrounding the fault plane and a gap in breakout occurrence is expected around the fault crossing. For lower strengths values, a combination of breakout orientation changes and gaps would occur.

high seismic momens, which have not been detected by far-field observations, exist locally (as discussed below), then they should induce amplified tangential stress at their vicinity. These would be associated with continuously spiraling breakouts near the fault plane, along depth intervals whose lengths depend on the rock strength (Fig. 4.7) and M_0. If extreme local stress drops do not exist, then all the observed variations in breakout orientation should be explained by tangential stress drops near the so-called low-M_0 faults.

Wavelengths of stress perturbations. The wavelengths of stress perturbations can be defined for the purpose of this discussion as the distance over which a disturbance of the stress field persists (although not necessarily observed in practice). As shown above, breakout occurrence near low-M_0 faults may be sporadic and although some dependence of wavelength on M_0 is seen above the fault in Fig. 4.3b, it would be too small to detect in a breakout analysis. For high-M_0 faults, on the other hand, there is a clear dependence of perturbation wavelength on M_0 below the fault in Fig. 4.4b (in spite of the constant fault dimension) but, evidently, whether or not this shows up depends also on the location and angle at which the borehole penetrates the fault. In general, it seems that once the high-M_0 pattern becomes dominant, perturbation wavelengths increase with increasing seismic moments and stress drops. Whether this will actually be observed, however, depends on the specific rock strength, as discussed above.

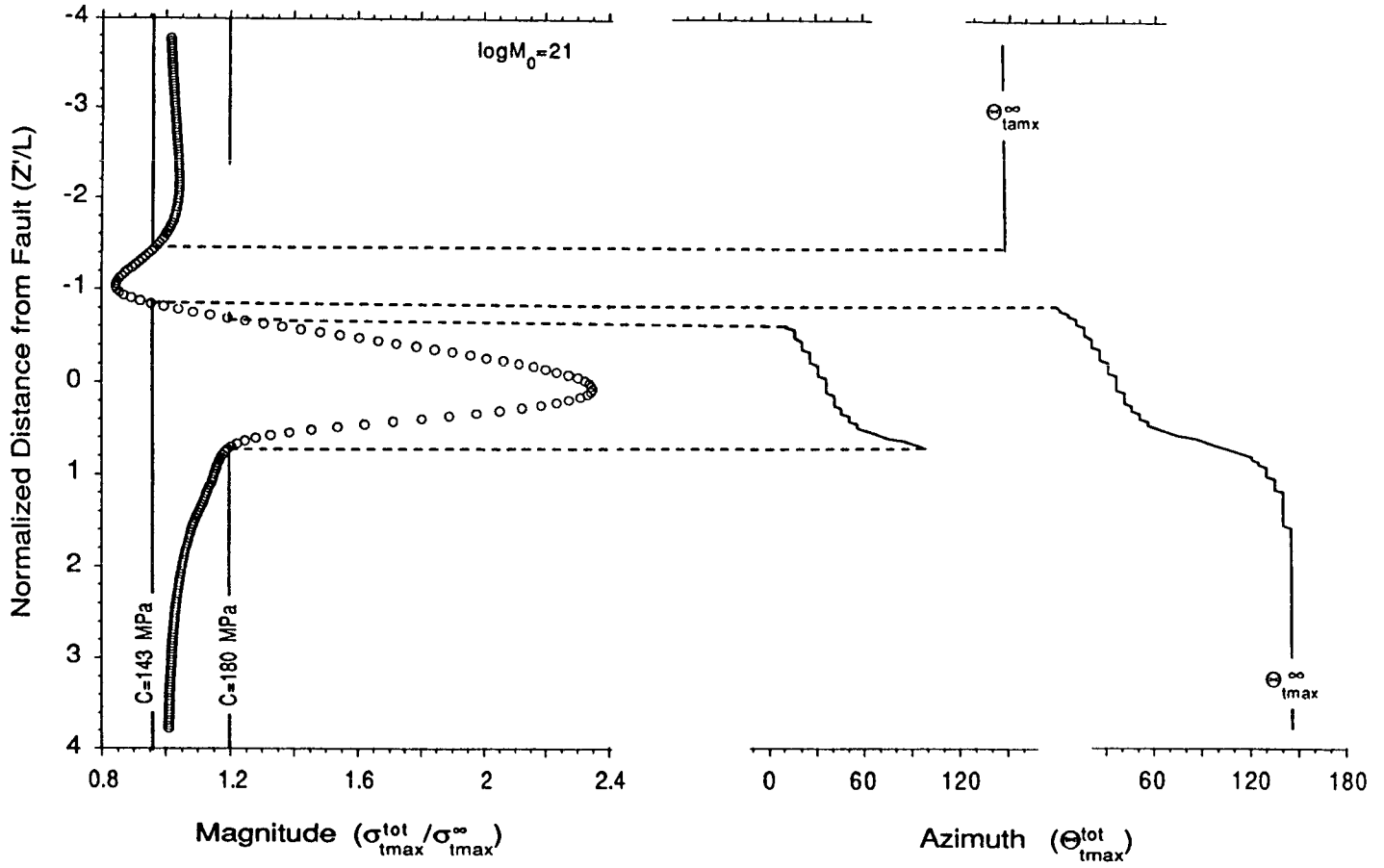

Figure 4.7 Same as Fig. 4.6 for a fault of $M_0=10^{21}$ dyne-cm and stress drop of 200MPa. This stress drop exceeds, by an order of magnitude, the shear stress available due to the ambient stres field alone.

4.2 The wavelength spectra of borehole stress fluctuations

Based on the conclusion that the majority of stress orientation variations are associated with active faults, the crustal volume bordering the San Andreas Fault may be conceptually visualized as containing a pervasive distribution of active fault patches of a wide range of scales which constitutes the broad SAF deformation zone. This zone of 'seismic flow' (quoting Kostrov, 1974) is sampled in the vertical dimension by the drillhole. Seismic fault displacements distributed in this rock volume may then make up a dynamically-stable system whose statistical properties are temporally invariant in the geological time scale. Such systems are termed critically self-organized (Bak et al., 1988) and are typically characterized by spatial self-similarity. It was shown in the previous section that the expression of fault-induced stress changes through borehole wall failure depends not only on the seismic moments of the penetrated slip patches but also on the ambient stress field and the fault geometry, all "re-processed" by the stress redistribution around the cylindrical hole. Nevertheless, the variance in wavelengths of stress orientation perturbations in the borehole may have useful implications for the statistical distribution of seismically active faults in the sampled depth interval, once better constraints can be put on the parameters involved. To obtain an estimate of this variance for the Cajon Pass breakout data, the power spectral density of the stress orientation function was calculated, as a function of frequency, for six intervals of the profile. The procedure involved the following steps:

1) Reducing the data to obtain no more than one data point per sampling interval (4cm), by averaging the two orientation data points from diametrically opposed breakouts at the same depth.

2) Angular 'smoothing', i.e. not restricting the azimuth data to a fixed angular range (e.g. 0° to 180° or 0° to 360°). The reason for this is the inherent non-uniqueness of azimuthal data, in the sense that each point can be shifted independently by ±180*n (where n is an integer), without changing its physical meaning. If variable orientation data are taken within a fixed angular range, wrapping around at the range boundaries results in artificial spectral noise. For example, a transition from azimuth 178° to 002° over a short depth interval is physically very smooth but will produce a sharp drop if the data are plotted in the range 0 to 180°.

3) Interpolation, to produce a continuous, equally-spaced spatial series (required for a spectral analysis employing the Fast Fourier Transform). A cubic spline interpolation scheme was used (Davis, 1986; Press et al., 1986), which considers the changes in slope (i.e. second derivatives) of the input function in the neighborhood of each point. The returned function is smooth over data gaps but loses its meaning if these are much wider than the sampling interval.

4) Estimation, by the periodogram method, of the power spectral density as a function of frequency, $G(\omega)$, employing the Fast Fourier Transform algorithm (Marple, 1987). The data is segmented into several, partially overlapping intervals and the spectrum of each is averaged. Three windows of 4096 points each and a 50% overlap were taken, providing only mild smoothing of the raw spectrum. The output consists of $G(\omega)$ over the frequency range 0 to $\frac{1}{2T}$, where T is the sampling interval (taken equal to the sample interval of the raw data, 4cm).

The analyzed data intervals range in length from 30 to 122 meters, and they were picked based on having typical stress orientation variations and lacking wide data gaps. Results are presented in Fig. 4.8 (and summarized in Table 2), where $G(\omega)$ vs. ω are shown between the highest detectable (Nyquist) frequency of 0.125 cm^{-1} down to the frequency corresponding to the length of the each interval. The linear fits (logarithmic least-squares curves with slope β) to portions of the spectrum define a power law relation

$$G(\omega) \approx \omega^{-\beta}, \tag{4.7}$$

for which the fractal dimension is given by (Turcotte, 1989)

$$D = \frac{5 - \beta}{2}, \tag{4.8}$$

and scale-invariance (self-similarity) is characterized by $1<\beta<3$ and $1<D<2$.

The first order observation to be made in Fig. 4.8 is that major bandwidths in all spectra are nearly linear and that for all of them $1<D<2$. This may suggest that there is a single dominant mechanism producing the stress perturbations of all scales represented in those linear spectra. If drilling-induced faulting would be important, one would expect an increased spectral power at some limited short wavelength band and breakdown of the self-similarity. The fall-off in spectral power with spatial frequency (as $\omega^{-(5-2D)}$) is a natural consequence of the fractal function (Mandelbrot, 1977). The spectra can further be broken down to shorter frequency bands with excellent linear fit, indicating that self-similarity in these cases is inhomogeneous, i.e. persists only over finite spatial bandwidths. This is common for natural phenomena and corresponds to "Effective fractal dimensions" (Mandelbrot, 1977). A third feature in some of the spectra is an

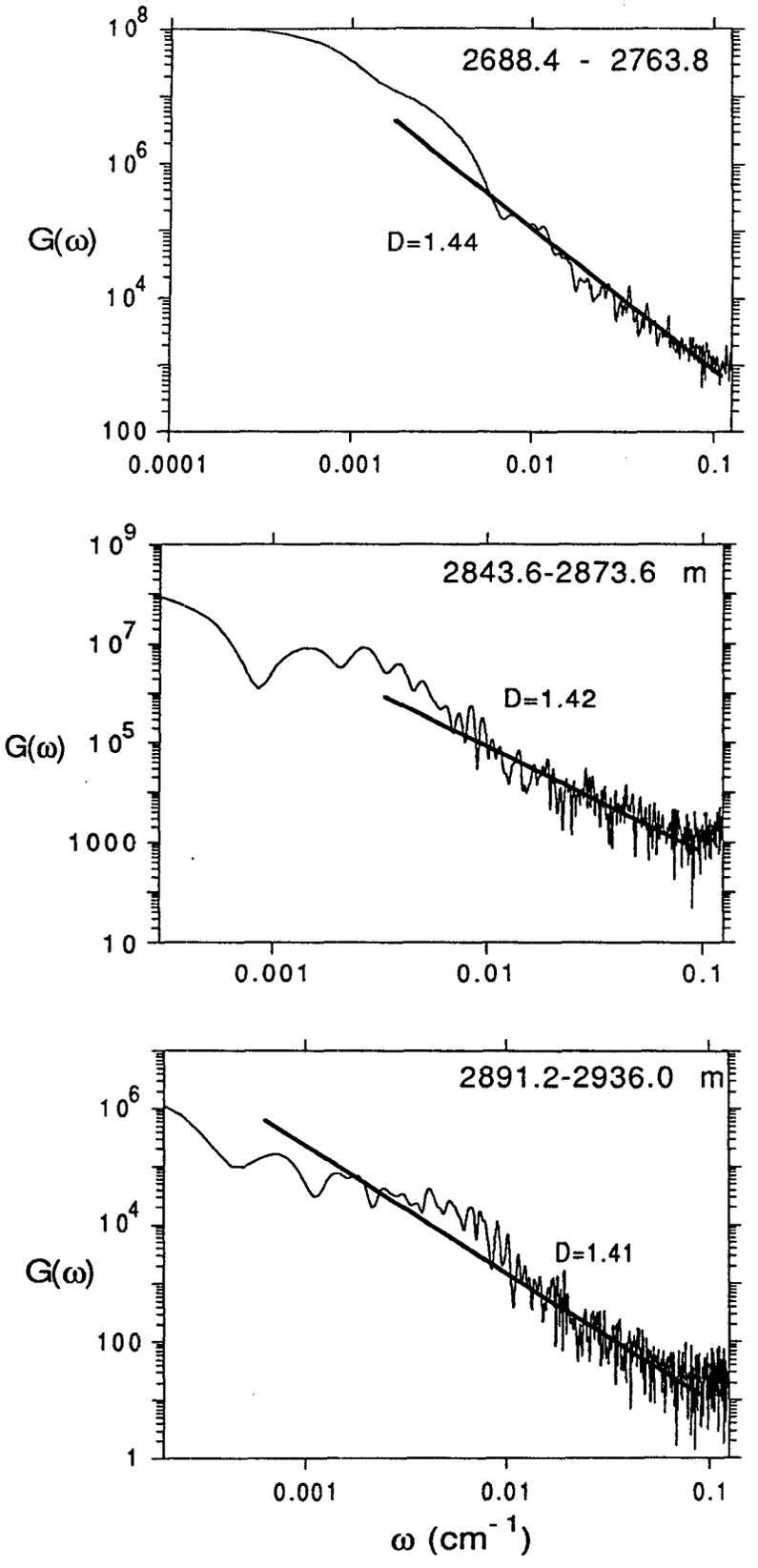

Figure 4.8 Power spectral density G(ω) as a function of frequency w of fluctuations in breakout orientations in six depth intervals in the Cajon Pass well. D - Fractal dimension.

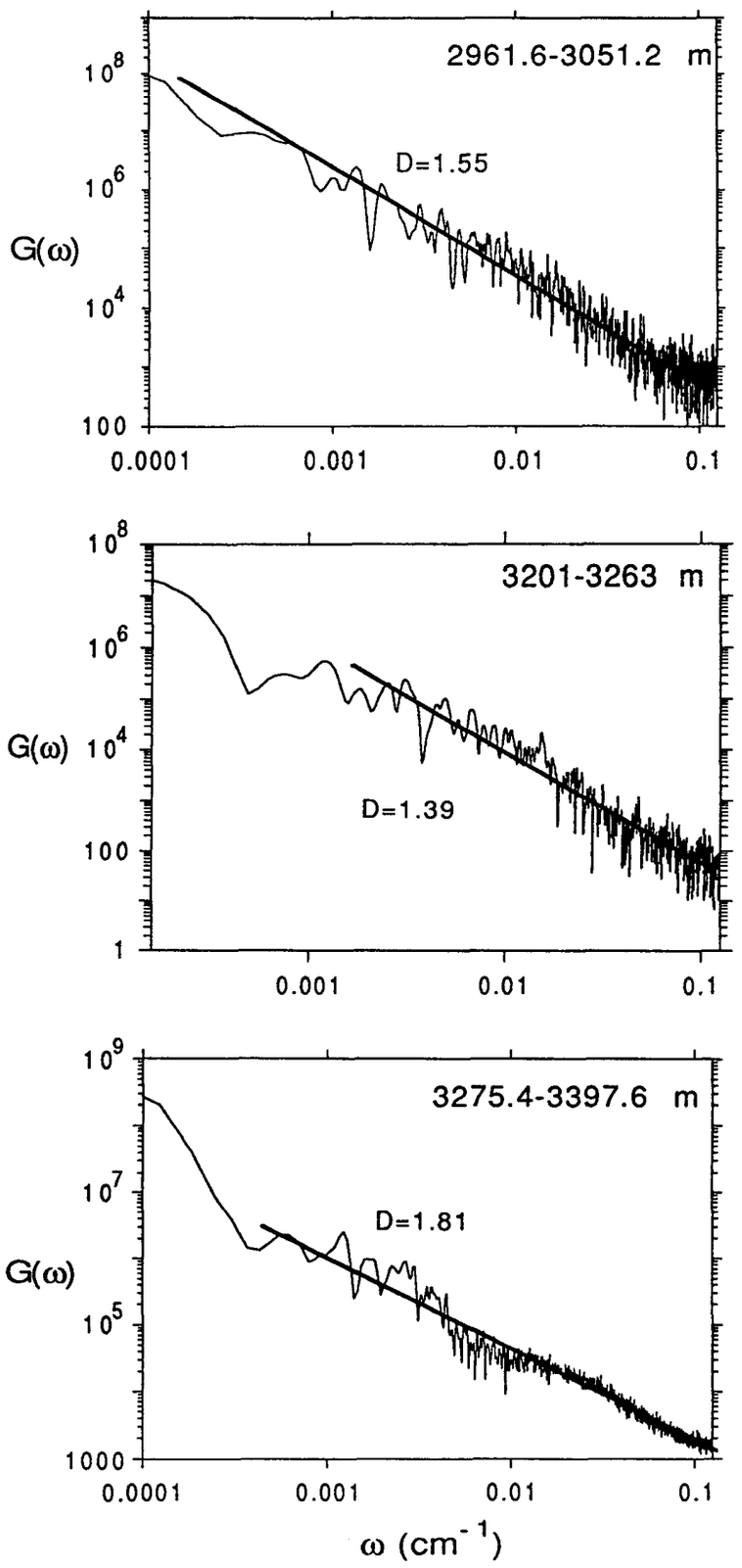
2961.6-3051.2 m
D=1.55
3201-3263 m
D=1.39
3275.4-3397.6 m
D=1.81
G(ω)
ω (cm⁻¹)

Table 2

Depth (m)	Interval length (m)	D	R
2688.4 - 2763.8	75.4	1.44	0.98
2843.6 - 2873.6	40.0	1.42	0.94
2891.2 - 2936.0	44.8	1.36	0.79
2961.6 - 3051.2	89.6	1.55	0.84
3201.0 - 3263.0	62.0	1.39	0.80
3275.4 - 3397.6	122.0	1.81	0.82

increase in spectral power (i.e. loss of self similarity altogether) at the very high frequencies, that is, for the spectral components of the shortest wavelength.

4.3 Discussion

It has been demonstrated in the past that the seismic process has a stochastic self-similarity in magnitude, time and space over length scales of 10^{-6} to 10^{5} meters, i.e. from microfracturing to large earthquakes (e.g. Mogi, 1962; Aki, 1967; Scholz, 1968; Kagan and Knopoff, 1981; Hirata, 1987). Then, the distribution of active faults and their associated stress fluctuations sampled by the Cajon Pass drillhole should, in principle, exhibit the same scale invariance. The spectra of stress fluctuation wavelengths along several depth intervals in the well show a self-similar distribution over wide bandwidths. The existence of this scale-invariance is somewhat surprising, considering the many parameters affecting the borehole stress state near active faults. It is assumed that self-similarity persists over longer length scales as well.

The mechanical analysis above showed that, for the fault geometry chosen, a distinction can be made between high and low moment/stress drop faults, based on the ratio between the fault-induced and the ambient tangential stresses at the borehole wall. For rock strength values on the order of the maximum ambient borehole tangential stress, low-M_0 faults are associated with discontinuous breakout occurrence and azimuthal variations from a few to several tens of degrees. Discontinuous breakout occurrence can, however, come about for other reasons as well (e.g. small local variations in strength). It is unlikely that drilling-induced fault slips make a significant, detectable contribution to the variability in breakout orientation.

High moment faults are associated with stress drops which are higher (by about an order of magnitude for the choice of parameters and geometry made here) than those calculated from commonly measured spectral parameters (<20 MPa; e.g. Hanks, 1977). Furthermore, using the ambient stress magnitudes measured in Cajon Pass (Zoback and Healy, 1991) and the laboratory-determined frictional strength of rocks (Byerlee, 1978), the available shear stress rate for strike slip faulting is ~90 bars/km and the maximum possible stress drop (excluding the possibility of slip overshoot) at a depth of 3km is ~270bars (27 MPa). If high-M_0 faults (i.e. with $\Delta\sigma$>20MPa) are indeed represented in the analyzed profile, they should be associated with significant increases of the borehole tangential stresses in their vicinity. Breakouts may then occur near those faults even where rock strength is too high to be overcome by the ambient stress field. Gradual azimuthal variations of the borehole stress concentration, up to complete 180° rotations, would then be possible, with wavelengths which generally increase with seismic moment. The actual extent of spiraling breakouts would depend also on the rock strength and the specific location and angle of piercing through the fault.

If the large stress drops predicted for high-M_0 faults are unrealistic, all the stress fluctuations observed in the Cajon Pass well are due to stress *drops*, and none to stress *increases*. Another, quite unlikely, possibility is that the magnitudes of the ambient stresses used in the calculations are in error and the transition from high- to low-M_0 pattern occurs at lower absolute stress magnitudes. The ambient stress field has been determined based on the hydraulic fracturing tests in the Cajon Pass well (Zoback and Healy, 1991), which provided an accurate estimate of the minimum principal stress (32.9±0.2 MPa at 2661m depth). The vertical, lithostatic stress, would only vary insignificantly for small changes in density and pore pressure. The calculated maximum principal stress

is less certain (70.0±7.6 MPa), but not expected to be lower than the vertical stress. Lowering the horizontal principal stresses, even below reasonable bounds, does not lower the transition from high- to low-M_0 sufficiently for the smooth, high amplitude azimuth changes to occur within the "allowed" range of stress drops.

Finally, it may be hypothesized that extremely high stress drops occur locally, due to high accumulated shear stresses beyond that available by the mean ambient far field stress field. In the simple mechanical model used above, the effects of fault-ends and fault interactions were ignored. Numerous observational, seismological and theoretical studies (e.g. Wyss and Brune, 1967; Hanks, 1974; Wu and Kanamori, 1975; Spottiswoode and McGarr, 1975; Das and Aki, 1977; Kanamori and Stewart, 1978; Nur, 1978; Madariaga, 1979; McGarr et al., 1979; Nur and Israel, 1980; Segall and Pollard, 1980; Rudnicki and Kanamori, 1981; Reasenberg and Ellsworth, 1982; Pechman and Kanamori, 1982, among others) have demonstrated that earthquakes are in general complex, multiple events on segmented and inhomogeneous faults. Small faults, with relatively short accumulated displacement, are likely to be especially irregular (as field observations indeed show) and affected by both non-uniform stress drops and spatially non-uniform frictional properties (Nur, 1978).

The case of heterogeneous stress drop is often modelled by distinct 'asperities', irregularly distributed on fault planes, which break after previously being loaded by the stress release in the surrounding slipped zones (e.g. Madariaga, 1979; Rudnicki and Kanamori, 1981). Madariaga (1979) showed theoretically that for given seismic moment and fault size, the calculated stress drop (for simple, smooth isolated faults) underestimates the true stress drop on the broken

patches of the fault by a factor equal to the ratio of the typical patch radius to the total fault radius. Particularly on the small scale, stress drops on unbroken 'barriers' may be variable and negative (stress increases). Rudnicki and Kanamori (1981) used solutions for colinear shear cracks to study their compound effect on the static seismic moment, stress drop and energy release due to faulting of the asperity between the cracks. For the case of strong barriers between slipping fault patches, with widths which are ~20% of the fault patch width, the apparent (calculated) stress drop underestimates the true stress drop by a factor which is on the order of the number of colinear cracks. The amplified seismic moment is primarily due to the additional displacement induced by the failing asperity on the adjacent (previously slipped) zones. Large local stress drops can result, while the average stress drop of the whole fault zone is comparable to that of an isolated fault of the same average moment and size. A well known example s the San Fernando earthquake of 1971 (Hanks, 1974), where a stress drop of 350-1400 bars was estimated for the source area.

With respect to the effect of fault interaction on the true (static) source parameters, Rudnicki et al. (1984) use the same crack solutions to calculate the amplification of the stress drop and seismic moment associated with a small slip patch close to, and colinear with a previously slipped larger fault zone. As an example of Rudnicki et al.'s calculations, if the ratio of dimensions of the new slip patch to that of the preexisting slip zone is $\frac{L_2}{L_1} = 5 \cdot 10^{-3}$ and the width of the intervening zone is $L_b=0.001L_1$, the seismic moment due to failure of this asperity is 10 times that of an isolated fault of the size of the preexisting slip zone. Actual values may be, for example, L_1=800m, L_2=4m and L_b=0.8m. Although in this example L_2 and L_b are very small (and cannot be modelled by the model above), they are still significant for a borehole of R=8.25cm, with a

'near-field' which extends to a distance of no more than 0.41m (5R) from the center of the hole. Thus, a small slip patch crossed by the borehole can easily produce an apparently unrealistic seismic moment if its failure was induced by slip on neighboring, larger fault patches. The amplification can be ten fold the moment produced by the nearby fault, if isolated.

The abundant interactions between active faults penetrated by the Cajon Pass drillhole may make the resolution of the high-stress-drop problem unresolvable until a more complete numerical model is constructed. It is possible that the drillhole directly samples locally amplified stress drops and, as the time between faulting and drilling is probably sufficient for inelastic stress relaxation, some of the observed stress changes may have been even higher at the time of faulting. If, however, the conservative upper limit of 20MPa is adopted for stress drops (in general and in particular in the Cajon Pass), then the low-M_0 patterns alone (for seismic moments up to about 10^{20} dyne-cm) should be able to explain the observed faulting-induced stress perturbations.

5. THE SEISMIC CYCLE OF THE SAN ANDREAS FAULT NEAR CAJON PASS

5.1 Introduction

In this section the basic assumption will be made that the average orientation of borehole breakouts in the Cajon Pass drillhole, resulting in an apparent mean horizontal maximum compressive stress $\overline{S_H^*}$, reflects the state of stress in a large (km-scale) rock volume adjacent to the San Andreas Fault, so that $\overline{S_H^*} = \overline{S_H}$, the mean remote maximum horizontal compressive stress. This working hypothesis is apparently supported by the relatively stable overall mean azimuth of S_H^*(057°, s.d. 19°, n=32616; Fig. 3.7) and the extent (1710m) and depth (3.46km) of the analyzed depth interval. If this hypothesis is valid, it means that the average Cajon Pass stress state is associated with the cycle of large San Andreas Fault earthquakes in this region. With this assumption, the actual average S_H^* orientation, which results in left lateral (LL) shear stress on planes striking parallel to the San Andreas Fault (i.e. ~300°), is unexpected and means that left-lateral shear stress may prevail on the SAF near Cajon Pass, at least during some periods during the earthquake cycle. The hydraulic fracturing stress measurements in Cajon Pass (Zoback and Healy, 1991) showed that the left-lateral shear stress magnitude is on the order of 3.5±3MPa at about 2.5km depth. These results are inconsistent with the long term slip history of the SAF, although qualitatively consistent with the LL Quarternary displacement of up to 4km along the Cleghorn Fault, which strikes 095° southeast of Cajon Pass and may have an unexposed extension parallel to the San Andreas Fault near the drillsite (Weldon, 1986).

To study the effect of the cycle of stress accumulation and release along this section of the San Andreas Fault, the net change in fault-parallel shear stress since immediately prior to the earthquake of 1812 is estimated. Although several large SAF earthquakes may have ruptured through Cajon Pass earlier in this millennium (Sieh, 1978; Sieh and Jahns, 1984; Weldon and Sieh, 1985; Sieh et al., 1989), there is no direct information about their associated displacements in this area. The analysis is particularly significant in this region since, in the absence of measurable surface fault creep on the San Andreas Fault (Louie et al., 1985) and the San Jacinto Fault (Keller et al., 1978; Allen, 1981), interseismic stress relaxation may be negligible and the stresses measured at relatively shallow depths may directly reflect the cycle of stress accumulation and release in large earthquakes. While details of the 1812 rupture are still loosely constrained (Jacoby et al., 1988; Sieh et al., 1989), the major results of this analysis are insensitive to small variations in the amount of slip during this event or its exact timing.

Geological maps of the Cajon Pass area (Rodgers, 1967 [1:25000]; Weldon, 1986, plate 3 [1:11900]) show several strike changes along the SAF (Fig. 5.1). Although such local variations may not persist in time or extend in depth through the entire upper crust (and other geometric complexities may exist at depth), their potential effect on the distribution of slip-induced stresses are examined as well.

In order to estimate the stresses induced by both seismic displacements and aseismic slip at depth, the SAF and SJF are modelled (Fig. 5.2) as combinations of rectangular dislocation (displacement discontinuity) surfaces embeded in an otherwise continuous, isotropic, linear elastic half-space. The boundary conditions are thus the relative displacements across fault planes,

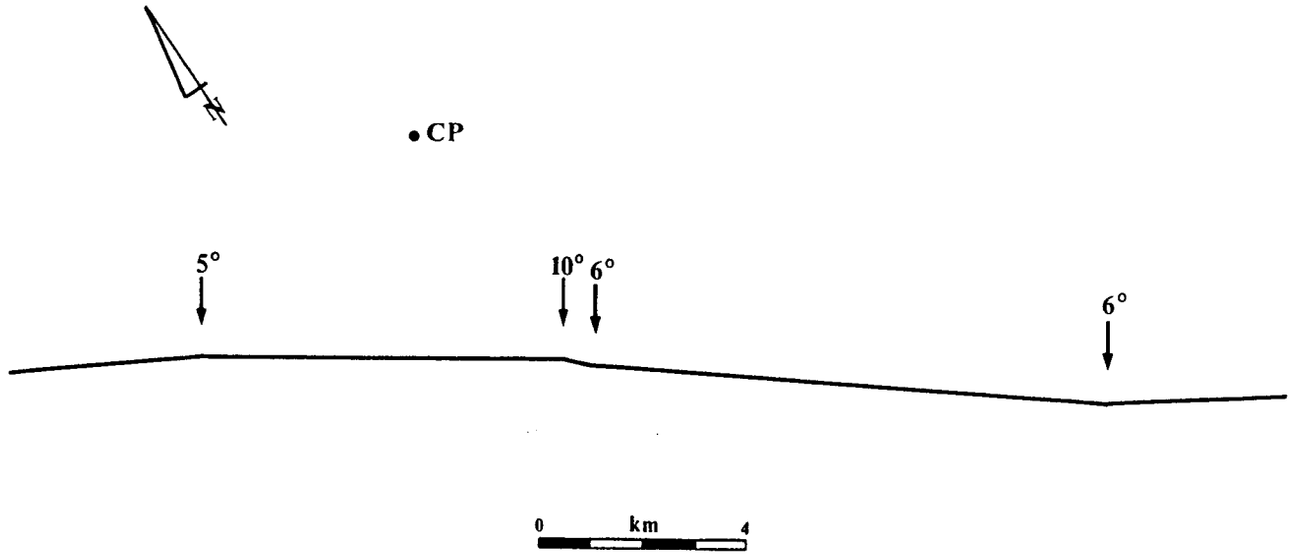

Figure 5.1 Major strike changes (in degrees) along the San Andreas Fault near Cajon Pass.

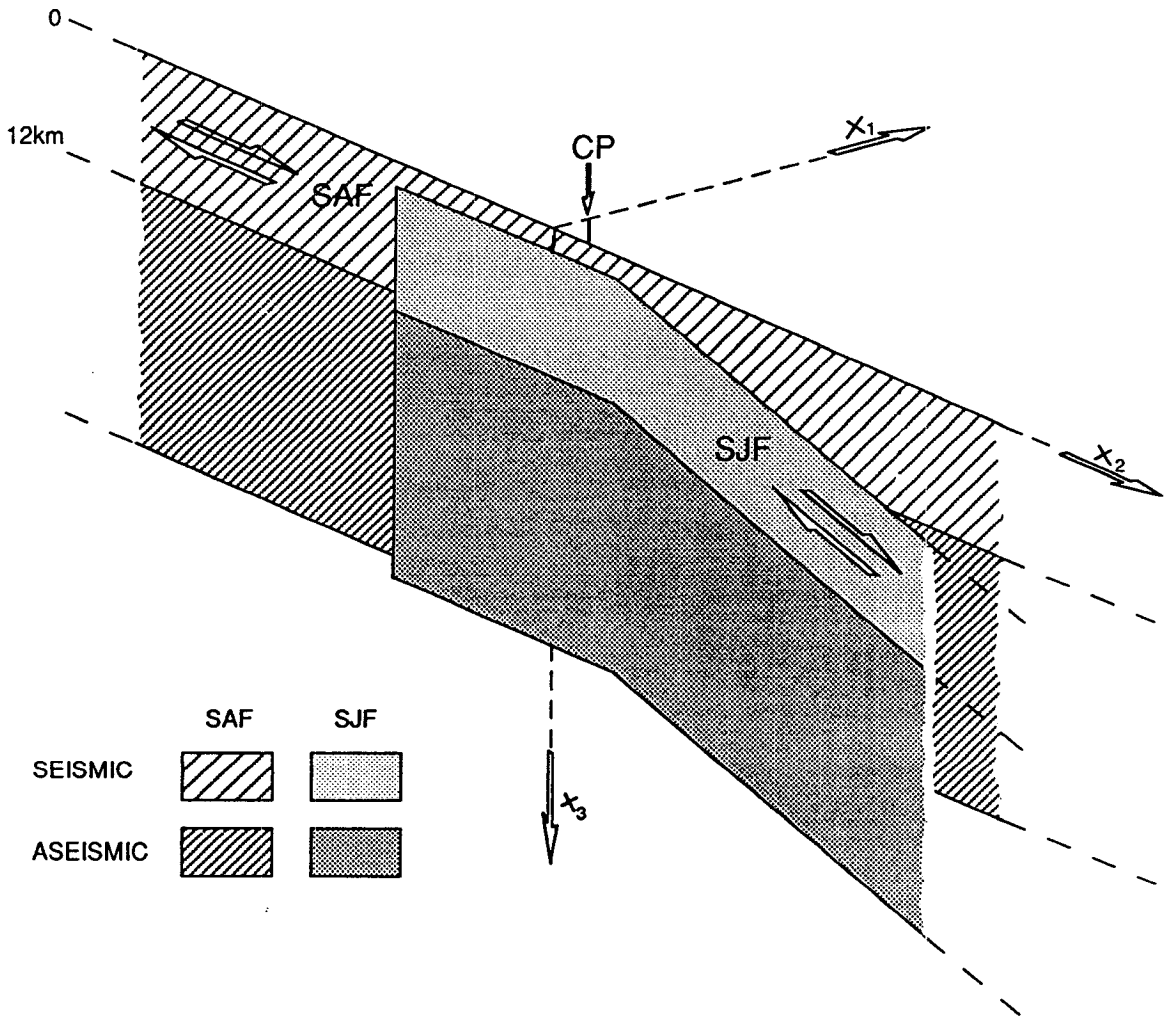

Figure 5.2 Dislocation fault model of the San Andreas and the San Jacinto Faults in the Cajon Pass area.

while the calculated, slip-induced stresses represent average stress changes due to faulting. A simple lithosphere model is assumed, in which the zone of coseismic slip is locked between large earthquakes up to the surface and a lower elastic zone of steady interseismic slip extends below (Savage and Burford, 1973). The long term interseismic motion below the seismogenic zone is imposed as uniform slip at constant rate, which is consistent with slip rates determined from surface offsets and from shear strain rates derived from geodetic measurements. The data concerning displacements across the SAF and SJF are summarized in Table 3.

Considering the effect of transient postseismic slip (Thatcher, 1983) and the range of depths which the locked zone may assume over the earthquake cycle due to the upward penetration of the aseismically slipping zone (discussed by Li and Rice, 1987), it can be assumed that the effective depth of the locked strip has by now, 178 years after the last large earthquake, been reduced relative to its 1812 value. The transitional depth interval is therefore included in the aseismic zone and the bottom of the coseismic strip is placed at a depth of 12 km. Furthermore, varying the depth of the coseismic zone in the range 10-15km has only a minor effect on the stress induced in the depths of interest (0-5 km). This simple scheme is similar to "thick lithosphere" models (e.g. Thatcher [1990], Fig. 10), in which an elastic plate is underlain by a viscoelastic half-space (asthenosphere) and deformation is imposed across the aseismic fault in the elastic plate (e.g. Savage and Prescott, 1978). In such a model the strain field at shallow depths is completely controlled by the aseismic dislocation and the asthenospheric time-dependent effects are unfelt at shallow depths if the seismogenic depth is much smaller than the lithosphere thickness. In more sophisticated models (e.g. Li and Rice, 1987) the deep aseismic slip is taken as

Table 3

Fault	Data	Type of observation	Reference
SAF @ Wallace Creek	Long term: 33.9±2.9 mm/yr	surface offsets	Sieh & Jahns, 1984
SAF @ Cajon Creek	Long term: 24.5±3.5 mm/yr,		Weldon & Sieh, 1985
	last 14400 yrs	"	
SAF	No measurable surface creep	creepmeters	Louie et al., 1985
	along the 1812 rupture		
SAF	1812: ~170km rupture;	trees	Jacoby et al., 1988
	S end ~35km SE of CP;		
	~6m @ PC, ~4m @ CP	surface offsets	Weldon & Sieh, 1985
SAF	1857: No surface slip @ CP;		Agnew & Sieh, 1978
	S end within 20 km N of CP.	"	Weldon & Sieh, 1985
SAF @ Pallet Creek	Intracluster intervals: ~100 yr		
	Intercluster intervals: 200-300 yr	C^{14} dating	Sieh et al., 1989
SAF @ Cajon Pass	Aseismic slip 1973-1984:		
	24.5±2.4 mm/yr for D=13km		

Table 3 (cont.)

	Max. horiz. shortening: 344°±2°	trilateration	Savage et al., 1986
SJF @ Anza	Long term slip:	surface offsets	Sharp, 1981
	8-12 mm/yr, last 0.73 m.y.		
	1.4-2 mm/yr, 400-6000 yrbp		
	2.8-5 mm/yr, last 400 yrs		
SAF @ Palmdale	Long term slip 1971-1984:		
	0.2±0.01 mstrain/yr	trilateration	Savage and Gu, 1985
SJF	Seismic slip since 1890: 8 mm/yr	seismic moments	Thatcher et al., 1975
SJF	Long term slip 1969-1975 and		
	1973-1981:	Savage & Prescott, 1976	
	11-18 mm/yr, for D=10-15	trilateration	King & Savage, 1983
SJF - Claremont	Seismic slip 1890-1923: 135 cm		Thatcher et al., 1975
	No surface creep 1973-1981		Keller et al., 1978
SJF: CP-Riverside	Seismicity mostly W of SAF	surface displacements	Sharp, 1972
	~20cm in 1899, 1907	inferred seismic slip	Thatcher et al., 1975

a viscoelastic response to mantle flow induced by slip at shallower depths and not as an imposed boundary condition.

The concept of dislocation surfaces originated with the work of Voltera (1907). Steketee (1958) showed that these surfaces can be described as distributions of 'nuclei of strain' and related the displacement discontinuity over an arbitrary surface in an infinite elastic medium to the resulting displacements at any arbitrary point, using a set of Green's functions. The basic model considers uniform Burgers vectors across dislocation patches (Voltera dislocations); A useful way of simulating non-uniform displacement distributions (Somiglana dislocations) is then to discretize fault planes into elements of constant slip, which are observed from distances much larger then the dimension of the elements. Concurrent effects of several faults are taken as the linear superposition of their respective elastic fields. The buried dislocation plane model for long term interseismic slip is obviously an oversimplification, but offers a first order estimate of the effects of such motion and has been successfully used to model crustal strain accumulation (e.g. Savage and Hastie, 1966; Savage and Burford, 1973).

The analysis outlined uses a computation of the three-dimensional elastic fields associated with dislocation surfaces in a half-space based upon the principles described above (program DIS3D; Dunbar, 1984; Erickson, 1986). A shear modulus of 30GPa and Poisson's ratio of 0.25 are used for the entire crust in the calculations.

5.2 Shear Stress Accumulation Since 1812

The 1812 SAF earthquake. Surface offsets related to a large earthquake preceding the 1857 earthquake were first observed by Sieh (1978, 1984) at Pallet Creek, about 44km northwest of Cajon Pass. At Cajon Creek, Weldon and Sieh (1985) concluded that the latest displacement across the SAF was of about 4 meters and possibly associated with an earthquake in the early 19th century. Based on a dendrochronologic study, Jacoby et al. (1988) correlated a large pre-1857 event with the earthquake of December 1812. It ruptured along about 170km, with a southern termination several tens of km southeast of Cajon Pass (Fig. 1.1).

The change in shear stress parallel to the SAF is calculated for an induced uniform RL slip of 4m (after Weldon and Sieh [1985]), typical of large San Andreas earthquakes, along a fault which is very long relative to both its depth and the distance to the CP drillsite. At the location of the drillhole, and at a depth of 3km, the change of shear stress is on the order of 3MPa, LL (negative), on planes parallel to the fault (Fig. 5.3). The effect of introducing strike changes along the fault is to slightly enhance the 1812 shear stress drop at CP by about 0.2 MPa.

As the RL slip in the pre-1857 (probably 1812) event at Pallet Creek is estimated to be of 6m (Jacoby et al, 1988), the effect of a smooth slip gradient, from about 6m at Pallet Creek to 4m at CP and vanishing 35km southeast of CP was also modelled. At Cajon Pass, the results are indistinguishable from those of uniform slip.

The 1857 SAF earthquake. The slip distribution for this event is among the best documented for major historic strike-slip earthquake (Sieh, 1978, 1984; Sieh

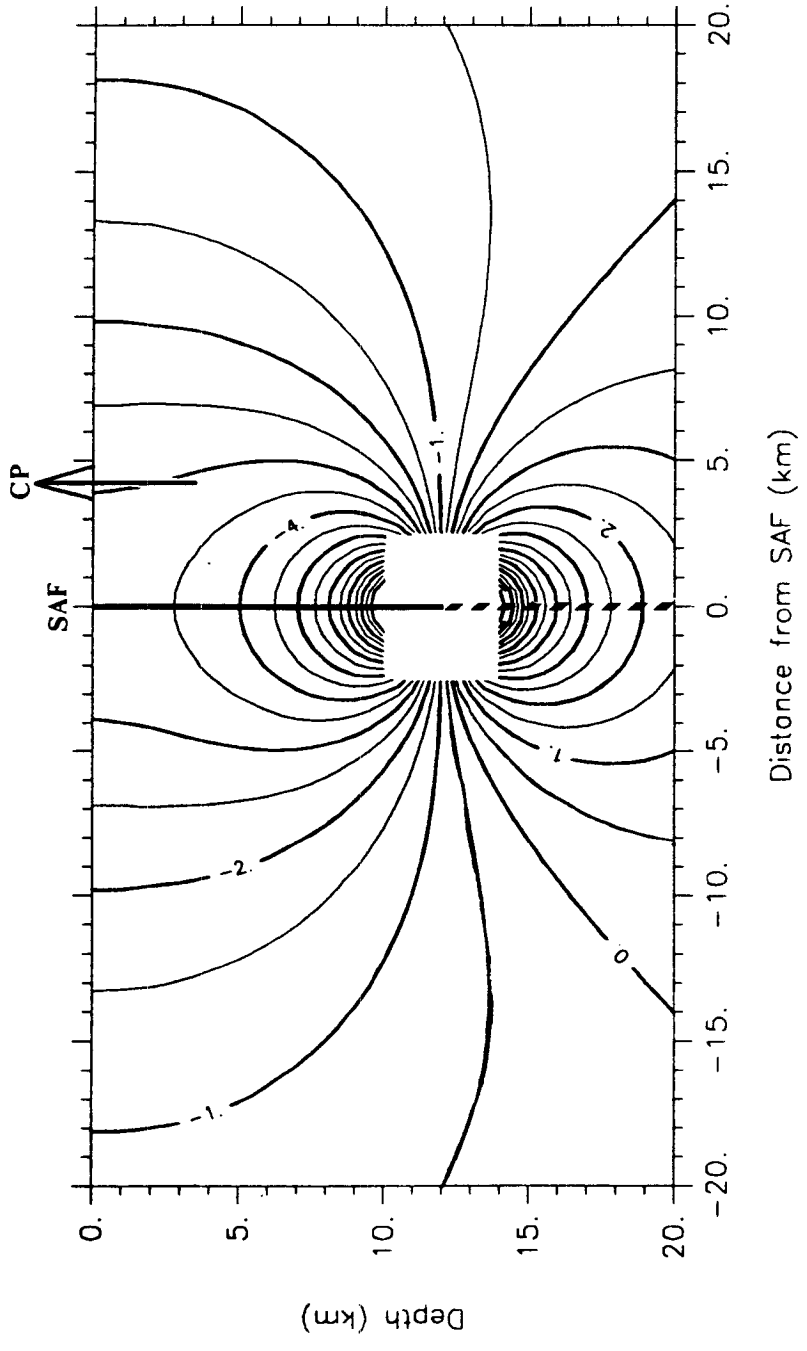

Figure 5.3 The net change in shear stress (MPa) parallel to the SAF near Cajon Pass, in a vertical x_1-x_3 cross section perpendicular to the SAF at CP (see Fig. 5.1) , due to 4m right-lateral slip during the 1812 earthquake.

deposits at Pallet Creek, with coseismic slip of about 6m and decreasing southeastward. The rupture ended somewhere within the 20km northwest of Cajon Creek (Weldon and Sieh, 1985). Rather than assuming an abrupt termination of the rupture, a smooth slip gradient is assumed, which tapers from 6 m at Pallet Creek to zero 10 km northwest of CP (Fig. 5.4a). The associated change in shear stress is such that a small amount of RL shear parallel to the SAF (~1.1MPa) is induced ahead of the rupture zone (Fig. 5.4b). At the CP site (Fig. 5.4c), the model predicts that the effect of the 1857 rupture was to induce a very small amount (<0.35 MPa) of RL shear. Small changes of the slip gradient of Fig. 5.4a have only minor effects on these results. Thus, the 1857 rupture, in spite of its magnitude and proximity to Cajon Pass, had a very small effect on the shear stress distribution in this area.

Long term stress accumulation due to deep aseismic slip. As mentioned above, the strain accumulation in the period 1973-1984 was deduced by Savage et al. (1986) from repeated trilateration surveys of several geodetic networks along the SAF. The results for the Cajon network should be taken with caution because of the small aperture of the net (~16km) and the small number of lines (ibid, p. 7460). The shear strain rate measured for this period, 0.28±0.04 μrad/yr, results in slip rates of 21.1±3.0 mm/yr and 26.4±3.7 mm/yr for a seismogenic zone 12 and 15 km deep, respectively (using a buried screw dislocation model; Weertman and Weertman, 1964, and Savage and Burford, 1973). This is remarkably similar to the Holocene slip rate of 24.5±3.5 mm/yr determined from offset Quarternary deposits by Weldon and Sieh (1985). To the northwest, in the Carrizo plain, Sieh and Jahns (1984) determined a Holocene slip rate of 35.8±5.4 mm/yr. In the Palmdale area, the strain rate for the period 1971-1984, based on trilateration surveys (Savage and Gu, 1985) was

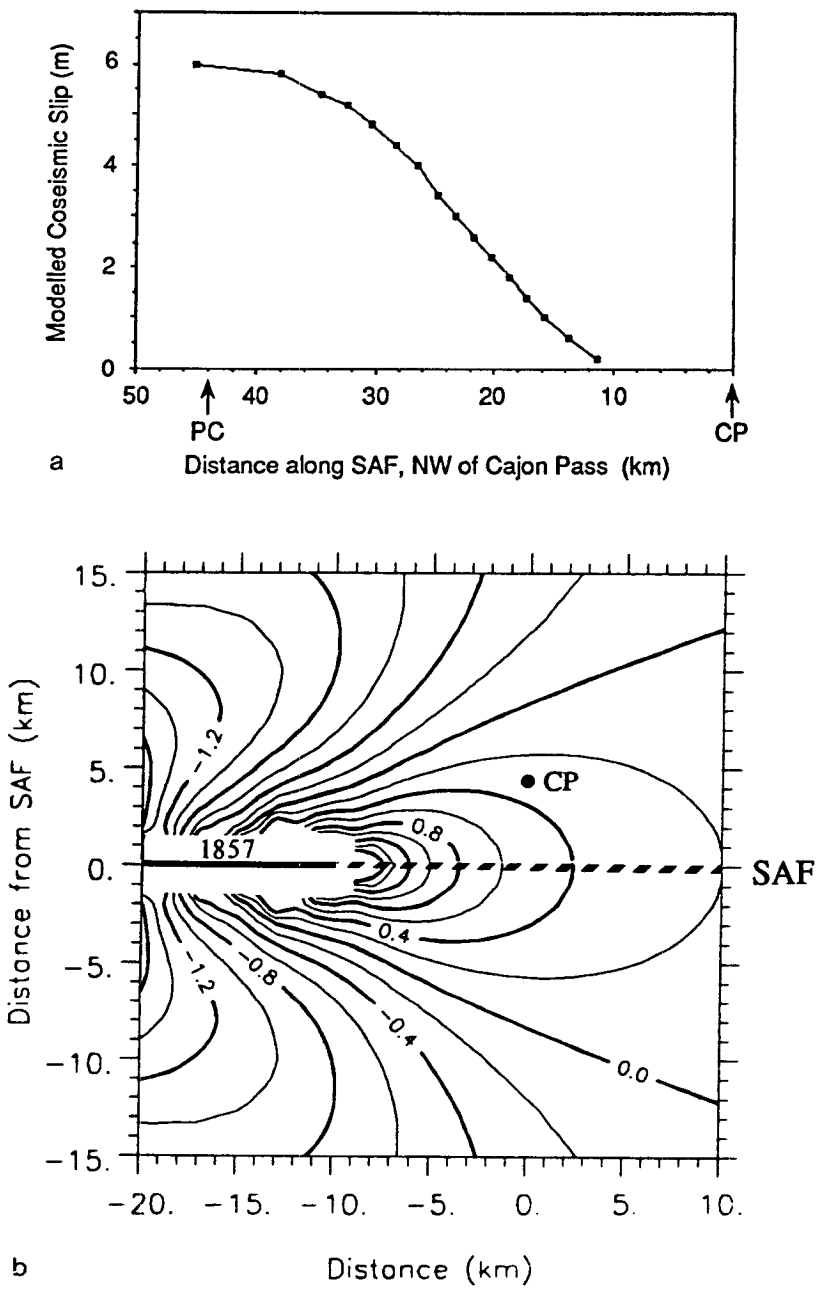

Figure 5.4 The change in shear stress (MPa) parallel to the SAF near Cajon Pass due to the 1857 San Andreas earthquake. (a) Slip gradient used for the southeastern termination of the 1857 rupture, from 6m at Pallet Creek (PC) to zero 10km northwest of Cajon Pass (CP); (b) Distribution of shear stress change at a depth of 3km around the southeastern tip of the 1857 rupture; (c) Shear stress induced by the 1857 event, in a vertical x_1-x_3 (Fig. 5.1) cross section perpendicular to the SAF at CP. Positive contour values represent right-lateral shear stress parallel to the SAF.

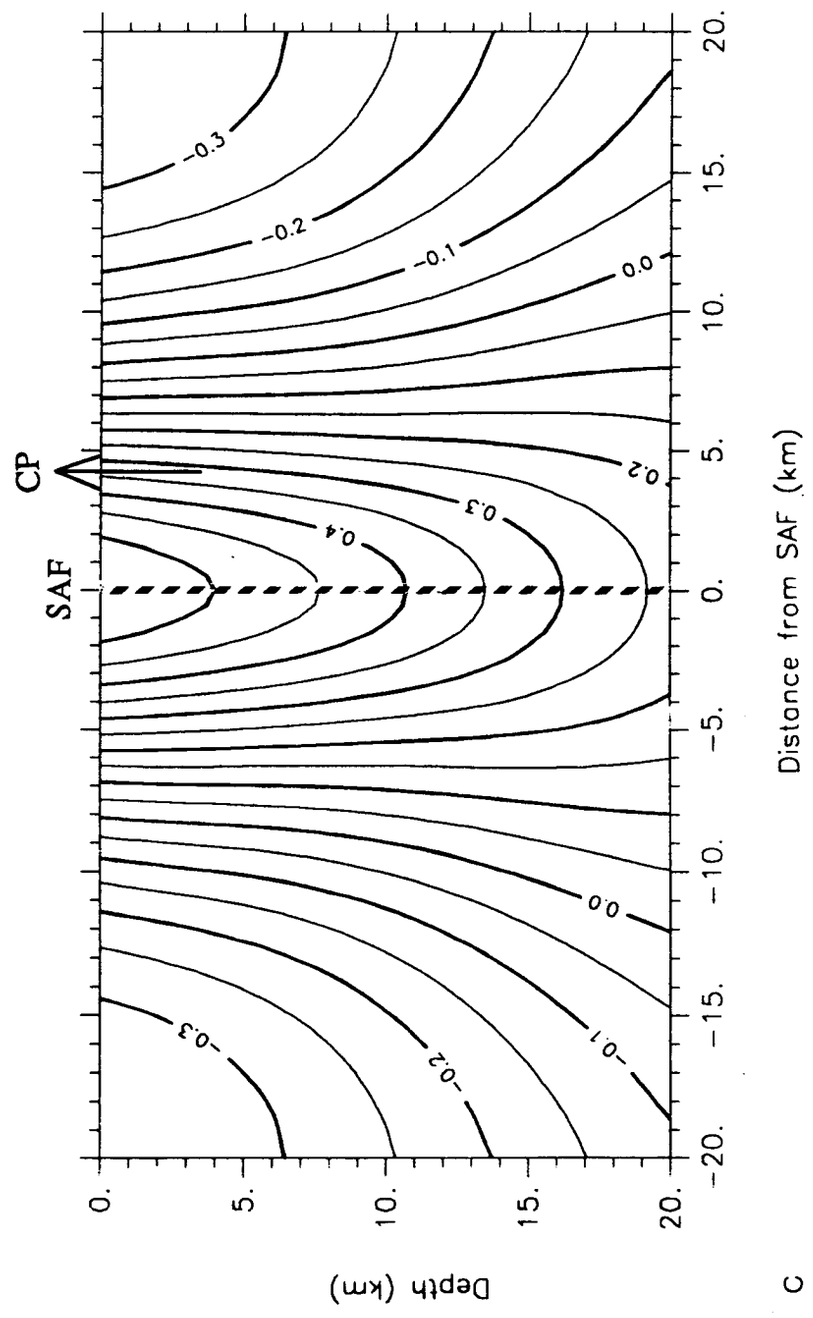
CP
SAF
-0.3
-0.2
-0.1
0.0
0.2
0.3
0.4
0.0
-0.1
-0.2
-0.3
0.
5.
10.
15.
20.
20.
15.
10.
5.
0.
-5.
-10.
-15.
-20.
Depth (km)
Distance from SAF (km)

C

0.2±0.01 μstrain/yr, which results in slip rates of 30.2±1.5 mm/yr and 37.7±1.8 mm/yr for a seismogenic zone 12 and 15 km deep, respectively. A reasonable long term slip for the northern section of the SJF is 10mm/yr (see below), so that the total slip rate across the SAF/SJF system is 31-36mm/yr. Thus, the aseismic slip rate to the north and to the south of CP are about equal.

Fixing the transition in slip rate 10km northwest of Cajon Pass and using 24 mm/yr and 35 mm/yr (to the south and to the north of the transition, respectively) as representative values for the last 178 yrs, the net driving shear stress induced by long term slip since 1812 at Cajon Pass is about 2 MPa RL. Again, the exact details of the slip rate transition have almost no effect on the result at the depth of interest at CP.

Considering the effect of strike changes along the SAF, they reduce, by about 0.5MPa, the RL shear stress induced by both the 1857 earthquake and the deep aseismic slip at CP.

San Jacinto Fault. The long term geologic slip rate along the SJF was deduced by Sharp (1981) to be 8-12mm/yr for the last 0.73 m.y., based on offset of Holocene deposits. Trilateration surveys in the periods 1969-1975 and 1973-1981 (Savage and Prescott, 1976; King et al., 1983) result in a lower crustal slip rates of 11-18 mm/yr for seismic/aseismic transition depths of 10-15km, respectively. We use a representative value of 10 mm/yr for the lower crustal aseismic slip on the SJF.

The cumulative coseismic slip along the northern segment of the SJF (Claremont Fault) from 1890 to 1923 was estimated by Thatcher et al. (1975) to be about 1.35m. Along the diffuse extension of the SJF which parallels the SAF near CP (CP-Riverside shear zone), the same authors estimated about 0.2m of RL slip during each of the events in 1899, 1907 and 1970. However, there is no

data about earthquakes between 1812 and 1890 and the cumulative amount of coseismic slip since 1812 is believed to be higher. For this analysis, displacements of 0.6m and 1.35m were used for the CP-Riverside shear zone and the Claremont fault, respectively.

The overall effect of these SJF displacements on the shear stress distribution near CP is on the order of 0.1-0.2MPa, RL on planes parallel to the SAF. This means that the RL loading of the seismogenic zone due to deep aseismic slip on the SJF slightly exceeds the coseismic stress release. However, additional coseismic slip (which presumably occurred in the 19th century) on the SJF would have probably brought the net shear stress induced by the SJF at CP to nearly zero.

Cumulative Effects Since 1812. Figure 5.5 shows the cumulative result of the coseismic and aseismic displacements described above, in a vertical cross section perpendicular to the SAF at Cajon Pass. The strike changes shown in Fig. 5.2 were incorporated in the model and result in the asymmetry of the stress distribution about the trace of the SAF, with a somewhat higher horizontal gradient on its northeastern side and with no vertical gradient through most of the coseismically rupturing zone. As the effect of slip on the SJF is extremely small (i.e. <0.1MPa), it has been neglected. The net change, since 1812, in shear stress parallel to the SAF is about -1.1MPa at a depth of 3 km at CP. The nearby fault bends have the general effect of somewhat reducing the rate of RL shear stress accumulation and slightly increasing the magnitude of the 1812 stress change. The overall result of these calculations is that the dominant contribution to the SAF-parallel shear stress budget at CP since the beginning of the current earthquake cycle comes from the stress drop associated with the 1812 earthquake and that the net change in shear stress parallel to the SAF in

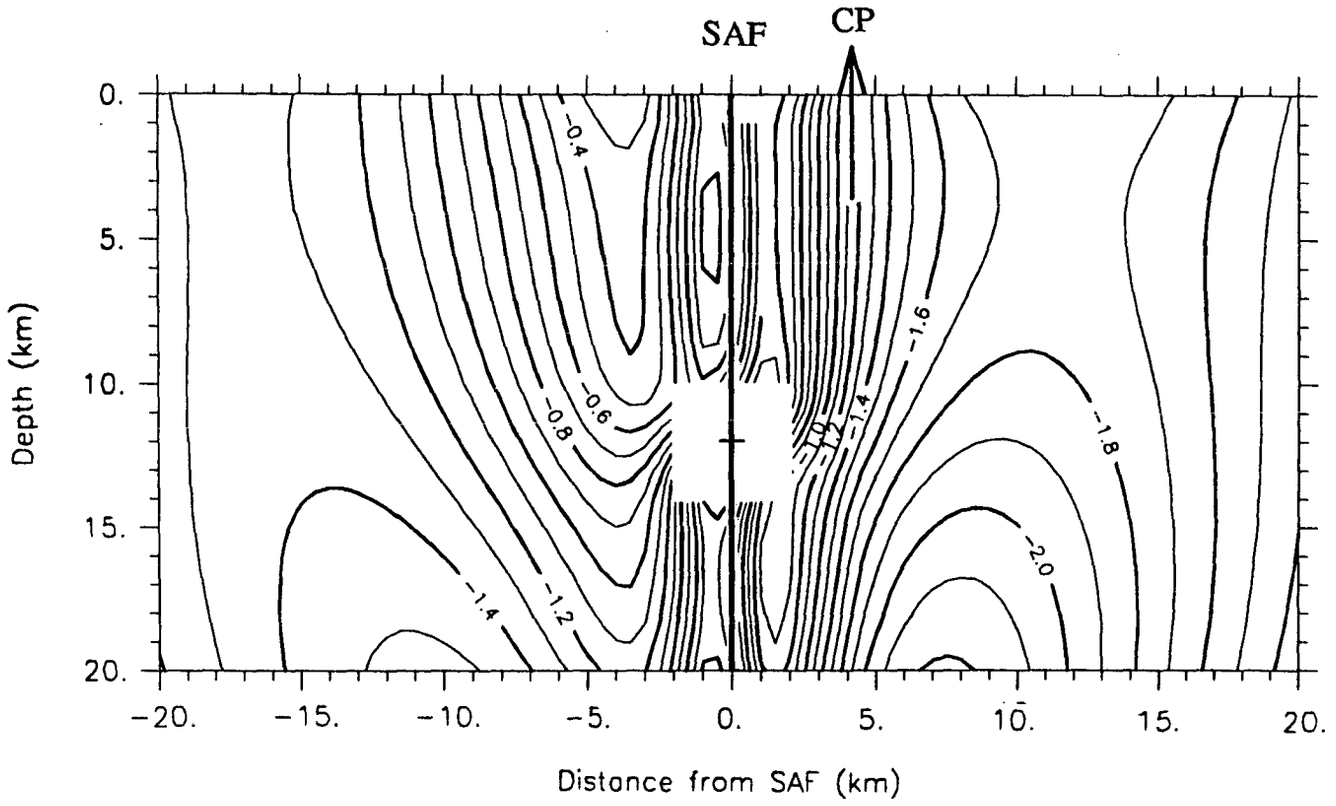

Figure 5.5 The net change in shear stress (MPa) parallel to the SAF near Cajon Pass, in a vertical x_1-x_3 (Fig. 5.1) cross section perpendicular to the SAF at CP, due to coseismic and aseismic displacements along the fault since prior to the 1812 earthquake, incorporating the strike changes observed at the surface near CP (Fig. 5.2). Positive contour values represent right-lateral shear stress parallel to the SAF.

the period since immediately before the 1812 earthquake is on the order of 1.0 MPa, left lateral. In other words, while right-lateral shear stress on planes parallel to the San Andreas Fault has not been totally recovered at this site, overall the state of stress at Cajon Pass is quite similar to that just prior to the 1812 earthquake.

5.3 Effects of aseismic slip Near Cajon Pass

Wesson (1988) utilized the fault model of Tse et al. (1985) to analyze possible variations of stress orientation with depth at Cajon Pass. This model considers a fault in an elastic plate, with a locked depth interval and freely slipping zones above and below, modelled as mode III edge cracks. The plate base is stress-free, and loading is in the form of laterally transmitted remote shear stress τ^{∞} (Fig. 5.6). Displacements on the two edge cracks produce anti-plane strain and modify the state of stress near the fault. By letting these unlocked parts of the fault to slip freely, the Tse et al. solution implies that they cannot sustain any significant frictional resistive stress. The model is analyzed by Tse et al. (1985) using thickness-averaged plane stress theory for lithospheric plates which slip along a discontinuity cut at the plate boundary. Wesson's (1988) analysis is basically followed below, to investigate whether possible undetected, distributed shallow creep can account for the mean stress orientation at CP.

The shear load applied to the fault zone may be represented by remote (thickness-averaged) horizontal principal stresses σ_i^r (compression taken positive), with σ_1^r oriented at an angle θ^r counterclockwise from the normal to

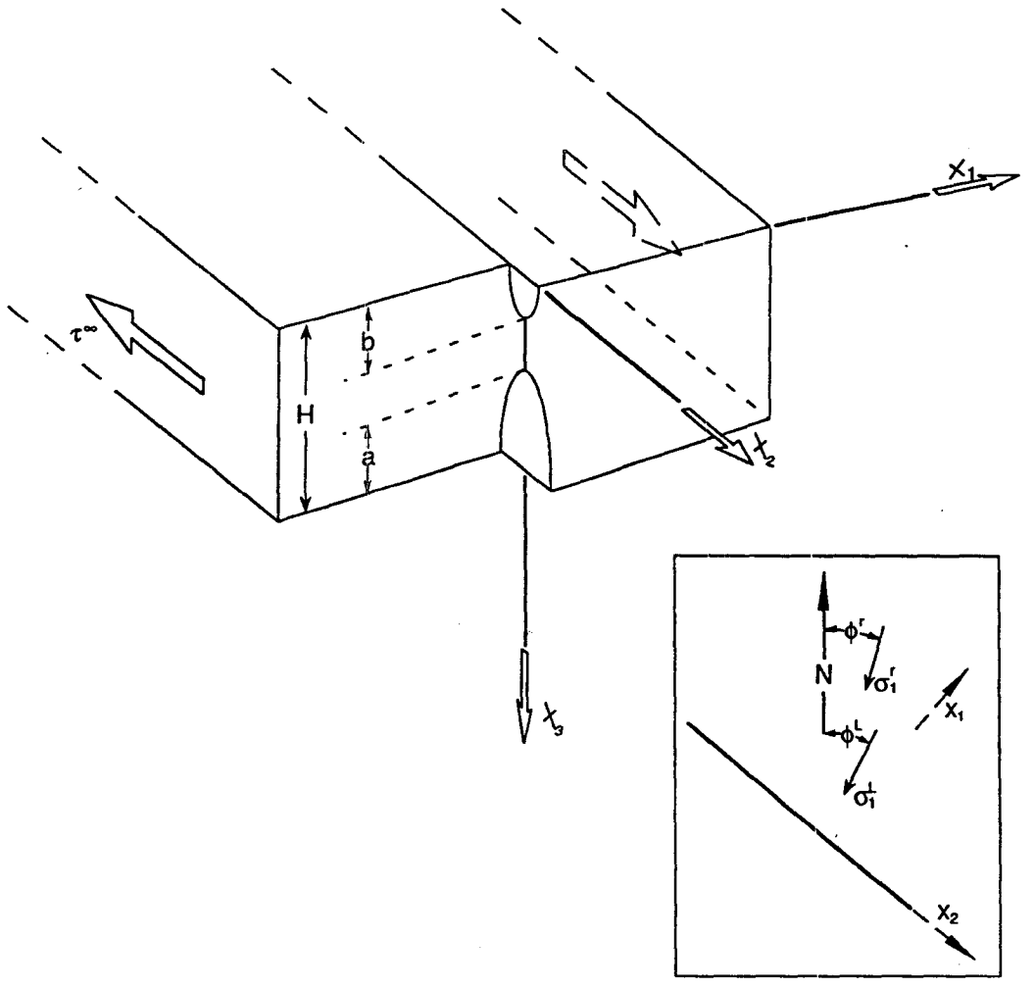

Figure 5.6 The Tse et al. (1985) model of double edge-crack in an elastic plate. b = the depth of the near-surface creeping zone; a = the thickness of the aseismicaly slipping zone below the locked strip.; H = Elastic plate thickness. The inset shows the relation among the remote and local horizontal maximum compressive stress in a horizontal view. σ_H^L, σ_H^r = Near- and far-field magnitudes, respectively, of the maximum horizontal compressive stress; ϕ^L, ϕ^r = Azimuths of σ_H^L and σ_H^r, respectively

the fault and with actual azimuth ϕ^r. In the absence of fault slip, this state of stress is resolved into the fault coordinate system x_i (Fig. 5.6) as:

$$\sigma_{11} = \frac{1}{2}(\sigma_1^r + \sigma_2^r) + \frac{1}{2}(\sigma_1^r - \sigma_2^r)\cos 2\theta^r \tag{5.1}$$

$$\sigma_{22} = \frac{1}{2}(\sigma_1^r + \sigma_2^r) - \frac{1}{2}(\sigma_1^r - \sigma_2^r)\cos 2\theta^r \tag{5.2}$$

$$\tau_{12}^r = \tau^\infty = \frac{1}{2}(\sigma_1^r - \sigma_2^r)\sin 2\theta^r \tag{5.3}$$

The thickness-averaged stress and slip at each section along the fault are related through an antiplane strain analysis (Tse et al., 1985), in which the normal stresses (eq. 5.1 and 5.2) are unchanged (i.e. independent of the slip) and can be expressed as a function of either $\{\sigma_1^r, \sigma_2^r, \theta^r\}$ or $\{\sigma_1^L, \sigma_2^L, \theta^L\}$. The shear stress parallel to the fault changes from τ^∞ as $x_2 \to \infty$, to its local value (the Tse et al. solution) in the fault near-field:

$$\tau_{12}^L = \mathrm{Re}\left(2\tau^\infty \sin\frac{\pi(x_3 + ix_1)}{H}\left\{(\beta+\alpha)^2 - \left[\beta - \alpha - 2\cos\frac{\pi(x_3 + ix_1)}{H}\right]^2\right\}^{-1/2}\right) \tag{5.4}$$

where $\alpha = \cos\frac{\pi a}{H}$ and $\beta = \cos\frac{\pi b}{H}$.

At a given section along the fault, the "local" orientation of the maximum horizontal compressive stress is therefore given by:

$$\tan 2\theta^L = \frac{2\tau_{12}^L}{\sigma_{11} - \sigma_{22}}$$

$$= 2\mathrm{Re}\left(\frac{-(\sigma_1^r - \sigma_2^r)\sin 2\phi^r}{-(\sigma_1^r - \sigma_2^r)\cos 2\phi^r}\sin\frac{\pi(x_3 + ix_1)}{H}\left\{(\beta+\alpha)^2 - \left[\beta - \alpha - 2\cos\frac{\pi(x_3 + ix_1)}{H}\right]^2\right\}^{-1/2}\right)$$

$$= 2\tan 2\theta^r\,\mathrm{Re}\left(\sin\frac{\pi(x_3 + ix_1)}{H}\left\{(\beta+\alpha)^2 - \left[\beta - \alpha - 2\cos\frac{\pi(x_3 + ix_1)}{H}\right]^2\right\}^{-1/2}\right) \tag{5.5}$$

According to this model, then, the modified orientation of the principal stresses due to fault displacements (above and below a locked section) is a

function of only the depth extent of locked and slipping zones and the remote stress orientation. It is independent of the far field stress magnitude.

Equation (5.5) provides a simple means of investigating the modification of stress orientation near a fault consisting of a locked patch with aseismic displacements above and below. As the slipping sections of the fault sustain no shear stress, the boundary condition at $x_2 = 0$ and $x_3 < b$ or $x_3 > (H-a)$, is that σ_1^L is perpendicular to the fault strike.

A lithospheric plate of thickness H = 35 km (Fig. 5.6) is considered; a thicker elastic plate has only the effect of spreading the influence of the lower aseismic zone further away from the fault, and does not affect the results at the location of the Cajon Pass drillhole. Variations of the azimuth ϕ^L of σ_1^L at a depth of 3 km as a function of distance from the SAF are shown in Figure 5.7 for two distinct loading boundary conditions:

Case 1: σ_1^r is oriented 000° (i.e. 60° clockwise from the strike of the SAF), in general agreement with stress orientations derived earthquakes near the SAF (Jones, 1988) and in the Los Angeles Basin (Hauksson, 1990). As shown in Fig. 5.7a, the deeper the lower aseismic zone, the larger is the counterclockwise rotation of σ_1^L in the near-field of the fault and the further from the fault the effect is maintained. Basically, the effect of deep aseismic slip is to induce right-lateral shear stress in the locked interval $b < x_3 < (H-a)$. This is equivalent to increasing the right-lateral shear stress by rotating σ_1^L counterclockwise towards 45° from

---

Figure 5.7. The modified orientation ϕ^L of the horizontal principal compressive stress at a depth of 3km as a function of distance from the SAF for ϕ^r= 000° (a,b) and ϕ^r= 050° (c,d) and for a shallow creeping zone of depth 5km (a,c) and an aseismically slipping zone of thickness 20km (b,d). Based on the model of Tse et al., 1985.

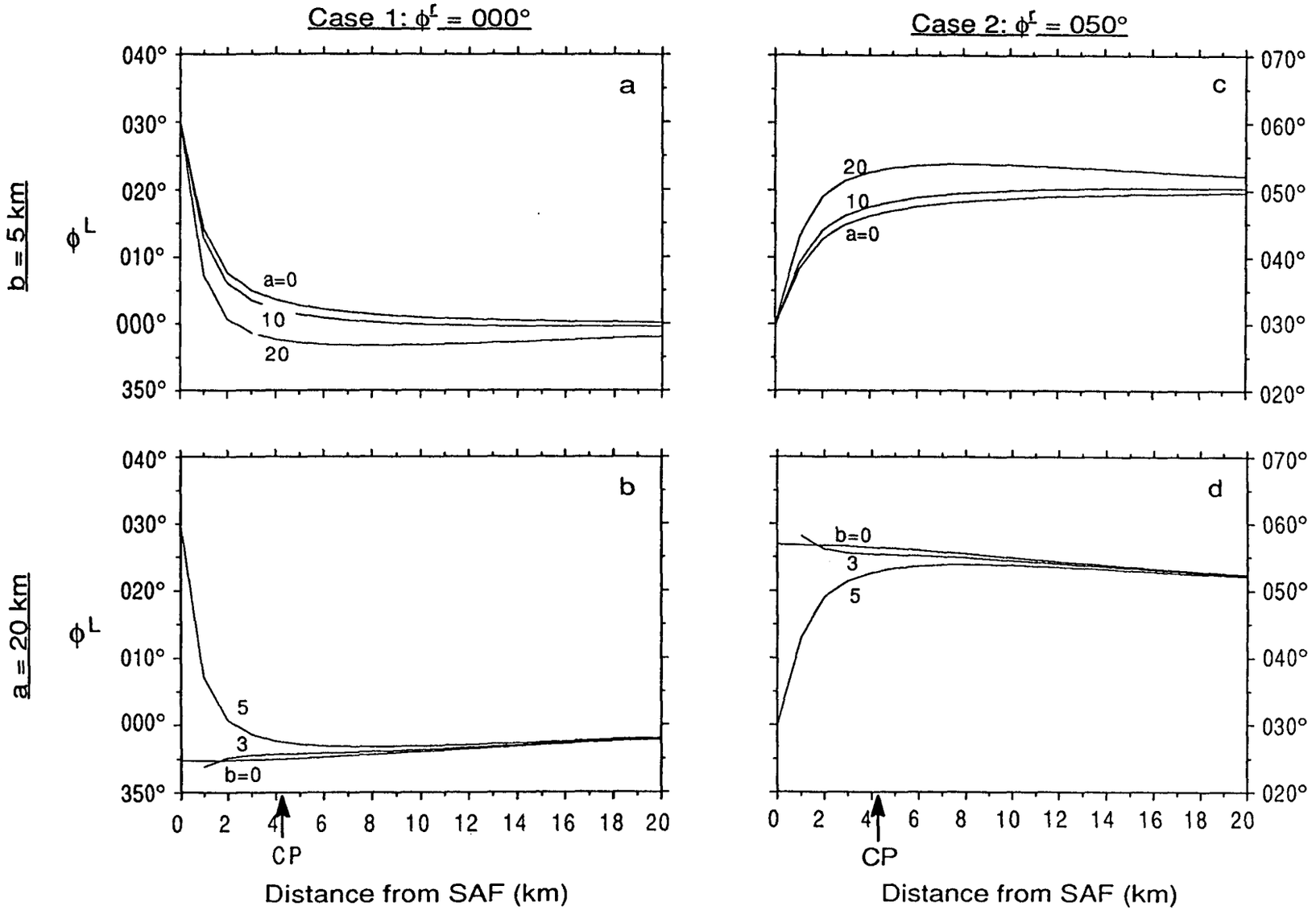
Case 1: ϕ^r = 000°
Case 2: ϕ^r = 050°
b = 5 km
a = 20 km
ϕ^L
a
b
c
d
a=0
10
20
b=0
3
5
040°
030°
020°
010°
000°
350°
070°
060°
050°
040°
030°
020°
0 2 4 6 8 10 12 14 16 18 20
CP
Distance from SAF (km)

the strike of the fault. On the other hand, the effect of increasing the depth of shallow slip (Fig.5.7b) is to reduce the right-lateral shear stress on the fault at depths $x_3<b$, thereby rotating σ_1^l towards the normal to the fault strike. Thus, the deeper the shallow creep zone, the further away from the fault is its effect of relative clockwise rotation maintained. At $x_3 = b$, ϕ^L is indeterminate due to the stress singularity at the tip of the shallow crack and, as mentioned by Wesson (1988), the dramatic change in the near-fault stress orientation there can, in principle, serve as indicator of the depth of the locked zone. In the far-field, the effect of the deep aseismic slip becomes dominant.

The effects described for this stress boundary condition are essentially the same for all orientations ϕ^r between 45° and 90° to the fault strike.

Case 2: σ_1^r is oriented 050°, i.e. 20° clockwise from the fault normal (Fig. 5.7c,d). The remote driving shear stress τ^∞ applied to the fault is therefore LL. While this far-field stress orientation is unreasonable (it would have resulted in LL aseismic fault motion and eventually in large LL earthquakes, in contradiction to the geologic record and geodetically determined strain accumulation along the SAF), it is considered for completeness. Comparison of the left and right side of Fig. 5.7 shows that the effects of the aseismic slip and the shallow creep are essentially the same as before, except that the senses of rotation are now reversed. The azimuth ϕ^L of the locally modified maximum horizontal compressive stress results in LL shear stress regardless of the depths of the aseismic motion and magnitude of the remote load. Orientations comparable to that of the Cajon Pass S_H^* can result from various fault configurations, e.g. for b=0 and a=20km (Fig. 5.7d).

The results of this analysis are summarized in Fig. 5.8 for a fault which strikes 300° and is loaded remotely by a maximum horizontal compressive stress σ_1^r at

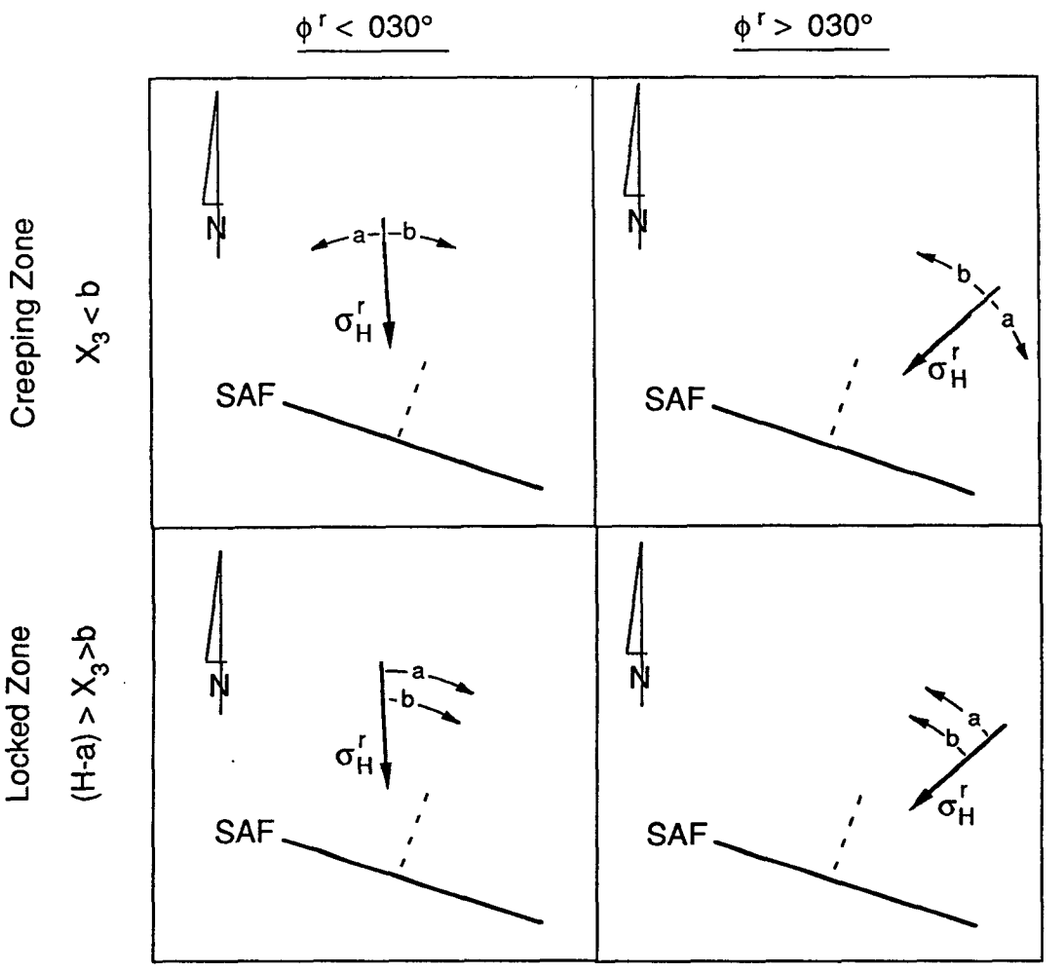

Figure 5.8. The effects (marked by arrows) of increasing the thickness of a shallow creeping zone (b) and a deep aseismic zone (a) on ϕ^L, for σ_H^r which induces RL ($\phi^r < 030°$) and LL ($\phi^r > 030°$) shear stress along the SAF, as observed within the creeping zone (upper plots) and the locked zone (lower plots).

an azimuth ϕ^r. The sense of the changes in ϕ^L due to the effects of deep aseismic slip and shallow creep are shown by arrows. The general conclusion is that, in the context of this model, fault-parallel LL shear stress can exist in the SAF near-field only if the remotely applied horizontal shear stress is also LL. As this possibility is unacceptable, neither the orientation of the remotely applied load nor the existence of a shallow creep zone can explain LL shear stress across the San Andreas fault near Cajon Pass.

5.4 Discussion

Based on an analysis of the interseismic loading of the locked zone of the San Andreas Fault (Tse et al., 1985), the shear stress across the fault could be left-lateral only if the remotely applied load is left-lateral as well, which is unacceptable. Therefore, fault-parallel left-lateral shear stress cannot be the result of aseismic slip on the San Andreas Fault near Cajon Pass. The dislocation model used above to estimate the shear stress budget near CP in the first 178 years of the current cycle has shown that

1) The 1812 earthquake, with about 4m of right-lateral slip near Cajon Pass (Weldon and Sieh, 1985), induced a shear stress change on the order of -3.5 MPa at a depth of 3km in the drillsite area;

2) The shear stress decrease on the fault has almost been balanced by the combined effects of the lower crustal aseismic slip and the positive (right-lateral) shear stress induced by the 1857 earthquake. At Cajon Pass, the calculated net shear stress change since the 1812 earthquake is on the order of -1MPa;

3) The effect of the strike changes along the SAF near CP is to reduce some of the right-lateral loading as well as to slightly enhance the 1812 stress drop;

4) The overall effect of slip along the SJF on the shear stress at CP appears to be negligible.

Since the most obvious source of left-lateral shear stress near a major right-lateral fault is the stress drop during large earthquakes, there was apparently more left-lateral shear stress parallel to the SAF in this area immediately after the 1812 earthquake compared to its present day level. Thus, stress accumulation due to deep aseismic slip has apparently not balanced the 1812 stress drop to date. One factor which may theoretically increase the amount of left-lateral shear at the time of the earthquake is dynamic overshoot, i.e. when the final stress after an earthquake is lower than the dynamic frictional level. Fig. 5.9a is a schematic representation of the different stress terms involved in a simple, one-dimensional fault model (i.e. a block and spring model) with spatially and temporally constant friction. In simple faulting models, $\tau_{fi} = \tau_d$, the stress drops during the earthquake exactly to the dynamic frictional level ($\tau_d^{(2)}$ in 5.8a; Orowan, 1960), or $\tau_{final} > \tau_d$, i.e. the earthquake rupture is blocked before stress drops to the dynamic frictional level, resulting in relatively small stress drops ($\tau_d^{(3)}$ in 5.8a; Housner, 1955; Smith et al., 1989). Savage and Wood (1971) pointed out, however, that if earthquake rupture is stopped by friction, inertia of the displaced blocks requires that the final stress τ_{fi} must 'overshoot' (i.e. be lower than) the dynamic frictional stress τ_d, and the static stress drop would be greater than the dynamic stress drop. They show that in this case $\tau_a < \frac{\Delta\tau}{2}$ (where τ_a = apparent (radiative) stress and $\Delta\tau$ = stress change during faulting = τ_{in}-τ_{fi}; $\tau_d^{(1)}$ in Fig. 5.9a) and suggest that overshoot may occur in many

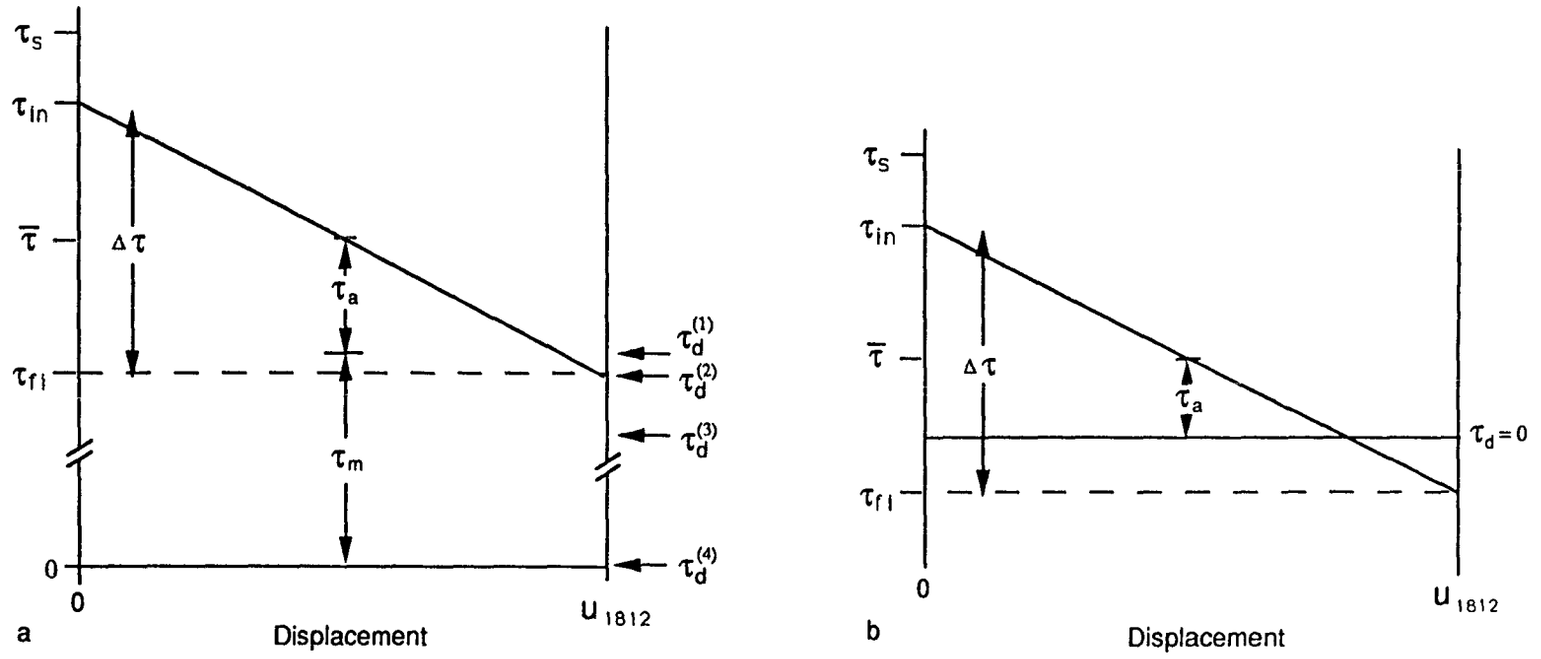

Figure 5.9 The change in earthquake-related stress terms as a function of displacement in a one-dimensional earthquake model with constant friction. τ_s = Static frictional (tectonic) stress; τ_{in} = Initial (pre-earthquake) stress; τ_{fi} = Final stress; $\bar{\tau} = \frac{\tau_{in} + \tau_{fi}}{2}$ = Mean long term stress ; $\Delta\tau = \tau_{in} - \tau_{fi}$ = Stress drop; τ_a = Apparent (radiative) stress; τ_m = Stress expended for mechanical work; τ_d = Dynamic friction stress level. (a) The general case, with unspecified absolute stress level. (b) Overshoot below the zero stress level with vanishing dynamic frictional stress (i.e. $\tau_{fi} < \tau_d = 0$).

earthquakes. The Savage-Wood expression simply means that the energy released as seismic radiation is non-zero and therefore that overshoot must be smaller than 50%. Several theoretical models considering the dynamic propagation of uniform cracks (e.g. Burridge and Halliday, 1971; Madariaga, 1976) showed that an overshoot exceeding 30% is possible.

If one hypothesizes that the overshoot mechanism contributed to the left-lateral shear observed at Cajon Pass, it requires not only that the final 1812 fault stress dropped below the dynamic frictional level, but also that it became negative, i.e. left lateral, as in Fig. 5.9b. For the seismic cycle since 1812, a crude balance of the fault shear stress is

$$\tau_c = \tau_s + \Delta\tau_{1812} + \Delta\tau_{1857} + \tau_r \qquad (5.6)$$

where

τ_c = Current shear stress parallel to the SAF at Cajon Pass (measured by hydrofracs) = -3.5±3.0 MPa at ~3km depth;

τ_s = Static frictional stress;

$\Delta\tau_{1812}$ = Stress drop at Cajon Pass during the 1812 earthquake = ~-3MPa;

$\Delta\tau_{1857}$ = Stress change at Cajon Pass due to the 1857 earthquake= ~0.35MPa;

τ_r = Aseismically recovered stress since 1812 = ~2MPa,

and τ_d is assumed to drop to zero during the earthquake. If a maximum hypothetical overshoot of 50% is assumed for the 1812 earthquake (i.e. zero seismic radiation), then τ_s=1.5MPa and the left side of Eq. 5.6 equals 0.85MPa, inconsistent with the measured value of τ_c (to the degree that a simple expression like Eq. 5.6 can be used). Furthermore, Smith et al. (1989), analyzing spectral parameters for medium and large earthquakes, show that the Savage-Wood inequality is usually violated, with final earthquake stresses

higher than the dynamic frictional stress. In that case, even if $\tau_d=0$, (i.e. fault stress vanishes due to, e.g., fault melting [McKenzie and Brune, 1972], acoustic fluidization [Melosh, 1979] or transient elevated pore pressures during faulting [Lachenbruch and Sass, 1980]), faulting would stop with some residual right-lateral shear acting on the fault.

APPENDICES

A.1: Polyaxial stress state near a borehole inclined with respect to the principal stresses

The state of stress around a borehole inclined with respect to the remote principal stresses (Hiramatsu and Oka, 1962), where the borehole fluid pressure is in equilibrium with the pore pressure in the surrounding rock, is given by

$$\sigma_{rr} = \left(1 - \frac{r^2}{R^2}\right)\frac{\sigma^{\infty}_{11} + \sigma^{\infty}_{22}}{2} + \left(1 - 4\frac{r^2}{R^2} + 3\frac{r^4}{R^4}\right)\left(\frac{\sigma^{\infty}_{11} - \sigma^{\infty}_{22}}{2}\cos 2\theta + \sigma^{\infty}_{12}\sin 2\theta\right)$$

$$+ P_b - \frac{r^2}{R^2}P_0 \qquad \text{A.1.1}$$

$$\sigma_{\theta\theta} = \left(1 + \frac{r^2}{R^2}\right)\frac{\sigma^{\infty}_{11} + \sigma^{\infty}_{22}}{2} - \left(1 + 3\frac{r^4}{R^4}\right)\left(\frac{\sigma^{\infty}_{11} - \sigma^{\infty}_{22}}{2}\cos 2\theta + \sigma^{\infty}_{12}\sin 2\theta\right)$$

$$- \frac{r^2}{R^2}P_0 \qquad \text{A.1.2}$$

$$\sigma_{zz} = \sigma^{\infty}_{33} - 4\nu\frac{r^2}{R^2}\left(\frac{\sigma^{\infty}_{11} - \sigma^{\infty}_{22}}{2}\cos 2\theta + \sigma^{\infty}_{12}\sin 2\theta\right) \qquad \text{A.1.3}$$

$$\sigma_{\theta z} = \left(1 + \frac{r^2}{R^2}\right)\left(\sigma^{\infty}_{23}\cos\theta - \sigma^{\infty}_{31}\sin\theta\right) \qquad \text{A.1.4}$$

$$\sigma_{zr} = \left(1 - \frac{r^2}{R^2}\right)\left(\sigma^{\infty}_{31}\cos\theta + \sigma^{\infty}_{23}\sin\theta\right) \qquad \text{A.1.5}$$

$$\sigma_{\theta r} = \left(1 + \frac{r^2}{R^2} - 3\frac{r^2}{R^4}\right)\left(\frac{\sigma^{\infty}_{22} - \sigma^{\infty}_{11}}{2}\sin 2\theta + \sigma^{\infty}_{12}\cos 2\theta\right) \qquad \text{A.1.6}$$

where

σ^{∞}_{ij} - Remote stress field (with respect to the borehole)

r,θ, z - cylindrical borehole coordinates

R - Borehole radius

ν - Poisson's ratio

P_0 - Pore pressure in the surrounding rocks.

At the borehole wall, r = R, $\sigma_{zr} = \sigma_{\theta r} = 0$ and the radial stress equals the pore fluid pressure. The circumferential stress is then

$$\sigma_{\theta\theta} = \sigma^{\infty}_{11} + \sigma^{\infty}_{22} - 2\left(\sigma^{\infty}_{11} - \sigma^{\infty}_{22}\right)\cos 2\theta - 4\sigma^{\infty}_{12}\sin 2\theta - P_0 \qquad \text{A.1.7}$$

which is equation 1.1

A.2: Borehole televiewer calibration

The borehole televiewers used in Cajon Pass drillhole were calibrated before each log in order to determine, first, the error in magnetic north reading of the tool and, second, the acoustic wave velocity in the drilling fluid, which then served to translate travel time information to borehole radii information. During calibration, the BHTV stationary and operating in a double-radius container (Fig. A.2.1), filled with drilling fluid. The step in the container radius is oriented accurately with respect to the true magnetic north and appears as a sharp color change in the graphic output (Fig. A.2.2, left). The deviation of this color change from the tool magnetic north (i.e. the edge of the image) provides the error in the magnetic north reading of the BHTV. Appropriate corrections are then applied to the output from the log following the specific calibration run. Finally, the

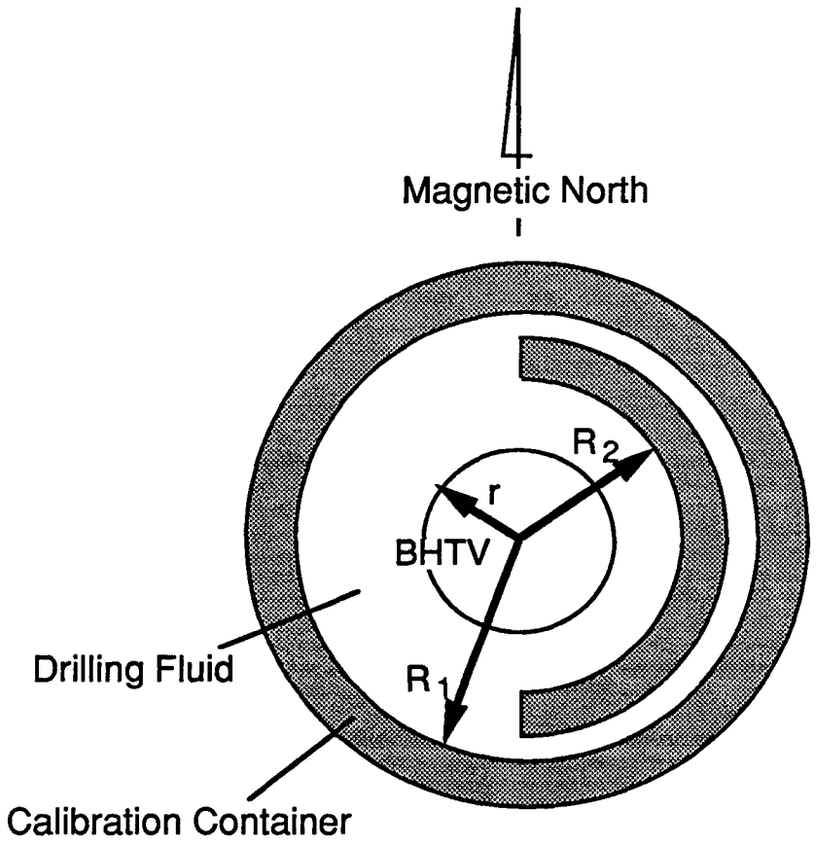

Figure A.2.1 Cross sectional view of the BHTV calibration container. r - BHTV radius; R_1,R_2 - Container inner radii.

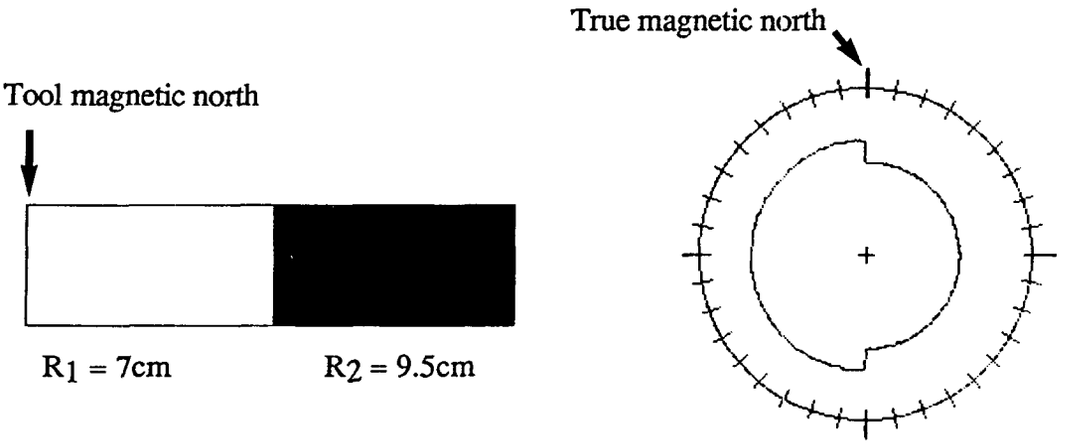

Figure A.2.2 BHTV calibration output. The change in color in the 360° image (left) marks the change in container inner radius, also seen in a cross sectional view on the right. In this particular example the radius step is oriented N-S and there is no shift between the tool magnetic north (the edge of the image) and the true magnetic north.

magnetic declination at Cajon Pass (15°) is added to obtain the orientation of the borehole features with respect to geographic north.

The temporal sequence of events from the generation of the reference sync pulse to the arrival back at the transducer can be described schematically as follows:

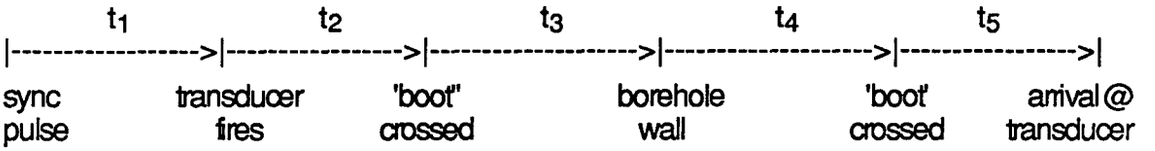

where

t_1 = 16 μs

$t_2 = t_5 = \delta t$ = Travel time within the tool (unknown)

$t_3 = t_4 = (r-R)/V$ = Travel time in borehole fluid

r = Tool radius

R = Container inner radius.

Then

$$\delta t = (t_{tot} - 16 - 2(r-R)/V)/2 \qquad \text{(A.2.1)}$$

$$V = (2(r-R)/(t_{tot} - 16 - 2\delta t) \qquad \text{(A.2.2)}$$

where t_{tot} is the total travel time, read directly from the analog data or from the acoustic seismogram. δt is a tool constant and was determined for each of the BHTV's used in Cajon Pass using Eq. A.2.1. Mud velocity was then determined from Eq. A.2.2 using travel times obtained in the cased part of the hole, where the radius is known and the temperature conditions are closer to those of real-time logging.

A.3 Effects of lithological and drilling parameters on breakout orientation in the Cajon Pass drillhole

In order to investigate the source of breakout orientation variations in the Cajon Pass drillhole, the orientation of the apparent maximum horizontal compressive stress was compared with the percent of biotite recovered in the cuttings, the rate of penetration as monitored continuously during drilling, and the drift and azimuth of the wellbore which were determined in occasional surveys. As Fig. A.3.1 shows, there is no correlation between the S_H^* orientation and the drilling parameters.This rules out the possibility that the drilling operations were responsible for the variations in breakout orientation. The percentage of biotite is a general indicator of the degree of strength anisotropy in the rocks, as biotite itself is highly anisotropic and form interlayering in mildly metamorphosed rocks such as those encountered in the Cajon Pass drillhole. Except possibly at a few localities (e.g. near a depth of 2250m), there is correlation between breakout orientation variations and biotite content in the drilled rocks. This, and the generally shallow dip of foliation in the drilled rocks indicate that strength anisotropy is generally unimportant in affecting breakout orientation.

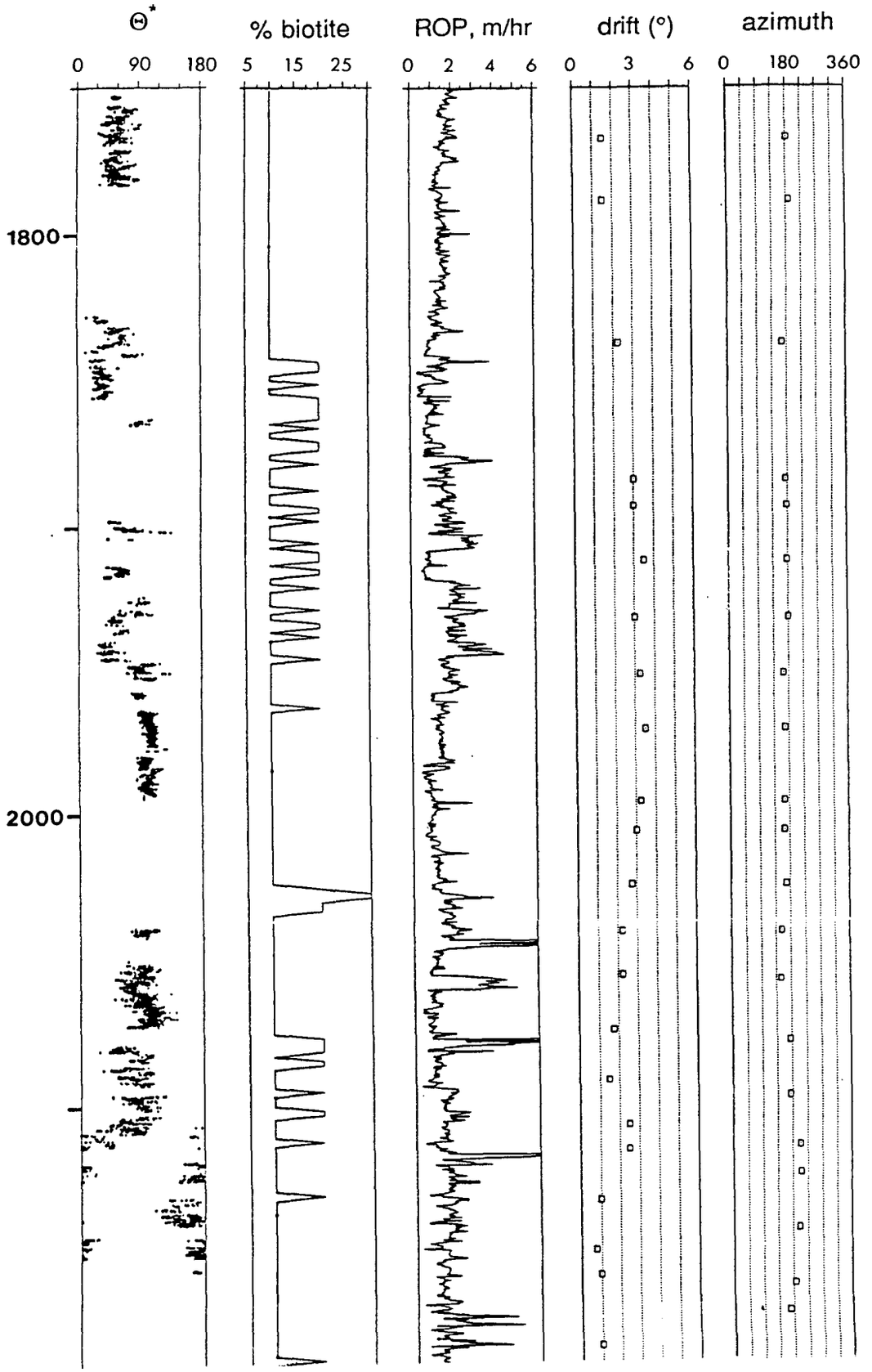
Θ*
0 90 180
% biotite
5 15 25
ROP, m/hr
0 2 4 6
drift (°)
0 3 6
azimuth
0 180 360
1800
2000

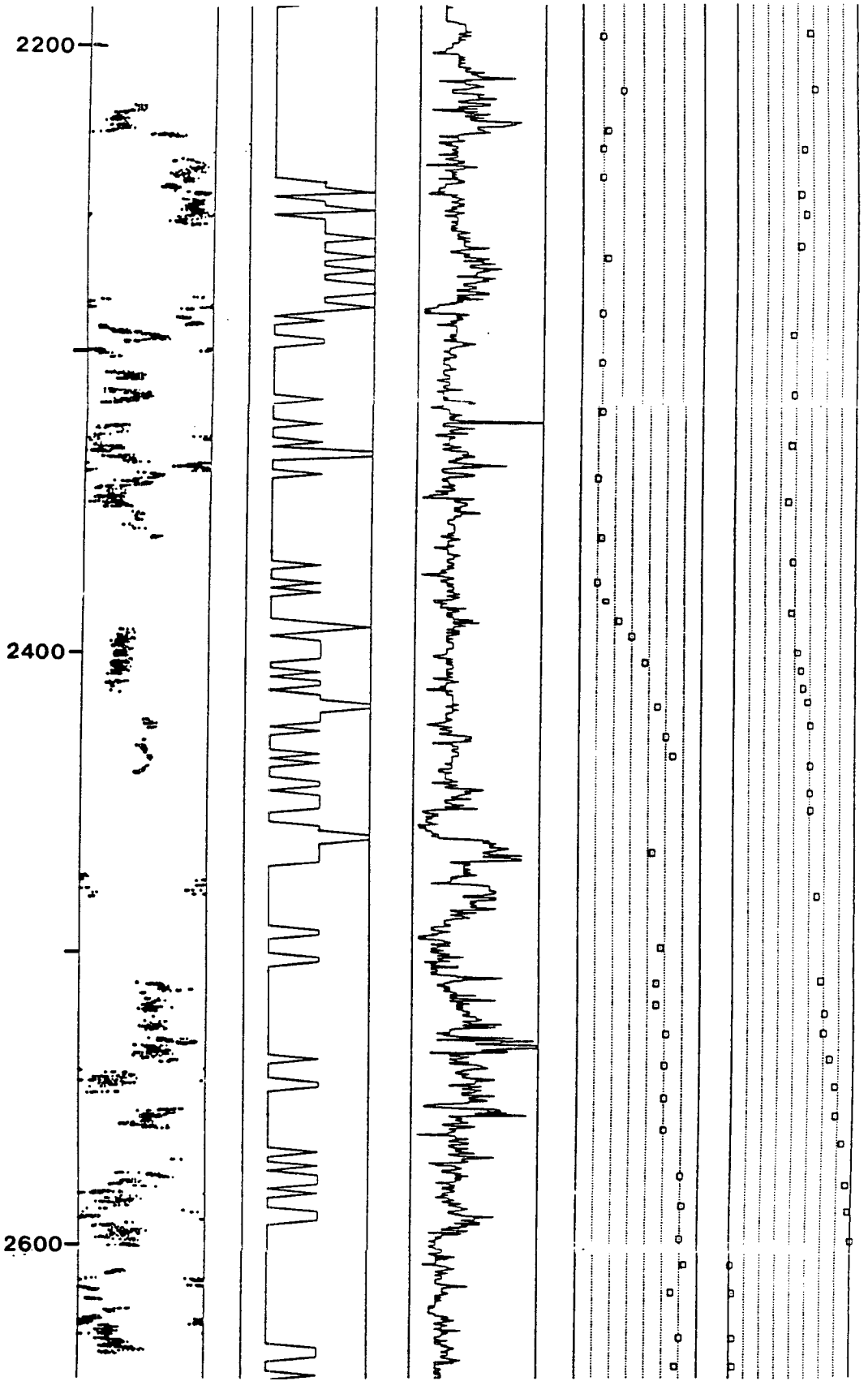
2200
2400
2600

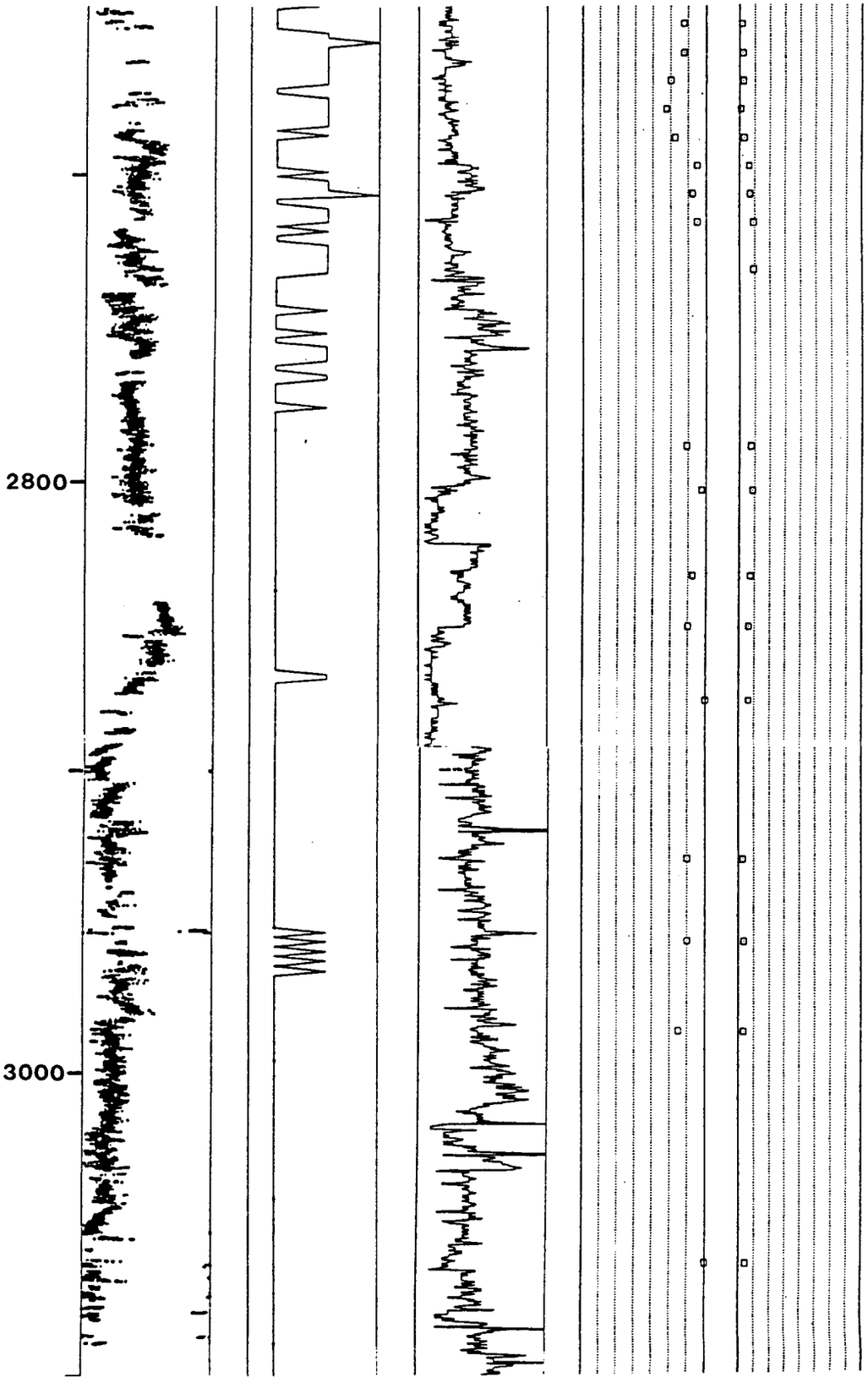
2800
3000

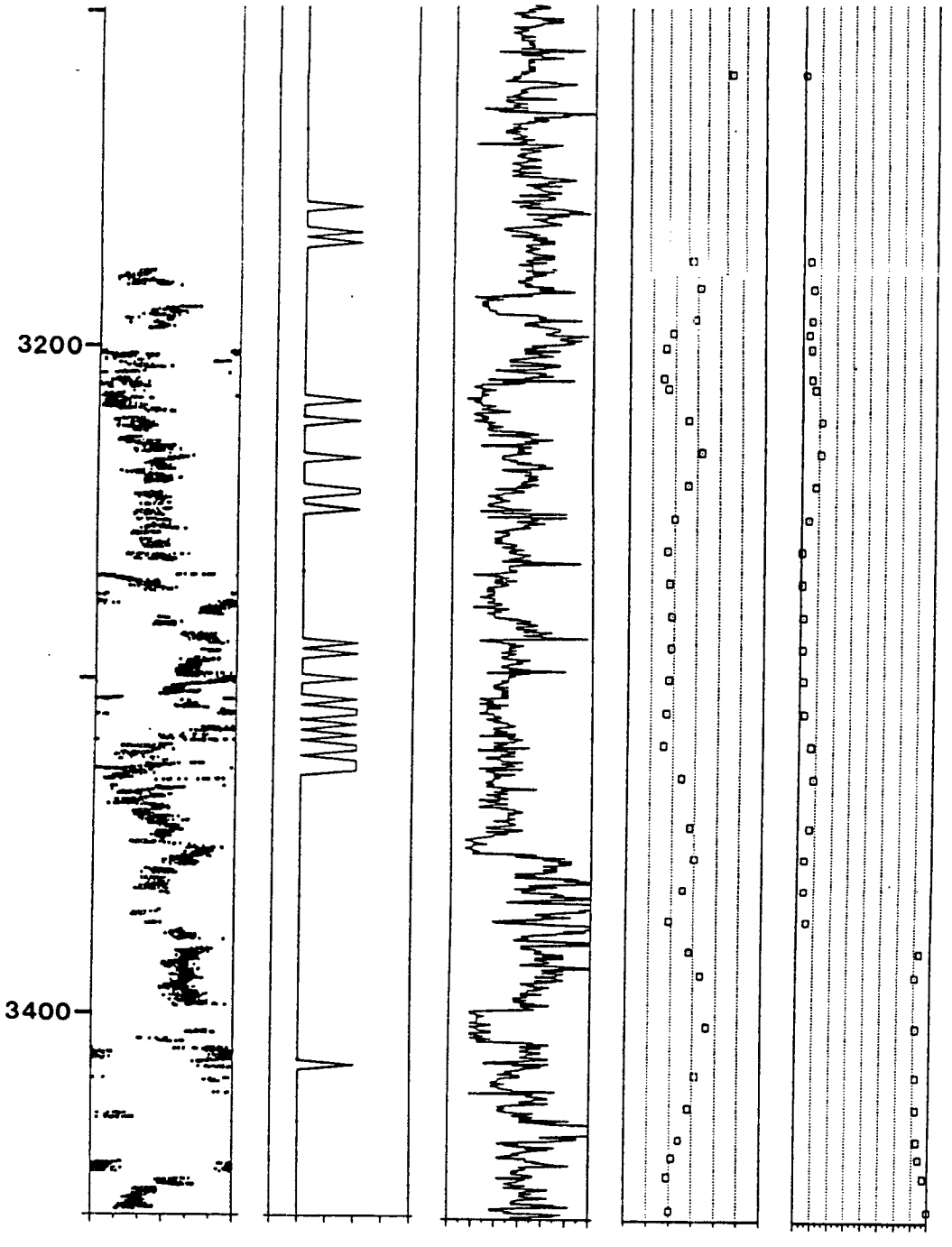

Figure A.3.1 Comparison between the azimuth of the apparent maximum horizontal compressive stress S_H^*, the percent of biotite in cuttings, hte rate of penetration, the drift and the azimuth of the borehole, throughout the depth interval 1750-3460m in the Cajon Pass borehole.

REFERENCES

Agnew, D. and K.E. Sieh, A documentary study of the felt effects of the great California earthquake of 1857, *Bull. Seismol. Soc. Am.*, 68, 1717-1729, 1978.

Aki, K., Asperities, barriers, characteristic earthquakes and strong motion prediction, *J. Geophys. Res.*, 89, 5867-5872, 1984.

Aki, K., Magnitude-frequency relation for small earthquakes: A clue to the origin of f(max) of large earthquakes, *J. Geophys. Res.*, 92, 1349-1355, 1987.

Archuleta, J. R., E. Cranswick, C. Mueller and P. Spudich, Source parameters of the 1980 Mommoth Lakes, California, earthquake sequence, *J. Geophys. Res.*, 87, 4595-4607, 1982.

Bak, P., C.Tang and K. Wiesenfeld, Self-organized criticality, *Physical Reviews*, 38, 364-374, 1988.

Bakun, W. H., C.G. Bufe and R.M. Stewart, Body wave spectra of central California earthquakes, *Bull. Seismol. Soc. Am.*, 66, 439-459, 1976.

Barton, C. A., Development of in-situ stress measurement techniques for deep boreholes, Ph.D. Dissertation dissertation, 192 pp., Stanford University, 1988.

Barton, C. A. and M.D. Zoback, Self-similar distribution and properties of macroscopic fractures at depth in crystalline rock in the Cajon pass Scientific drillhole, *subm. to J. Geophys. Res.*, 1990.

Baumgartner, J., J. Carvalho and J. McLennan, Fracturing deviated boreholes - an experimental laboratory approach, *Proc. Rock at Great Depth*, edited by V. Maury, D. Fourmaintraux, 929-938, Pau, France, 1989.

Baumgartner, J., M. D. Zoback, J. Healy and B. O'Neill, A detailed interpretation of the Cajon Pass hydraulic fracturing stress measurements, *EOS Trans., Am. Geophys. U.*, 70, 480, 1989.

Bell, J. S. and D.I. Gough, Northeast southwest compressive stress in Alberta: Evidence from oil wells, *EPSL*, 45, 475-482, 1979.

Bott, M. P. H., The mechanics of oblique slip faults, *Geol. Mag.*, 96, 109-117, 1959.

Burridge, R. and G.S. Halliday, Dynamic shear cracks with friction as models for shallow focus earthquakes, *Geophys. J. R. astr. Soc.*, 25, 261-283, 1971.

Chinnery, M. A., Theoretical fault models, *Proc. A symposium on processes in the focal region, v.37, no. 7*, edited by K. Kasahara, A.E. Stevens, Ottawa, Canada, 1967.

Chouet, B., K. Aki and M. Tsujiura, Regional variation of the scaling law of earthquake source spectra, *Bull. Seismol. Soc. Am.*, 68, 49-79, 1978.

Cox, J. W., Long axis orientation in elongated boreholes and its correlation with rock stress data, *Proc. 24th Annual Logging Symposium, Soc. Prof. Well Log. Anal.*, Calgary, Alberta, 1983.

Crowel, J., Displacement along the San Andreas fault, California, *Geol. Soc. Am. Spec. Pap.*, 71, 1-61, 1962.

Daneshy, A. A., A study of inclined hydraulic fractures, *J. Soc. Pet. Eng.*, 13, 61-68, 1973.

Das, S. and K. Aki, Fault plane with barriers: A versatile earthquake model, *J. Geophys. Res.*, 82, 5658-5670, 1977.

Davis, J. C., *Statistics and data analysis in geology*, John Wiley & Sons, Canada, 1986.

Dunbar, S., DIS3D a three dimensional fault modelling program, Unpublished manuscript, 1984.

Eaton, J. P., M. E. O'Neill and J. N. Murdock, Aftershocks of the 1966 Parkfield-Cholame, California, earthquake: A detailed study, *Bull. Seismol. Soc. Am.*, 60, 1151-1197, 1970.

Erickson, L., User's manual for DIS3D: A three dimensional dislocation program with applications to faulting in the earth, 167 pp., Stanford University, 1987.

Ewy, R. T. and N.G.W. Cook, Fracture processes around highly stressed boreholes, *Proc. Drilling Symposium 1989*, edited by J.C. Rowley, 63-70, Texas, 1989.

Ewy, R., N.G.W. Cook and L.R. Meyer, Hollow cylinder tests for studying fracture around underground openings, *Proc. Proc. U.S. Symp. Rock Mech. 29th*, 67-74, 1988.

Fletcher, J., A comparison between the tectonic stress measured in situ and stress parameters from induced seismicity at Monticello reservoir, south California, *J. Geophys. Res.*, 87, 6931-6944, 1982.

Fletcher, J. B., Spectra from high-dynamic range digital recordings of Oroville, California aftershocks and their source parameters, *Bull. Seismol. Soc. Am.*, 70, 735-755, 1980.

Frankel, A., J. Fletcher, F. Vernon, L. Haar, J. Berger, T. Hanks and J. Brune, Rupture chracteristics and tomographic source imaging of M(L)~3 earthquakes near Anza, southern California, *J. Geophys. Res.*, 91, 12633-12650, 1986.

Rodgers, T. H., Geologic map of California - San Bernardino sheet (compilation), scale 1:25000, 1967.

Gough, D. I. and J.S. Bell, Stress orientation from borehole wall fractures with with examples from Colorado, east Texas and northern Canada, *Can. J. Earth Sci.*, 19, 1358-1370, 1982.

Haimson, B. C. and C.G. Herrick *Proc. International symposium on rock Stress and Rock Stress Measurements*, 271-280, Stockholm, 1986.

Haimson, B. C. and C.G. Herrick *Proc. 26th US Symposium on rock mechanics*, 1207-1218, Rapid city, SD, 1985.

Hanks, T. C., Earthquake stress drops, ambient tectonic stresses and stresses that drive plate motions, *Pageoph*, 115, 441-458, 1977.

Hanks, T. C., The faulting mechanism of the San Fernando earthquake, *J. Geophys. Res.*, 79, 1215-1229, 1974.

Hayashi, K., T. Shoji, H. Niitsuma, T. Ito and H. Abe, A new in-situ tectonic stress measurement and its application to a geothermal model field, *Geothermal Resources Council Transactions*, 9, 99-104, 1985.

Henyey, T. L., Heat flow near major strike slip faults in California, Ph.D. thesis dissertation, Calif. Inst. of Technol., 1968.

Henyey, T. L. and G.J. Wasserburg, Heat flow near major strike slip faults in California, *J. Geophys. Res.*, 76, 7924-7946, 1971.

Hickman, S. H., J.H. Healy and M.D. Zoback, In situ stress, natural fracture distribution and borehole elongation in the Auburn geothermal well, Auburn, New York, *J. Geophys. Res.*, 90, 1985.

Hickman, S. H., M.D. Zoback and J.H. Healy, Continuation of a deep borehole stress measurement profile near the San Andreas fault, I: Hydraulic fracturing stress measurements at Hi Vista, Mojave Desert, California, *J. Geophys. Res.*, 93, 15183-15195, 1988.

Hill, M. and T. Dibblee, San Andreas, Garlock and Big Pine faults, California - A study of their character, history and tectonic significance of their displacements, *Geol. Soc. Am. Bull.*, 64, 443-458, 1953.

Hiramatsu, Y. and Oka Y., Stress around a shaft or level excavated in ground with a three dimensional stress state, *Mem. Fac. Eng. Kyoto Univ.*, 24, 56-76, 1962.

Hirata, T., Omori's power law aftershock sequence of microfracturing in rock fracture experiments, *J. Geophys. Res.*, 92, 6215-6221, 1987.

Hirth, J. P. and J. Lothe, *Theory of dislocations*, John Wiley & Sons, 1982.

Jacoby, G., P.R. Sheppard and K.E. Sieh, Irregular recurrence of large earthquakes along the San Andreas fault - evidence from trees, *Science*, 244, 196-199, 1988.

Jones, L. M., Focal mechanisms and the state of stress on the San Andreas fault in southern California, *J. Geophys. Res.*, 93, 8869-8891, 1988.

Kagan, Y. Y. and L. Knopoff, Stochastic synthesis of earthquake catalogs, *J. Geophys. Res.*, 86, 2853-2862, 1981.

Kanamori, H. and G.S. Stewart, Seismological aspects of the Guatemala earthquake of Feb. 4, 1976, *J. Geophys. Res.*, 83, 3427-3434, 1978.

Kirsch, G., Die theorie der elastizitat und die Dedurfnisse der fertigkeirslehre, *Zeitschrift der Vereines Deutscher Ingenieure*, 42, 797, 1898.

Kuriyagawa, M., H. Kobayashi, I. Matsunaga, T. Yamaguchi and K. Hibiya, Application of hydraulic fracturing to three dimensional In situ stress measurement, *Int. J. Rock Mech. Min. Sci. & Geomech. Abstr.*, 26, 587-593, 1989.

Lachenbruch, A. H., Frictional heating, fluid pressure and the resistance to fault motion, *J. Geophys. Res.*, 85, 6097-6112, 1980.

Lachenbruch, A. H., Mechanics of thermal contraction cracks and ice-wedge polygons in permafrost, *Geol. Soc. Am. Spec. Pap.*, 70, 1-67, 1962.

Lachenbruch, A. H. and J.H. Sass, Heat flow and energetics of the San Andreas fault zone, *J. Geophys. Res.*, 85, 6185-6222, 1980.

Lachenbruch, A. H. and J.H. Sass, The stress-heat flow paradox and thermal results from Cajon Pass, *Geophys. Res. Lett.*, 15, 981-984, 1988.

Lachenbruch, A. H. and J.H. Sass, Thermo-mechanical aspects of the San Andreas fault system, *Proc. Tectonic problems of the San Andreas fault system*, edited by R.L. Kovatch, A. Nur, 192-205, Stanford, California, 1973.

Lawson, A. C. et al., The California earthquake of April 18, 1906, Report of the State Earthquake Investigation Commission, 451 pp., 1908.

Leeman, E. R., The measurement of the stress in the ground surrounding mining excavations, in *Papers and Discussions, 1958-59*, pp. 331-356, The Transval and Orange Free State Chamber of Mines, South Africa, 1960.

Li, V. C. and J.R. Rice, Crustal deformation in great California earthquake cycles, *J. Geophys. Res.*, 92, 11533-1551, 1987.

Louie, J. N., C.R. Allen, D.C. Johnson and P.C. Hasse, Fault slip in southern California, *Bull. Seismol. Soc. Am.*, 75, 811-834, 1985.

Madariaga, R., Dynamics of an expanding circular fault, *Bull. Seismol. Soc. Am.*, 66, 639-666, 1976.

Madariaga, R., On the relation between seismic moment and stress drop in the presence of stress and strength heterogeneity, *J. Geophys. Res.*, 84, 2243-2250, 1979.

Mandelbrot, B., *Fractals: Form, chance and dimension*, W.H. Freeman, San Francisco, California, 1977.

Marple, S. L., *Digital spectral analysis*, Prentice=Hall, Inc., New Jersey, 1987.

Mastin, L. G., The development of borehole breakouts in sandstone, M.S. thesis dissertation, Stanford University, 1984.

McGarr, A., D.D. Pollard, N.C. gay and W.O. Oertlepp, Analysis of actual Fault Zones in Bedrock, U.S. Geol. Surv. Open File Rep., 79-1239, 1979.

McGarr, A., M.D. Zoback and T.C. Hanks, Implications of an elastic analysis of in situ stress measurements near the San Andreas fault, *J. Geophys. Res.*, 87, 7797-7806, 1982.

Mogi, K., Magnitude frequency relation for elastic shocks accompanying fractures of various materials and some related problems in earthquakes, *Bull. Earthquake Res. Inst.*, 40, 831-853, 1962.

Moos, D. and M.D. Zoback, Utilization of observations of well bore failure to constrain the orientation and magnitude of crustal stresses: Application to continental, deep sea drilling project and ocean drilling program boreholes, *J. Geophys. Res.*, 95, 9305-9325, 1990.

Mount, V. S. and J. Suppe, State of stress near the San Andreas fault: Implications for wrench tectonics, *Geology*, 15, 1143-1146, 1987.

Nur, A., Nonuniform friction as a physical basis for earthquake mechanics, *Pageoph*, 116, 964-991, 1978.

Nur, A. and M. Israel, The role of heterogeneities in faulting, *Phys. Earth Plan. Int.*, 21, 225-236, 1980.

O'Neil, J. R. and T.C. Hanks, Geochemical evidence for water-rock interaction along the San Andreas and Garlock Faults of California, *J. Geophys. Res.*, 85, 6286-6292, 1980.

E. Orowan, Mechanics of seismic faulting, in *Rock deformation*, edited by D. Griggs and J. Handin, pp. 323-373, GSA mem., 79, 1960.

Pechman, J. C. and H. Kanamori, Waveforms and spectra of pre-shocks and aftershocks of the 1979 Imperial Valley, CA earthquake: Evidence for fault heterogeneity?, *J. Geophys. Res.*, 87, 10579-10597, 1982.

Plumb, R. A. and J.W. Cox, Stress directions in eastern North America determined to 4.5 km from borehole elongation measurements, *J. Geophys. Res.*, 92, 4805-4816, 1987.

Plumb, R. A. and S.H. Hickman, Stress-induced borehole elongations: A comparison between the 4-arm dipmeter and the borehole televiewer in the Auburn geothermal well, *J. Geophys. Res.*, 90, 1985.

Press, W. H., B.P. Flannery, S.A. Teukolsky and W.T. Vatterling, *Numerical Recipes*, Cambridge University Press, Cambridge, 1986.

Rautian, T. G., V.I. Khalturin, V.G. Martynov and P. Molnar, Preliminary analysis of the spectral content of P and S waves from local earthquakes in the Garm, Tdjikistan region, *Bull. Seismol. Soc. Am.*, 68, 949-971, 1978.

Reasenberg, P. and W.L. Ellsworth, Aftershocks of the Coyote Lake, CA, earthquake of August 6, 1979: A detailed study, *J. Geophys. Res.*, 87, 10637-10655, 1982.

Rudnicki, J. W. and H. Kanamori, Effects of fault interaction on moment, stress drop, and strain energy release, *J. Geophys. Res.*, 86, 1785-1793, 1981.

Rudnicki, J. W., K. Hirashima and J.D. Achenbach, Amplification of moment and strain energy release due to interaction between different size fault slip zones, *J. Geophys. Res.*, 89, 5828-5834, 1984.

Savage, J.C., Dislocations in seismology, in *Dislocations in solids*, edited by F.R.N. Nabarro, North-Holland Company, 1980.

Savage, J. C. and G. Gu, The 1979 Palmdale, California, strain event in retrospect, *J. Geophys. Res.*, 90, 10301-10309, 1985.

Savage, J. C. and L. M. Hastie, Surface deformation associated with dip slip faulting, *J. Geophys. Res.*, 71, 4879-4904, 1966.

Savage, J. C. and M. D. Wood, The relation between apparent stress and stress drop, *Bull. Seismol. Soc. Am..*, 61, 1381-1388, 1971.

Savage, J. C. and R.O. Burford, Geodetic determination of relative plate motion in central California, *J. Geophys. Res.*, 78, 832-845, 1973.

Savage, J. C., W.H. Prescott and G.H. Gu, Strain accumulation in southern California, 1973-1984, *J. Geophys. Res.*, 91, 7455-7474, 1986.

Scholz, C. H., The frequency-magnitude relation of microfracturing in rock and its relation to earthquakes, *Bull. Seismol. Soc.Am.*, 58, 399-415, 1968.

Segall, P. and D.D. Pollard, Mechanics of discontinuous faults, *J. Geophys. Res.*, 85, 4337-4350, 1980.

Shamir, G., M.D. Zoback and F.H. Cornet, Fracture-induced stress heterogeneity: Examples from the Cajon Pass scientific drillhole near the San Andreas Fault, California, *Proc. Proceedings of the International Symposium on Rock Joints*, edited by N. Barton, O. Stephansson, 719-724, Loen, Norway, 1990.

Shamir, G. and M.D. Zoback, In situ stress orientation near the San Andreas fault: Preliminary results to 2.1 km depth from the Cajon Pass scientific drillhole, *Geophys. Res. Lett.*, 15, 989-992, 1988.

Shamir, G. and M.D. Zoback, The stress orientation profile in the Cajon Pass, California, scientific drillhole, based on detailed analysis of stress-induced borehole breakouts, *Proc. Rock at Great Depth*, edited by V. Maury, D. Fourmaintraux, 1041, Pau, France, 1989.

Sharp, R. V., Variable rates of late Quarternary strike slip on the San Jacinto fault zone, southern California, *J. Geophys. Res.*, 86, 1754-1762, 1981.

Sieh, K. E., Slip along the San Andreas fault associated with the great 1857 earthquake, *Bull. Seismol. Soc. Am.*, 68, 1421-1448, 1978.

Sieh, K. E., M. Stuiver and D. Brillinger, A more precise chronology of earthquakes produced by the San Andreas Fault in Southern California, *J. Geophys. Res.*, 94, 603-623, 1989.

Sieh, K. E. and R.H. Jahns, Holocene activity of the San Andreas fault at Wallace Creek, California, *Geol. Soc. Am. Bull.*, 95, 883-896, 1984.

Simpson, R. W., S.S. Schultz, L.D. Dietz and R.O. Burford, The response of creeping parts of the San Andreas fault to earthquakes on nearby faults: Two examples, *PAGEOPH*, 126, 665-685, 1988.

Smith, K.D., J.N. Brune and K.F.Priestley, Seismic energy, spectrum and the Savage and Wood inequality for complex earthquakes, in *Observatory Seismology*, edited by J.J. Litehiser, pp. 279-302, UC Press, 1989.

Spottiswoode, S. M. and A. McGarr, Source parameters of tremors in a deep level gold mine, *Bull. Seismol. Soc. Am.*, 65, 93-112, 1975.

Steketee, J. A., On Voltera's dislocation in a semi-infinite elastic medium, *Can. J. Phys.*, 36, 192-205, 1958.

Stesky, R. M. and W.F. Brace, Estimation of frictional stress on the San Andreas fault from laboratory measurements, *Proc. Conference on tectonic problems of the San Andreas fault system*, edited by R.L. Kovatch, A. Nur, 206-214, Stanford, California, 1973.

Stock, J. M. and J.H. Healy, Continuation of a deep borehole stress measurement profile near the San Andreas fault, II: Hydraulic fracturing stress measurements at Black Bute, Mojave Desert, CA, *J. Geophys. Res.*, 93, 15196-15206, 1988.

Thatcher, W., Nonlinear strain buildup and the earthquake cycle on the San Andreas fault, *J. Geophys. Res.*, 88, 5893-5902, 1983.

Thatcher, W., Present-day crustal movements and the mechanics of cyclic deformation on the San Andreas fault, *U.S.G.S. Prof. Pap. The San Andreas Fault*, 1990.

Thatcher, W., J.A. Hileman and T.C. Hanks, Seismic slip distribution along the San Jacinto fault zone, southern California, and its implications, *Geol. Soc. Am. Bull.*, 86, 1140-1146, 1975.

Tse, S. T., R. Dmowska and J.R. Rice, Stressing of locked patches along a creeping fault, *Bull. Seismol. Soc. Am.*, 75, 709-736, 1985.

Tucker, B.E. and J.N. Brune, S-wave spectra and source parameters for shocks of the San Fernando earthquake of February 9, 1971, in *Geological and Geophysical studies, vol. 3, San Fernando Earthquake of February 9, 1971*, National Oceanic and Atmospheric Administration, Washington, D.C., 1973.

Turcotte, D. L., Fractals in geology and geophysics, *PAGEOPH*, 131, 171-196, 1989.

Vardulakis, I., J. Sulem and A. Guenot, Borehole instabilities as bifurcation phenomena, *Int. J. Rock Mech. Min. Sci. & Geomech. Abstr.*, 25, 159-170, 1988.

Vernik, L. and M.D. Zoback, Strength anisotropy in crystalline rock: Implications for assessment of in situ stresses from wellbore breakouts, *Proc. Rock mechanics contributions and challenges: Proceedings of the 31st U.S. symposium*, edited by W.A. Hustrulid, G.A. Johnson, 841-848, Colorado, 1990.

Voltera, V., *Ann. sci. ecol norm. superieure, Ser. 3*, 24, 401, 1907.

Weertman, J. and J. R. Weertman, *Elementary dislocation theory*, MacMillan, New York, 1964.

Weibols, G. A. and N.G.W. Cook, An energy criterion for the strength of rock in polyaxial compression, *Int. J. Rock Mech. Min. Sci.*, 5, 529-549, 1968.

Weldon, R. J., The late Cenozoic geology of Cajon Pass: Implications for tectonics and sedimentation along the San Andreas fault, Ph.D. thesis dissertation, 400 pp. pp., Calif. Ins. of Technol., 1986.

Weldon, R. J. and K.E. Sieh, Holocene rate of slip and tentative recurrence intervals for large earthquakes on the San Andreas fault, Cajon Pass, southern California, *Geol. Soc. Am. Bull.*, 96, 793-812, 1985.

Wesson, R. L., Predicted variation of stress orientation with depth near an active fault: Application to the Cajon Pass scientific drillhole, southern California, *Geophys. Res. Lett.*, 15, 1009-1012, 1988.

Wu, F. T. and H. Kanamori, Source mechanism of the Feb. 4, 1965, Rat Island earthquake, *J. Geophys. Res.*, 78, 6082-6092, 1975.

Wyss, M. and J.B. Brune, The Alaska earthquake of March 28, 1964, A complex multiple event, *Bull. Seismol. Soc. Amer.*, 57, 1017-1023, 1967.

Zemanek, J., E.E. Glen Jr., L.J. Norton and R.W. Caldwell, Formation evaluation by inspection with the borehole televiewer, *Geophysics*, 35, 254-269, 1970.

Zheng, Z., J. Kemeny and N.G.W. Cook, Analysis of borehole breakouts, *J. Geophys. Res.*, 94, 7171-7182, 1989.

Zoback, M. D. and D. Moos, In situ stress, natural fracture and sonic velocity measurements in the Moodus, Connecticut scientific research well, Report submitted to Woodward-Clyde Consultants, 90 pp., 1988.

Zoback, M. D., D. Moos, L. Mastin and R.N. Anderson, Wellbore breakouts and in situ stress, *J. Geophys. Res.*, 90, 5523-5530, 1985.

Zoback, M. D., H. Tsukahara and S. Hickman, Stress measurements at depth in the vicinity of the San Andreas fault: Implications for the magnitude of shear stress at depth, *J. Geophys. Res.*, 85, 6157-6173, 1980.

Zoback, M. D. and J.C. Roller, Magnitude of shear stress on the San Andreas fault: Implications of a stress measurement profile at shallow depth, *Science*, 206, 445-447, 1979.

Zoback, M. D. and J. Healy, Stress measurements in the Cajon Pass scientific drillhole, *subm. to J. Geophys. Res.*, 1990.

Zoback, M. D., L.T. Silver, T. Henyey and W. Thatcher, The Cajon Pass scientific drilling experiment: Overview of phase 1, *Geophys. Res. Lett.*, 15, 933-936, 1988.

Zoback, M. L. and M.D. Zoback, Global patterns of tectonic stress, *Nature*, 341, 291-298, 1989.

Zoback, M. D., M.L. Zoback, V.S. Mount, J. Suppe, J.P. Eaton, J.H. Healy, D. Oppenheimer, P. Reasenberg, L. Jones, C.B. Raleigh, I.G. Wong, O. Scotti and C. Wentworth, New evidence on the state of stress of the San Andreas fault system, *Science*, 238, 1105-1111, Nov. 1987.

Zoback, M. D. and M.L. Zoback, State of stress in the conterminous United States, *J. Geophys. Res.*, 85, 6113-6173, 1980.